Advanced Monte Carlo Methods for Eigenvalue Sensitivity Coefficient Calculations

by

Christopher Michael Perfetti

A dissertation submitted in partial fulfillment
of the requirements for the degree of
Doctor of Philosophy
(Nuclear Engineering and Radiological Sciences)
in The University of Michigan
2012

Doctoral Committee:

Professor William R. Martin, Chair
Professor Thomas J. Downar
Professor James P. Holloway
Assistant Professor Krzysztof J. Fidkowski
Bradley T. Rearden, Oak Ridge National Laboratory

For Samim

Acknowledgements

I wish to thank my advisor Bill Martin for his guidance during my graduate school career at the University of Michigan. His breadth of knowledge, insight, and difficult questions have kept me on my toes and transfixed by my work throughout my graduate studies. I would also like to thank my committee members and all of the professors at the Universities of Michigan and Florida for teaching me everything I know. I would especially like to thank my mentor Brad Rearden and the staff at ORNL for providing me the opportunity to work on this amazing project. I am also in debt to the Department of Energy's Nuclear Engineering University Program Graduate Fellowship for supporting me financially during the course of this work.

Most of all I would like to thank my parents for their constant love and support, for providing me with the foundations to live a great life, and for relentlessly bragging about me to their friends.

Table of Contents

List of Figures

Figure

Figure

Figure

List of Tables

Table

Chapter I

Introduction

Eigenvalue sensitivity coefficients describe the fractional change in the eigenvalue of a fissionable system that is induced by changes to system parameters. The eigenvalue sensitivity coefficient for the parameter Σ_x is defined as [1]

$$S_{k,\Sigma_x} = \frac{\delta k/k}{\delta \Sigma_x/\Sigma_x}.$$

(1.1)

In addition to representing the cross-sections of neutron interactions, Σ_x can represent any nuclear data parameter, such as the average number of neutrons emitted per fission, the energy distribution of fission neutrons at birth, or group-to-group scattering probabilities. Eigenvalue sensitivity coefficients, which will be referred to as sensitivity coefficients for convenience, are commonly used in nuclear criticality safety applications to determine adequate safety margins so that systems remain sufficiently sub-critical [2]. For these applications the differential term $\delta\Sigma_x$ in Equation 1.1 is replaced by the uncertainty for Σ_x, and the induced uncertainty for k is determined as follows [1]

$$\sigma_k^2 = S_k C_{\alpha\alpha} S_k^T ,$$

(1.2)

where S_k is the row vector containing all of the relevant sensitivity coefficients for the system and $C_{\alpha\alpha}$ is the matrix containing the relative variances and covariances for the evaluated nuclear data; the elements in $C_{\alpha\alpha}$ are given by

$$C_{\alpha_x,\alpha_y} = \frac{COV(\alpha_x, \alpha_y)}{\alpha_x \alpha_y}, \tag{1.3}$$

where x and y vary across all regions, isotopes, reactions, and energies of interest.

Perhaps the most extensive use of sensitivity coefficients occurs in the TSUNAMI-3D (**T**ools for **S**ensitivity and **U**ncertainty **A**nalysis **M**ethodology **I**mplementation in **Three D**imensions) code within the SCALE code package. TSUNAMI-3D uses 3D Monte Carlo simulations to calculate sensitivity coefficients and the overall uncertainty in the eigenvalue for systems, and can also use these sensitivity coefficients to determine the degree of similarity between systems and to quantify biases and uncertainties in nuclear system responses [1] [2]. TSUNAMI currently calculates sensitivity coefficients by performing forward and adjoint multigroup Monte Carlo simulations and tallying the forward and adjoint neutron fluxes in a system as a function of space, energy, and angle. Several factors have created a push towards generating sensitivity coefficients using continuous-energy methods, including the need for higher fidelity in sensitivity coefficients, the need to calculate sensitivity coefficients for advanced applications (such as modeling fast reactors, high-temperature gas-cooled reactors, and other next-generation designs), and the need to develop adjoint-weighted tallies for calculating reactor kinetics parameters and generalized sensitivity coefficients. The current TSUNAMI approach of performing adjoint Monte Carlo simulations is not appropriate for continuous-energy applications because of the difficulty in transposing a continuous-energy neutron scattering operator, and new methods for calculating eigenvalue sensitivity coefficients must be developed to extend sensitivity coefficient calculations to the continuous-energy regime. This dissertation examines several new and existing methods for performing sensitivity coefficient calculations that have the potential for continuous-energy applications. The existing methods examined in this

study include the Differential Operator method, the Iterated Fission Probability method, and the Contributon method.

Originally developed by Olhoeft, the Differential Operator method determines the importance of a neutron interaction in a Monte Carlo simulation by tallying the number of fission neutrons produced by the neutron after the event occurs [3]. The Differential Operator method has been previously implemented in the SCALE and MCNP codes, but has been shown to produce inaccurate sensitivity coefficient estimates for complex systems and has fallen out of favor in recent years [1] [4]. The Iterated Fission Probability method, which has been implemented in the SCALE, MCNP, and McCARD codes, can achieve more accurate estimates for the importance of events in Monte Carlo calculations than the Differential Operator method [1] [5] [6]. Originally developed by Hurwitz, the Iterated Fission Probability method relies on the concept of importance which states that the importance of an event can be determined by tallying the population of neutrons present in a system several generations after the original event occurs [7]. Although the Iterated Fission Probability method produces accurate sensitivity coefficient estimates, it can have large memory requirements for complex problems. Developed by Williams for shielding applications, the Contributon method determines the importance of an event by simulating secondary particles at the site of the event and tracking the number of fission neutrons created by each secondary particle [8]. The Contributon method is currently implemented in the SCALE code package and causes substantial increases in problem runtimes because of the large number of secondary particle simulations required by the method [1].

This dissertation examines two new approaches for calculating eigenvalue sensitivity coefficients that have potential for continuous-energy applications: the Contributon-IFP Hybrid method and the CLUTCH (**C**ontributon-**L**inked eigenvalue sensitivity/**U**ncertainty estimation via **T**racklength importance **Ch**aracterization) method. Conceived by Brown, the Contributon-IFP Hybrid method combines the Iterated Fission Probability methodology for calculating the importance of an event with the Contributon notion of simulating secondary particles to reduce the method's memory requirements [9]. The CLUTCH method, which was created and developed during the course of this dissertation research, uses the Contributon methodology for calculating the importance of

events but eliminates the need to simulate secondary particles by instead examining the behavior of a neutron within each neutron history.

Each of these sensitivity methods is implemented, tested, and evaluated in the Shift Monte Carlo code within the Denovo framework of the SCALE code package. Developed recently for the CASL project, Shift is a 3D Monte Carlo code designed for applicability in large scale, massively-parallel reactor core calculations. The various sensitivity coefficient methods discussed here are used to calculate sensitivity coefficients for a series of test problems, and the performance and scalability of each method is evaluated. Each method is compared in terms of accuracy, speed, efficiency, and memory requirements. The newly developed CLUTCH method is shown to perform well in each of these categories, and shows potential to accurately and efficiently calculate eigenvalue sensitivity coefficients for continuous-energy applications.

Chapter II

Methodologies for Calculating Eigenvalue Sensitivity Coefficients

Sensitivity coefficients are commonly determined using first-order perturbation theory, which uses properties of adjoint functions to determine the change in an eigenvalue in response to small perturbations in system parameters. The steady-state Boltzmann neutron transport equation states that the neutron balance for a steady-state system is given by

$$B\Phi = \lambda F\Phi \,, \tag{2.1}$$

where Φ is the neutron flux, λ is equal to $1/k$, the neutron transport-collision term B is given by

$$B\Phi = \Omega \bullet \nabla\Phi(r,E,\Omega) + \Sigma_t(r,E)\Phi(r,E,\Omega) - \int_{4\pi} d\hat{\Omega}' \int_0^{\infty} dE' \Sigma_s\left(r,E' \rightarrow E, \hat{\Omega}' \rightarrow \hat{\Omega}\right)\Phi(r,E',\hat{\Omega}') \,, \tag{2.2}$$

and the neutron production term F is given by

$$F\Phi = \frac{\chi(r,E)}{4\pi}\int_{4\pi} d\hat{\Omega}'\int_{0}^{\infty} dE'\bar{\upsilon}\Sigma_f\left(r,E',\hat{\Omega}'\right)\Phi\left(r,E',\hat{\Omega}'\right) + S\left(r,E,\hat{\Omega}\right).$$

(2.3)

Note that for eigenvalue problems the neutron source $S(r,E,\hat{\Omega})$ typically equals zero. The adjoint steady-state transport equation is given by

$$B^*\Phi^* = \lambda F^*\Phi^*,$$

(2.4)

where Φ^* is the adjoint neutron flux, the adjoint neutron transport-collision term B^* is given by

$$B^*\Phi^* = -\hat{\Omega}\bullet\nabla\Phi^*(r,E,\Omega) + \Sigma_t(r,E)\Phi^*(r,E,\Omega) - \int_{4\pi} d\hat{\Omega}'\int_{0}^{\infty} dE'\Sigma_s\left(r,E\to E',\hat{\Omega}\to\hat{\Omega}'\right)\Phi^*(r,E',\hat{\Omega}),$$

(2.5)

and the adjoint neutron production term F^* is given by

$$F^*\Phi^* = \bar{\upsilon}\Sigma_f\left(r,E,\hat{\Omega}\right)\int_{4\pi} d\hat{\Omega}'\int_{0}^{\infty} dE'\frac{\chi(r,E')}{4\pi}\Phi^*\left(r,E',\hat{\Omega}'\right) + S^*\left(r,E,\hat{\Omega}\right).$$

(2.6)

Conceptually, the adjoint flux represents the importance of neutrons in a given phase space to the calculation of the eigenvalue for a system. For eigenvalue problems the source term for neutron importance in Equation 2.6, $S^*(r,E,\hat{\Omega})$, equals zero. In first-order perturbation theory a differential perturbation is introduced into Equation 2.1 such that

$$F' = F + \delta F,$$
$$B' = B + \delta B,$$
$$\lambda' = \lambda + \delta\lambda,$$

$$\Phi' = \Phi + \delta\Phi .$$

After being multiplied by Φ^* and integrated over space, energy, and angle, the perturbed Equation 2.1 becomes

$$\begin{aligned} <\Phi^* B\Phi> + <\Phi^* \delta B\Phi> + <\Phi^* B\delta\Phi> + <\Phi^* \delta B\delta\Phi> = <\lambda\Phi^* F\Phi> + \\ <\lambda\Phi^* \delta F\Phi> + <\delta\lambda\Phi^* F\Phi> + <\delta\lambda\Phi^* \delta F\Phi> + <\lambda\Phi^* F\delta\Phi> + \\ <\lambda\Phi^* \delta F\delta\Phi> + <\delta\lambda\Phi^* F\delta\Phi> + <\delta\lambda\Phi^* \delta F\delta\Phi> . \end{aligned}$$

(2.7)

As its name suggests, first-order perturbation theory assumes that all higher-order terms are negligible. Discarding these terms gives

$$\begin{aligned} <\Phi^* B\Phi> + <\Phi^* \delta B\Phi> + <\Phi^* B\delta\Phi> = <\lambda\Phi^* F\Phi> + <\lambda\Phi^* \delta F\Phi> + \\ <\delta\lambda\Phi^* F\Phi> + <\lambda\Phi^* F\delta\Phi> . \end{aligned}$$

(2.8)

Additional terms can be cancelled through the property of adjointness (i.e., $<\Phi^*(B-\lambda F)\Phi'> = <\Phi'(B^*-\lambda F^*)\Phi^*> = 0$), and Equation 2.8 reduces to

$$\delta\lambda = \frac{<\Phi^*(\delta B - \lambda\delta F)\Phi>}{<\Phi^* F\Phi>} .$$

(2.9)

Because $\lambda = 1/k$, it can be shown that $\delta\lambda = -\delta k / k^2$. Combining Equations 1.1 and 2.9 gives

$$S_{k,\Sigma_x} = \Sigma_x \frac{<\Phi^*\left(\lambda\frac{\delta F}{\delta\Sigma_x} - \frac{\delta B}{\delta\Sigma_x}\right)\Phi>}{\lambda <\Phi^* F\Phi>} .$$

(2.10)

2.1 Terms Required for Calculating Eigenvalue Sensitivity Coefficients

Now that the first-order perturbation method for determining sensitivity coefficients has been derived, methods for calculating individual sensitivity coefficients are explained.

2.1.1 Calculating Eigenvalue Sensitivity Coefficients

Determining sensitivity coefficients using Equation 2.10 requires calculating the equation's denominator term as well as three functions that describe different forms of the inner product for $\Phi\Phi^*$ in the numerator. The first inner product in Equation 2.10 describes the forward and adjoint fluxes in the $\Sigma_t(r,E)\Phi(r,E,\Omega)$ term of Equation 2.2, also known as the collisional term, which, for a zone z, is given by [10]

$$C_x(z,E) = \int_{V_z}\int_{4\pi} \Sigma_x(r,E)\Phi(r,E,\hat{\Omega})\Phi^*(r,E,\hat{\Omega})d\hat{\Omega}dV \ . \tag{2.11}$$

As shown in Equation 2.11, the forward and adjoint flux in the collisional term share the same space, energy, and direction coordinates. The second inner product in Equation 2.10 describes the fluxes in the fission source term of Equation 2.3, which, for zone z, is given by [10]

$$C_f(z,E\rightarrow E') = \int_{V_z}\int_{4\pi} \bar{\upsilon}\Sigma_f(r,E)\Phi(r,E,\hat{\Omega})d\hat{\Omega}\int_{4\pi}\frac{\chi(r,E')}{4\pi}\Phi^*(r,E',\hat{\Omega}')d\hat{\Omega}'dV \ . \tag{2.12}$$

As shown in Equation 2.12, the forward and adjoint fluxes in the fission source term are correlated only in space. The energy and direction coordinates *E'* and $\hat{\Omega}'$ represent the random energy and direction of particles emerging from fission events. The third inner product in Equation 2.10 describes the fluxes in the scattering source term of Equation 2.2, which, for zone z, is given by [10]

$$C_s(z, E \to E') = \int_{V_z} \int_{4\pi} \int_{4\pi} \Phi(r, E, \hat{\Omega}) \Sigma_s(r, E \to E', \hat{\Omega} \to \hat{\Omega}') \Phi^*(r, E', \hat{\Omega}') d\hat{\Omega}' d\hat{\Omega} dV \, .$$

(2.13)

As shown in Equation 2.13 the forward and adjoint fluxes in the scattering source term share the same spatial coordinates and the energy and direction terms are correlated by scattering kinematics.

The denominator term in Equation 2.10 represents the adjoint-weighted fission source term integrated over all regions and nuclides, and is defined as [10]

$$D = \lambda \int_V \int_0^\infty \int_{4\pi} \bar{\upsilon} \Sigma_f(r, E) \phi(r, E, \Omega) d\Omega dE \int_0^\infty \int_{4\pi} \frac{\chi(r, E')}{4\pi} \, \phi^*(r, E', \Omega') d\Omega' dE' \, dV$$

(2.14)

After calculating these four terms the sensitivity coefficients for nuclides in region z can be determined as detailed in Equations 2.15 through 2.19. The sensitivity coefficients described by Equations 2.15 through 2.19 have been integrated over energy to form multigroup sensitivity coefficients, which is common practice even when using continuous-energy methods because the covariance matrices which contain uncertainty estimates for evaluated nuclear data are reported using a multigroup energy structure. In practice there exists sensitivity coefficients for more reactions and phenomena than are listed in Equations 2.15 though 2.19, but the research presented here focuses only on the following five primary sensitivity coefficients. Note that to obtain the sensitivities for individual nuclides within a zone one should multiply by Σ_x for the nuclide of interest instead of Σ_x for the zone. Note also that $\bar{\upsilon}$ is a function of energy.

Sensitivity Coefficient for the Capture Cross Section for Energy Group g in Zone z:

$$S_{cap}(z, g) = -\int_g \frac{C_{x=cap}(z, E)}{D} dE.$$

(2.15)

Sensitivity Coefficient for the Fission Cross Section for Energy group g in Zone z:

$$S_f(z,g) = \int_g \left[\lambda \int_0^\infty \frac{C_f(z, E \to E')}{D} \, dE' - \frac{C_{x=fis}(z,E)}{D} \right] dE.$$

(2.16)

Sensitivity Coefficient for the Scattering Cross Section for Energy Group g in Zone z:

$$S_s(z,g) = \int_g \left[\int_0^\infty \frac{C_s(z, E \to E')}{D} \, dE' - \frac{C_{x=sca}(z,E)}{D} \right] dE.$$

(2.17)

Sensitivity Coefficient for $\bar{\upsilon}$ for Energy Group g in Zone z:

$$S_{\bar{\upsilon}}(z,g) = \lambda \int_g \left[\int_0^\infty \frac{C_f(z, E \to E')}{D} \, dE' \right] dE \, .$$

(2.18)

Sensitivity Coefficient for χ for Energy Group g in Zone z:

$$S_\chi(z,g) = \lambda \int_g \left[\int_0^\infty \frac{C_f(z, E' \to E)}{D} \, dE' \right] dE \, .$$

(2.19)

2.1.2 Constrained Chi Sensitivities

Because the probability distribution for the prompt fission neutron, or chi, spectrum must always equal one when integrated over all energies, an increase to the

probability that a neutron is born in an energy group must be accompanied by a decrease in the probability that the neutron is born in other energy groups. Equation 2.19 does not account for this renormalization, and a set of equations have been developed by Nagaya to account for the interdependence of the chi sensitivity coefficients and to obtain effective, or "constrained," chi sensitivity coefficients [11]. A new approach for calculating constrained chi sensitivity has also been developed during the course of this research, and the two methods will be compared in Chapter 3.8.

Given the prompt fission neutron emission probability for group g, χ_g, Nagaya's approach assumes that the perturbation $\Delta\chi_g$ to χ_g results in an equal fractional change in the prompt fission neutron emission spectrum probability in every other group such that, for each energy group *i*,

$$\chi'_{i=g} = \frac{\chi_i + \Delta\chi_g}{1+\Delta\chi_g} \qquad \text{and} \qquad \chi'_{i\neq g} = \chi_i \frac{1}{1+\Delta\chi_g}. \tag{2.20}$$

This approach assumes that a perturbation in the emission probability in one energy group affects the emission probabilities in all other energy groups, and does not allow for the possibility that a perturbation in the emission probability in one energy group would only affect the emission probabilities in neighboring energy groups. The change in the emission probabilities due to the perturbation is

$$\Delta\chi_{i=g} = (1-\chi_i)\frac{\Delta\chi_g}{1+\Delta\chi_g} \qquad \text{and} \qquad \Delta\chi_{i\neq g} = -\chi_i \frac{\Delta\chi_g}{1+\Delta\chi_g}, \tag{2.21}$$

which can be expanded using the Taylor series to give

$$\Delta\chi_{i=g} = (1-\chi_i)\left(\Delta\chi_g - \Delta\chi_g^2 + \Delta\chi_g^3 \ldots\right) \quad \text{and}$$
$$\Delta\chi_{i\neq g} = -\chi_i \left(\Delta\chi_g - \Delta\chi_g^2 + \Delta\chi_g^3 \ldots\right). \tag{2.22}$$

Assuming infinitesimal perturbations and ignoring all higher-order terms causes Equation 2.22 to become

$$\frac{\delta\chi_{i=g}}{\delta\chi_g} = (1-\chi_i) \qquad \text{and} \qquad \frac{\delta\chi_{i\neq g}}{\delta\chi_g} = -\chi_i.$$

(2.23)

The multivariate derivative of the eigenvalue with respect to some perturbation in χ_g is given by

$$\frac{\delta k}{\delta\chi_g} = \frac{\delta k}{\delta\chi_{i=g}}\frac{\delta\chi_{i=g}}{\delta\chi_g} + \sum_{i\neq g}\frac{\delta k}{\delta\chi_{i\neq g}}\frac{\delta\chi_{i\neq g}}{\delta\chi_g}.$$

(2.24)

Multiplying both sides of Equation 2.24 by χ_g/k and incorporating the differential terms in Equation 2.23 gives the constrained chi sensitivity as

$$S_{\chi_g}^{con} = \frac{\delta k/_k}{\delta\chi_{i=g}/_{\chi_g}}(1-\chi_g) - \chi_g\sum_{i\neq g}\frac{\delta k/_k}{\delta\chi_i/_{\chi_i}}.$$

(2.25)

Combining the $i = g$ term with the summation term and applying the sensitivity coefficient definition from Equation 1.1 gives

$$S_{\chi_g}^{con} = S_{\chi_{i=g}} - \chi_g\sum_i S_{\chi_i}.$$

(2.26)

A new approach for calculating constrained chi sensitivity coefficients has been developed by applying an alternate chi spectrum renormalization scheme: instead of renormalizing all values of chi after a perturbation to χ_g, only the chi values in groups $i \neq g$ are renormalized, such that

$$\chi'_{i=g} = \chi_i + \Delta\chi_g \qquad \text{and} \qquad \chi'_{i\neq g} = \chi_i \frac{1-\chi_g-\Delta\chi_g}{1-\chi_g}.$$

(2.27)

This approach again assumes that a perturbation in the emission probability in one energy group does not just affect the neighboring energy groups, and instead affects all energy groups. The change in the emission probabilities due to the perturbation and renormalization are

$$\Delta\chi_{i=g} = \Delta\chi_g \qquad \text{and} \qquad \Delta\chi_{i\neq g} = -\chi_i \frac{\Delta\chi_g}{1-\chi_g},$$

(2.28)

and an infinitesimal perturbation implies that

$$\frac{\delta\chi_{i=g}}{\delta\chi_g} = 1 \qquad \text{and} \qquad \frac{\delta\chi_{i\neq g}}{\delta\chi_g} = -\chi_i \frac{1}{1-\chi_g}.$$

(2.29)

Multiplying both sides of Equation 2.24 by χ_g/k and incorporating the differential terms in Equation 2.29 gives the new constrained chi sensitivity as

$$\hat{S}^{con}_{\chi_g} = \frac{\delta k/k}{\delta\chi_{i=g}/\chi_g} - \frac{\chi_g}{1-\chi_g}\sum_{i\neq g}\frac{\delta k/k}{\delta\chi_i/\chi_i}.$$

(2.30)

Adding and subtracting the term $\frac{\chi_g}{1-\chi_g}S_{\chi_{i=g}}$ and applying the sensitivity coefficient definition from Equation 1.1 gives

$$\hat{S}^{con}_{\chi_g} = \frac{S_{\chi_{i=g}}}{1-\chi_g} - \frac{\chi_g}{1-\chi_g}\sum_i S_{\chi_i},$$

(2.31)

which differs from Equation 2.26 by a factor of $\frac{1}{1-\chi_g}$. This suggests that the two methods for calculating constrained chi sensitivities approach equivalence as the number of groups in a simulation approaches infinity and the value of chi for each group becomes small.

Although the sum of all of the unconstrained chi sensitivity coefficients in a problem equals one, Nagaya's equation for constrained chi sensitivity has the property that the sum of all constrained chi sensitivities over all energy groups and nuclides in a system equals zero, which implies that the impact of perturbing one value of χ_g is counteracted by the opposite perturbation induced when the values of chi for other energy groups are perturbed in response. The new approach for calculating chi sensitivity coefficients does not assume this is true, and allows for a perturbation in one very important group to overpower the effect of renormalizing chi in other groups. The new approach for calculating chi sensitivities also contains fewer mathematical assumptions than Nagaya's approach because it does not discard higher-order differential terms in Equation 2.22, and the accuracy of the two approaches will be discussed in Chapter 3.8.

2.1.3 Estimating the Variance of Sensitivity Coefficient Tallies

Because Monte Carlo processes are random processes, Monte Carlo simulations typically calculate the variance of tally estimates to quantify the level of tally precision, or uncertainty, achieved for a simulation. Consider an estimate for the expected value of some parameter that is determined after simulating N neutron histories, such that

$$E(x) = \frac{1}{N}\sum_{i}^{N} x_i \, .$$

(2.32)

The variance of this estimate is given by [12]

$$Var(x) \approx \frac{1}{N}\left[\frac{1}{N}\sum_{i}^{N} x_i^2 - \left(\frac{1}{N}\sum_{i}^{N} x_i\right)^2\right].$$

(2.33)

Calculating the variance of sensitivity coefficients, as described in Equations 2.15 through 2.19, requires combining the variance estimates for the sensitivity tallies in Equations 2.11 through 2.14 to determine the overall variance for each sensitivity coefficient; however, one must account for the shared variance, or covariance, of the tallies when calculating the true variance of sensitivity coefficients. Consider two sets of regions in a Monte Carlo simulation: one set of adjacent regions and one set of regions that are on opposite sides of a reactor core. The tallies for the first set of regions will likely be strongly correlated because particles streaming through one region are likely to contribute tallies to both regions, while the tallies for the regions that are on opposite sides of a reactor model are likely to be uncorrelated. For sensitivity coefficient tallies, the sensitivity terms in Equations 2.11, 2.12, and 2.13 can be strongly correlated with adjoint-weighted fission source term in Equation 2.14 for regions where particles contribute significantly to the adjoint-weighted fission source for the problem. The covariance for two tallies, x and y, during a Monte Carlo simulation is given by

$$cov(xy) \approx \frac{1}{N}\left[\frac{1}{N}\sum_{i}^{N} x_i y_i - \left(\frac{1}{N}\sum_{i}^{N} x_i\right)\left(\frac{1}{N}\sum_{i}^{N} y_i\right)\right].$$

(2.34)

The overall variance of a parameter Z that is the sum of the parameters X and Y, multiplied by the constants x and y, respectively, is given by [13]

$$\sigma_Z^2 = x^2\sigma_X^2 + y^2\sigma_Y^2 + 2xy\, cov(XY)\,,$$

(2.35)

and the overall variance of a parameter Z that is the quotient of the parameters X and Y is given by [13]

$$\left(\frac{\sigma_Z}{Z}\right)^2 = \left(\frac{\sigma_X}{X}\right)^2 + \left(\frac{\sigma_Y}{Y}\right)^2 - 2\frac{cov(XY)}{XY}.$$

(2.36)

Covariance estimates for eigenvalue sensitivity coefficients has been incorporated in the Shift code, and were used when calculating sensitivity coefficient variance estimates presented in Chapter 3.

2.2 Conventional TSUNAMI Methodology

The first method presented for calculating sensitivity coefficients is currently used by the TSUNAMI-3D code in the SCALE Code Package [1]. TSUNAMI uses the KENO Monte Carlo code to simulate both a forward and an adjoint transport calculation for a problem while tallying the forward and adjoint angular fluxes, and then applies these fluxes to Equations 2.11 through 2.19 to calculate the various sensitivity coefficients. Although performing forward Monte Carlo calculations is a commonly-understood process, solving the adjoint Boltzmann neutron transport equations using Monte Carlo methods is a much less common process, and will be explained briefly.

2.2.1 Adjoint Monte Carlo Simulations

Upon examining Equations 2.2, 2.3, 2.5, and 2.6, one notices that the forward and adjoint transport equations are very similar, and differ slightly in the leakage, scattering source, and fission source terms. By modifying several of the physics parameters in the forward transport equation, one can "fool" a forward, multigroup Monte Carlo code into simulating adjoint neutron transport.

The leakage term does not need special treatment because Monte Carlo methods directly model the leakage of a system by tracking individual neutron histories. Looking at the fission terms in Equations 2.3 and 2.6, one notices that the neutron production cross section, $\bar{\upsilon}\Sigma_f$, and the fission spectrum term, exchange places when the forward transport equation is made adjoint. Thus the adjoint fission spectrum for a nuclide is redefined in terms of forward cross sections as

$$\chi(E)^{adj} = \frac{\bar{\upsilon}\Sigma_f(E)}{\sum_i^{All\ E} \bar{\upsilon}\Sigma_f(E_i)}, \tag{2.37}$$

and the adjoint neutron production cross section is redefined in terms of forward cross sections as

$$\bar{\upsilon}\Sigma_f(E)^{adj} = \chi(E)\sum_{i}^{All\ E}\bar{\upsilon}\Sigma_f(E_i)\ .$$

(2.38)

Substituting these new definitions for $\bar{\upsilon}\Sigma_f(E)^{adj}$ and $\chi(E)^{adj}$ into Equation 2.3 causes it to reduce to Equation 2.6.

Figure 2.1 shows a sample plot of the forward $\bar{\upsilon}\Sigma_f(E)$ and $\chi(E)$ for U-235 [14]. As seen in the figure, the U-235 neutron production cross section is somewhat constant over different energies and the fission spectrum is non-zero only above about 1 keV; similar behavior is observed for other fissile isotopes. The discontinuous nature of the fission spectrum causes the adjoint neutron production cross sections to be zero for energies below 1 keV, and thus neutrons in an adjoint Monte Carlo simulation can only cause fission events at fast energies. Neutrons in fissile material for forward Monte Carlo simulations encounter non-zero fission cross section at all energies, whereas adjoint neutrons must avoid leakage and absorption long enough to scatter up to fast energies to cause fission events. Thus, the nature of adjoint cross sections induces a greater variance in the eigenvalue estimate for adjoint Monte Carlo simulations, and adjoint calculations must simulate more particle histories to obtain eigenvalue uncertainties of a similar magnitude to those from forward calculations. The default for TSUNAMI-3D is to simulate three times the number of forward neutron histories per generation over twice as many active generations for adjoint simulations, and some cases require as much as 50 times the number of forward neutron histories per generation.

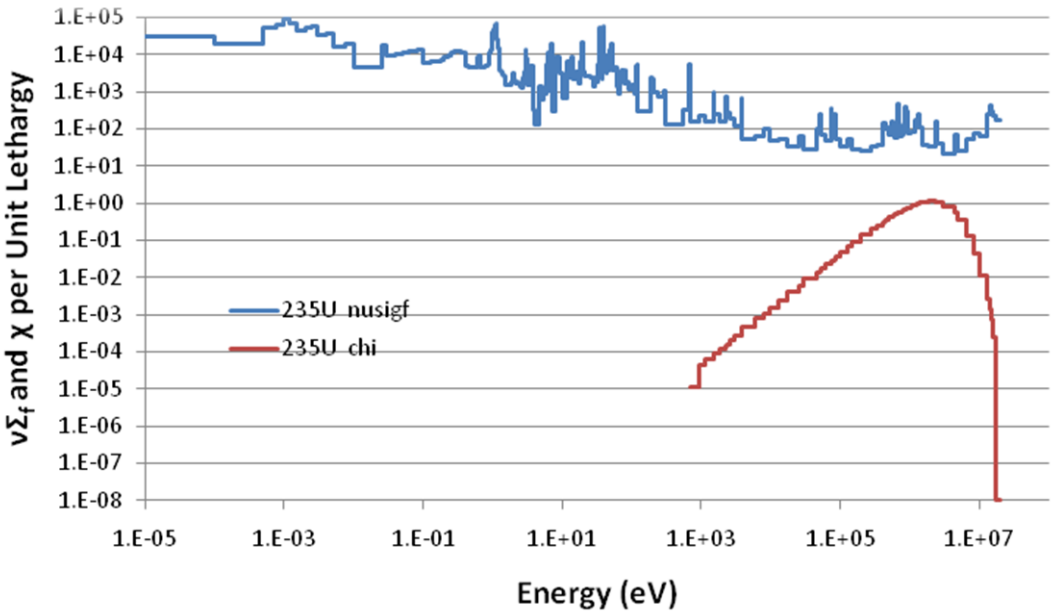

Figure 2.1: Neutron production cross section (nusigf) and prompt fission emission spectrum (chi) for U-235 [14].

Equations 2.2 and 2.5 suggest that the group-to-group scattering matrix must be transposed in order to model the scattering term for adjoint transport calculations. The adjoint scattering probability is modified such that

$$p(E \to E')^{adj} = \frac{\Sigma_s(E' \to E)}{\sum_i^{All\ E'} \Sigma_s(E_i{}' \to E)}. \tag{2.39}$$

While transposing the scattering matrix is not difficult for multigroup Monte Carlo calculations, inverting the scattering matrix for continuous-energy simulations is challenging due to the use of cross-section relations. Many group-to-group scattering probabilities are well-behaved across large energy ranges and are described in Monte Carlo data using equations of scattering relations to reduce cross-section memory usage. These scattering relations must be removed and converted into discrete cross-section values to transpose the continuous-energy scattering matrix. Discretized cross-section files that remove the memory-saving scattering relations can occupy on the order of

gigabytes of memory, which makes adjoint Monte Carlo calculations for systems with a large number of nuclides unfeasible [15].

Modifying the scattering source term to simulate adjoint transport also forces one to change how implicit capture is treated. Implicit capture, a variance-reduction technique that is used in virtually all Monte Carlo neutron transport codes, forces neutrons to scatter at every collision, and instead of allowing for particles to be killed by absorption during a collision, implicit capture slowly reduces the weight of particles emerging from collisions until they leak or are killed via Russian Roulette. Because the probability of a neutron scattering at a collision is equal to Σ_s/Σ_t, the weight of a neutron emerging from an implicit capture collision is modified such that

$$weight^{new} = weight^{old} \cdot \frac{\Sigma_s}{\Sigma_t}. \tag{2.40}$$

Because the adjoint scattering source for neutrons emerging from collisions is different from the forward source, the scattering cross section for implicit capture must be treated differently for adjoint Monte Carlo simulations. For forward simulations, the scattering cross section is given by

$$\Sigma_s(E) = \sum_{i}^{All\ E'} \Sigma_s(E \rightarrow E_i') . \tag{2.41}$$

For adjoint Monte Carlo calculations, the implicit capture scattering cross-section is given by

$$\Sigma_s(E)^{adj} = \sum_{i}^{All\ E'} \Sigma_s(E_i' \rightarrow E) . \tag{2.42}$$

Thus it is possible $\Sigma_s(E)^{adj}$ to be greater than $\Sigma_t(E)$ and for neutrons emerging from a collision to have a greater weight than when entering the collision.

2.2.2 Pathlength Flux Tallies

During the forward and adjoint Monte Carlo simulations, TSUNAMI uses a flux mesh to capture the spatial, energy, and directional dependence of the forward and adjoint fluxes that are used to in Equations 2.11 through 2.14 to calculate sensitivity coefficients. The flux that is tallied for a neutron passing on track T through the mesh interval in phase space *(r, E, Ω)* is recorded using the pathlength flux tally estimator that is given by

$$\Phi(r,E,\Omega) = \frac{w_T l_T}{N\Delta V \Delta E \Delta\Omega}, \tag{2.43}$$

where

w_T = The weight of the particle during the track T,

l_T = The length of track T,

N = The total number, or weight, of active histories for the simulation,

ΔV = The volume of the mesh at r,

ΔE = The width of the energy interval at E,

$\Delta\Omega$ = The width of the angular interval at Ω.

The width of the angular interval is determined using a user-specified order of discrete ordinate angles; is should be noted that although TSUNAMI bins and tallies the angular fluxes using a discrete ordinates treatment, neutrons in TSUNAMI are still allowed to exist in any solid angle, as described by the conventional, continuous-angle Monte Carlo treatment. TSUNAMI can also tally flux moments in lieu of discrete ordinate fluxes, as discussed in detail in Reference 16.

2.2.3 Conventional TSUNAMI Methodology Evaluation

The greatest advantage for the conventional TSUNAMI methodology is that it directly tallies the forward and adjoint fluxes when calculating sensitivity coefficients. In addition to allowing the user to investigate how the two fluxes vary across a system, this allows for the efficient calculation of sensitivity coefficients for rare reactions. The other sensitivity coefficient methodologies only tally contributions towards sensitivity coefficient tallies for a reaction when particles undergo that reaction, making it difficult for these methodologies to, for example, tally the sensitivity coefficient for fast-to-thermal scattering cross sections in a fast system. In this instance, although the number of particles that undergo the fast-to-thermal scattering reaction is very low, the importance of the newly-created thermal neutrons may be very high and may result in a significant contribution to the sensitivity coefficient for that reaction. Because TSUNAMI separately tallies the forward and adjoint fluxes, sensitivity coefficients for these rare but important reactions can be generated with greater efficiency.

The fact that TSUNAMI performs separate forward and adjoint Monte Carlo calculations can be viewed as a disadvantage because the user must wait for two Monte Carlo simulations to finish. As mentioned previously, the adjoint simulation requires more neutron histories than the forward simulation, and adjoint simulations often require much more simulation time than their forward counterparts. Furthermore, because few people have investigated adjoint Monte Carlo calculations in great depth, concepts such as Shannon Entropy and fission source convergence are not well understood for adjoint simulations.

The greatest disadvantage to the conventional TSUNAMI methodology is the large memory requirements of the forward and adjoint flux meshes. For example, a quarter-core model of a PWR using a 1 cm^3 mesh, 238 energy groups, and a S_4 quadrature set requires approximately:

$$\frac{1}{4} \times 200\ x\ intervals\ \times 200\ y\ intervals\ \times 400\ z\ intervals\ \times 238\ energy\ groups$$
$$\times\ 24\ directions \times 8\ bytes\ per\ double$$
$$= 182.8\ gigabytes\ of\ memory\ per\ flux\ mesh.$$

(2.44)

Furthermore, a 1 cm^3 mesh and S_4 quadrature set are often not sufficiently resolved to obtain accurate sensitivity coefficients [17]. TSUNAMI results can be extremely sensitive to the flux mesh discretization because the forward and adjoint fluxes are averaged across each phase space bin before they are multiplied to calculate sensitivity coefficients, and thus systems with a strong spatial, energy, or angular dependence for the forward and adjoint fluxes must use a very finely resolved flux mesh. Memory requirements prevent the use of tens of thousands of energy groups for tallying the forward and adjoint fluxes during continuous-energy calculations, and the forward and adjoint fluxes must instead be grouped into multigroup bins when tallied; this introduces inaccuracy when calculating sensitivity coefficients for multigroup bins containing cross section resonances because the neutron fluxes and importances are considered constant throughout each energy bin. The resolution of the flux discretization can be lowered when performing TSUNAMI calculations to reduce memory usage, but this often results in a loss of sensitivity coefficient accuracy. Thus, to avoid the pitfalls of flux discretization and the encumberment of a multi-gigabyte memory requirement, it is desirable to develop methods for sensitivity coefficient calculation that do not require a flux mesh.

2.3 Differential Operator Methodology

Although all of the other methods that were investigated in this study make use of adjoint-weighted tallies to calculate sensitivity coefficients, the Differential Operator method calculates sensitivity coefficients by directly taking the derivative of the Monte Carlo process for generating eigenvalue tallies with respect to a perturbation in Σ_x [4]. This results in a fast and efficient method for calculating eigenvalue sensitivity

coefficients, but the lack of adjoint-weighted tallies often causes inaccuracies in the calculated sensitivity coefficients.

2.3.1 Differential Operator Description and Derivation

The Differential Operator method states that the eigenvalue can be determined by summing $k_\tau p_\tau$ over all possible neutron paths τ, where k_τ is the eigenvalue generated by a neutron on path τ and p_τ is the probability of a neutron living its lifetime following path τ; thus,

$$k = \sum_{\tau} (k_\tau p_\tau) \, . \tag{2.45}$$

The Differential Operator method manipulates Equation 2.45 such that

$$\frac{\delta k}{\delta \Sigma_x / \Sigma_x} = \sum_{\tau} (k_\tau p_\tau) \Lambda_\tau \, , \tag{2.46}$$

where

$$\Lambda_\tau \equiv \frac{\Sigma_x}{p_\tau} \frac{\delta p_\tau}{\delta \Sigma_x} + \frac{\Sigma_x}{k_\tau} \frac{\delta k_\tau}{\delta \Sigma_x} \equiv \alpha_\tau + \beta_\tau \, . \tag{2.47}$$

For a Monte Carlo simulation of N particle histories, each containing s particle paths between two collisions, Equations 2.46 and 2.47 become

$$\frac{\delta k}{\delta \Sigma_x / \Sigma_x} = \frac{1}{N} \sum_{i=1}^{N} \sum_{s} \Lambda_s k_s \, , \tag{2.48}$$

where

$$\Lambda_s \equiv \frac{\Sigma_x}{p_s}\frac{\delta p_s}{\delta \Sigma_x} + \frac{\Sigma_x}{k_s}\frac{\delta k_s}{\delta \Sigma_x} \equiv \alpha_s + \beta_s \, .$$

(2.49)

The p_s term is not carried over from Equation 2.46 to Equation 2.49 because it is already taken into account by the Monte Carlo nature of the problem: the probability that a Monte Carlo code tracks a neutron following path *s* is equal to p_s.

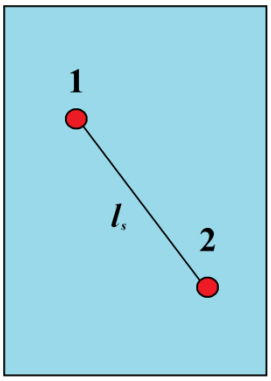

Figure 2.2: The particle track *s* in a material.

Figure 2.2 shows a sample path *s* of length l_s between points 1 and 2 in some material. The probability of track *s* occurring is given by

$$p_s = \frac{\Sigma_s(E_1 \to E_2, \Omega_1 \to \Omega_2)}{\Sigma_t(E_1)} \Sigma_t(E_2) e^{-\Sigma_t(E_2) l_s}.$$

(2.50)

Equation 2.50 incorporates both the probability that at point 1 the particle scatters from energy E_1 to E_2 and direction Ω_1 to Ω_2, and the probability that the particle travels length l_s before undergoing a collision at point 2. It can be shown that

$$\alpha_s = \frac{\Sigma_x}{p_s}\frac{\delta p_s}{\delta \Sigma_x} = \frac{\Sigma_x(E)}{\Sigma_s(E_1)}\frac{\delta \Sigma_s(E_1)}{\delta \Sigma_x(E)} + \frac{\Sigma_x(E)}{p(E_1 \to E_2, \Omega_1 \to \Omega_2)}\frac{\delta p(E_1 \to E_2, \Omega_1 \to \Omega_2)}{\delta \Sigma_x(E)} - \frac{\Sigma_x(E)}{\Sigma_t(E_1)}\frac{\delta \Sigma_t(E_1)}{\delta \Sigma_x(E)} - l_s \Sigma_x(E)\frac{\delta \Sigma_t(E_2)}{\delta \Sigma_x(E)} + \frac{\Sigma_x(E)}{\Sigma_t(E_2)}\frac{\delta \Sigma_t(E_2)}{\delta \Sigma_x(E)}$$

(2.51)

Note that Equation 2.51 assumes that $\delta l_s / \delta \Sigma_x(E)$ is equal to zero; this is not true because the pathlength is typically calculated by dividing a randomly-generated mean free path by the total cross section and $\delta \Sigma_t(E)/\delta \Sigma_x(E)$ is not equal to zero.

The derivative of some parameter Σ_y with respect to Σ_x is equal to one if the reaction x is included in the parameter Σ_y and is equal to zero otherwise; for example, $\delta \Sigma_s(r_1, E_1)/\delta \Sigma_s(r_1, E_2)$ is equal to zero, $\delta \Sigma_s(r_1, E_1)/\delta \Sigma_s(r_1, E_1)$ is equal to one, and $\delta \Sigma_t(r_1, E_1)/\delta \Sigma_s(r_1, E_1)$ is also equal to one because any change in the scattering cross section causes an equal change in the total cross section. Thus,

$$\frac{\delta \Sigma_t(r_1, E_1)}{\delta \Sigma_x(r, E)} = \delta_{r r_1} \delta_{E E_1} \delta_{\Sigma_t \Sigma_x},$$

(2.52)

where the Kronecker delta function, δ_{ij}, is equal to one if $i = j$, and is equal to zero if $i \neq j$. Note that the "modified" Kronecker delta function for $\delta_{\Sigma_t \Sigma_x}$ is equal to one if $\Sigma_x \in \Sigma_t$. These assumptions cause Equation 2.51 to reduce to

$$\alpha_s = \frac{\Sigma_x}{p_s}\frac{\delta p_s}{\delta \Sigma_x} = \left[\delta_{r r_1} \delta_{E E_1} \delta_{\Sigma_s \Sigma_x}\right] - \frac{\Sigma_x(E)}{\Sigma_t(E_1)}\left[\delta_{r r_1} \delta_{E E_1} \delta_{\Sigma_t \Sigma_x}\right] - l_s \Sigma_x(E)\left[\delta_{r r_s} \delta_{E E_2} \delta_{\Sigma_t \Sigma_x}\right] + \frac{\Sigma_x(E)}{\Sigma_t(E_2)}\left[\delta_{r r_2} \delta_{E E_2} \delta_{\Sigma_t \Sigma_x}\right].$$

(2.53)

The scattering probability term in Equation 2.51 is typically ignored, as indicated in Equation 2.53. The pathlength term in Equation 2.53 may encompass several different regions because collisions 1 and 2 may not take place in the same zone, and is then summed across each region separately. When α_s is multiplied by k_s in Equation 2.48 it is important to note that k_s is the eigenvalue contribution, or importance, that is

generated by the particle from point 1 on until the death of the particle. k_s is not the total eigenvalue estimate that is generated during the lifetime of the particle because the impact of the track *s* should not be weighted by any neutron generation that occurred before track *s*.

The contribution to the eigenvalue track-length estimator that is generated during track *s* is given by

$$k_s = w_s \bar{\nu} \Sigma_f(E_2) l_s \,, \tag{2.54}$$

thus,

$$\beta_s = \frac{\Sigma_x}{k_s} \frac{\delta k_s}{\delta \Sigma_x} = \frac{w_s \bar{\nu} \Sigma_f(E_2) l_s}{k_s} \left[\frac{\delta \Sigma_f(E_2)}{\delta \Sigma_x(E)} + \frac{\delta \bar{\nu}(E_2)}{\delta \Sigma_x(E)} \right], \tag{2.55}$$

where w_s is the weight of the particle during track *s*. Note that the Differential Operator method assumes that $\delta w_s / \delta \Sigma_x(E)$ is zero.

For calculating fission spectrum sensitivities, one can re-write Equation 2.54 such that

$$k_s = w_s \bar{\nu} \Sigma_f(E_2) l_s \sum_i^{All\ E} \chi(E_i) \,, \tag{2.56}$$

and thus when a particle is born with energy *E*

$$\beta_{\chi(E)} = \frac{\chi(E)}{k_{\chi(E)}} \frac{\delta k_{\chi(E)}}{\delta \chi(E)} = \chi(E) \frac{\delta \chi(E)}{\delta \chi(E)} \frac{k_s}{k_s} = \chi(E) \,. \tag{2.57}$$

Because the probability of recording a $\chi(E)$ sensitivity tally for a particle born at energy *E* is equal to $\chi(E)$, $\beta_{\chi(E)}$ becomes equal to one. Thus the unconstrained chi sensitivity

coefficient for neutrons born at energy E that generate $k_{\chi(E)}$ fissions from birth until death is given by

$$\frac{\delta k}{\delta \chi(E) / \chi(E)} = \frac{1}{N} \sum_{i=1}^{N} k_{\chi(E)} \, .$$

(2.58)

2.3.2 Differential Operator Methodology Evaluation

The Differential Operator method provides a fast and efficient way to generate sensitivity coefficients that requires no flux mesh. Because α_s and β_s for a collision are multiplied by the number of fissions created by the particle from track s until death, one must tally the number of fissions generated by each particle track and "go back in time" to weight the sensitivity coefficient tallies by these values. Thus the Differential Operator method requires one to store information for every collision (the energy and location of the collision, and the track length tallies generated between the current and previous collision) until the particle dies. Fortunately this is not an overwhelming amount of data to store because particles typically undergo on the order of 100 collisions until being killed and because the data is freed once the particle dies. The amount of memory required by the Differential Operator method with a maximum estimate of 400 collisions per particle for a hypothetical full-core sensitivity calculation similar to that found in Reference 18 is

$$\begin{aligned} 38{,}000 \; & unique \; isotope - regions \times 12 \; reactions \; per \; isotope \\ & \times 400 \; collisions \; per \; particle \; \times 8 \; bytes \; per \; double \\ & = 1.46 \; gigabytes \; of \; memory \, . \end{aligned}$$

(2.59)

It has been stated that the performance a Monte Carlo code degrades by 10-20% for each isotope that is perturbed using the Differential Operator method, but such performance degradation was not seen for the cases examined in this dissertation [4].

The Differential Operator method achieves its low runtime and memory requirements by accepting sacrifices in the accuracy of its sensitivity coefficients. Because it only takes the first-order derivative of the eigenvalue to calculate sensitivity coefficients, the Differential Operator method ignores all second-order perturbation effects. Ignoring the second-order effects is exacerbated by the Differential Operator method's lack of adjoint-weighted tallies. While it is possible for the Differential Operator method to account for second-order effects by calculating the $\delta^2 k / \delta \Sigma_x{}^2$ term, the cross-section covariance matrices do not account for second-order effects and cannot use second-order sensitivity coefficients to calculate σ_k [19]. Methods have been developed to improve the accuracy of the Differential Operator method through improved quantification of the fission source sensitivity coefficients, but these methods will not be examined in this research because they are very similar to the approach taken by the Iterated Fission Probability method, which will be discussed in detail. The Differential Operator method was previously implemented in the MCNP Monte Carlo code, and has recently been replaced by the Iterated Fission Probability method [5].

2.4 Iterated Fission Probability Methodology

2.4.1 Method Description and Derivation

The Iterated Fission Probability (IFP) method computes adjoint-weighted tallies by observing that the importance of a neutron is proportional to the population of neutrons existing in some future generation that are progeny of the original neutron [5] [7]. As shown in Figure 2.3, after some initial neutron, known as a progenitor, causes a fission event the Iterated Fission Probability method tracks the "fission chain" of progeny of the initial progenitor particle for a number of generations.

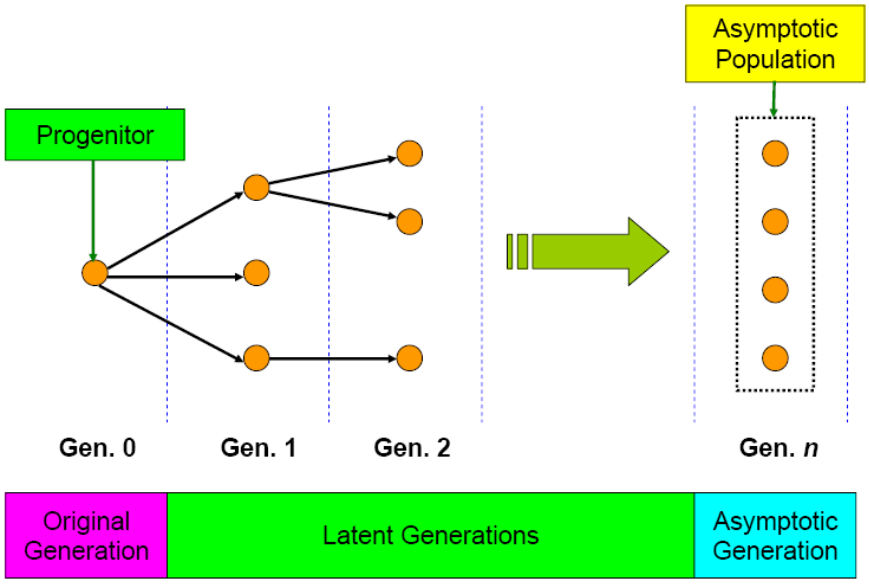

Figure 2.3: The fission chain of a progenitor [5].

After the progeny have undergone a sufficient number of generations to establish a well-distributed population of progeny in the system, the number of fission neutrons that are created by that final generation of progeny, known as the asymptotic population of the progenitor, is calculated as [5]

$$\pi_p = \sum_{\tau \epsilon p} \sum_{s} w_s \bar{\upsilon} \Sigma_f l_s \,, \tag{2.60}$$

where τ is the index for the neutrons in the asymptotic generation created by progenitor p and s is the set of paths traveled by each neutron. The number of latent generations required before calculating the asymptotic population for a progenitor is system dependent, and can range anywhere from zero generations for systems with flat importance profiles to more than 20 generations for complex systems or conservative calculations [20].

Because the asymptotic population is a measure of importance and is proportional to Φ^*, it can replace Φ^* in Equations 2.11 through 2.14. Calculating the C_x term in Equation 2.11 is done by multiplying the asymptotic population for the progenitor by the tracklength-calculated flux generated in all regions at all energies from the time of the

neutron's birth until when it creates progenitor *p*; this implies that all of the collisions a neutron sees from birth until it creates progenitor *p* have equal importance because all of the collisions result in the same asymptotic population. If a neutron creates two fission chains, p and p^*, then it is possible for some pathlengths to contribute multiple times to the sensitivity coefficient tallies, although one set is weighted by π_p and the other by π_{p^*}. When used in continuous-energy codes, the Iterated Fission Probability method tallies different reaction rates in lieu of tallying the neutron flux and groups these reaction rates into multigroup bins. Because sensitivity coefficients require tallies as a function of isotope and reaction, the multigroup reaction rates must be stored as a function of isotope and reaction when calculating the asymptotic population of a progenitor, which results in an increase in the memory requirements for the problem.

Because the forward and adjoint flux terms for C_s in Eq. 15 are correlated by the double-differential scattering probability *at the location* of a collision, flux tallies for C_s are not calculated using pathlength flux estimators, but instead with the collisional flux estimator [12],

$$\Phi(r,E,\Omega) = \frac{w_s}{\Sigma_t(r,E)} \frac{1}{N\Delta V \Delta E \Delta\Omega}. \tag{2.61}$$

The tally that is recorded for a given collision when tallying scattering sensitivity coefficients is equal to

$$Score\ for\ C_s(E \to E') = \Sigma_s(r,E)\Phi\left(r,E,\hat{\Omega}\right)\Phi^*\left(r,E',\hat{\Omega}'\right) = w_s \frac{\Sigma_s(r,E)}{\Sigma_t(r,E)} \frac{\pi_p}{N\Delta V \Delta E \Delta\Omega}. \tag{2.62}$$

The probability that the neutron scatters at the site of the collision is equal to $\frac{\Sigma_s(r,E)}{\Sigma_t(r,E)}$ and the use of implicit capture already weights the asymptotic population by $\frac{\Sigma_s(r,E)}{\Sigma_t(r,E)}$ after a collision, thus it is not necessary to weight the scattering sensitivity score by $\frac{\Sigma_s(r,E)}{\Sigma_t(r,E)}$. Furthermore, the neutron emerging from the collision is already weighted by w_s, and thus the asymptotic population is already weighted by w_s and it is not necessary to weight the

scattering sensitivity score by w_s. Thus, the score recorded at the site of a collision for the scattering sensitivity coefficient is simply π_p.

The forward flux terms for C_f and D in Equations 2.12 and 2.14 are also calculated using collisional flux estimators because fission points can only be created at the site of a collision. The score tallied when calculating C_f and D is given by

$$Score = \bar{\upsilon}\Sigma_f(r,E)\Phi(r,E,\Omega)\Phi^*(r,E,\Omega) = w_s \frac{\bar{\upsilon}\Sigma_f(r,E)}{\Sigma_t(r,E)} \frac{\pi_p}{N\Delta V \Delta E \Delta\Omega}. \tag{2.63}$$

Because C_f and D should be calculated at every collision and the probability of a collision actually causing a fission is equal to $w_s \frac{\bar{\upsilon}\Sigma_f(r,E)}{\Sigma_t(r,E)}$, the tally that is scored for calculating C_f and D is once again π_p.

2.4.2 Iterated Fission Probability Methodology Evaluation

The Iterated Fission Probability method provides a very accurate way for calculating adjoint-weighted sensitivity coefficients without significantly slowing down the Monte Carlo simulation or using a spatial mesh [5] [20]. However, the Iterated Fission Probability method faces challenges with memory management because it must store reaction rates and data from collisions for every particle for up to 20 generations before the asymptotic population is reached and tallies are calculated. An Iterated Fission Probability simulation that generates sensitivity coefficients as a function of energy for various nuclides in a complex system must store on the order of

$$\begin{aligned} 38{,}000\ &unique\ isotope-regions\ \times 12\ reactions\ per\ isotope \\ &\times 44\ energy\ groups\ \times\ 21\ generations\ of\ storage \\ &\times 10{,}000\ particles\ per\ generation\ \times 8\ bytes\ per\ double \\ &= 33{,}707.5\ gigabytes\ of\ memory\ . \end{aligned} \tag{2.64}$$

One must store 21 generations of data to account for data collection from the 20 latent generations and the progenitor's initial generation. Often IFP calculations do not require 20 latent generations to obtain an accurate estimate for the asymptotic population

produced by an event, and the number of latent generations used by the Iterated Fission Probability method should be minimized when calculating sensitivity coefficients; this will be discussed in detail in Chapter 3.9. As indicated in Equation 2.64, the Iterated Fission Probability method faces challenges with memory usage when modeling complex systems that scale directly with the number of particles simulated in each generation. One possible way to alleviate these memory issues is to run separate Monte Carlo calculations on different processors using the Iterated Fission Probability method, each with a much lower number of particles per generation, and to combine the results from the runs after they finish. Unfortunately, running too few particles per generation has the effect of biasing the Monte Carlo solution and fission source convergence, and can produce erroneous results [21].

Progenitors tracked by the Iterated Fission Probability method must have fission chains of progeny that survive for up to 20 generations before tallies for those progenitors are recorded; if a neutron in the fission chain leaks from the system or fails to cause a fission, then that fission chain is destroyed and the asymptotic population returns a tally of zero. Thus the efficiency of the Iterated Fission Probability method is inferior to that of the Differential Operator method because not every fission chain results in a non-zero sensitivity coefficient tally but almost every neutron collision contributes to sensitivity coefficient tallies in a Differential Operator simulation.

2.5 Contributon Methodology

2.5.1 Method Description and Derivation

The Contributon methodology, which was developed by Mark Williams et. al. for shielding calculations, determines the importance of a neutron at a collision by creating and simulating secondary particles at the site of the collision [8]. After allowing these secondary particles to undergo random walks and terminate, the importance of the initial collision is determined by tallying how many fission neutrons are created by each secondary particle. This process is described graphically in Figure 2.4. The Contributon method requires a very small amount of memory to calculate sensitivity coefficients because it determines the importance of each collision before allowing the initiating

particle to continue onto its next collision, but causes a large increase in the runtime for a problem as the number of secondary particles that must be simulated is typically much, much larger than the number of forward neutrons that are simulated.

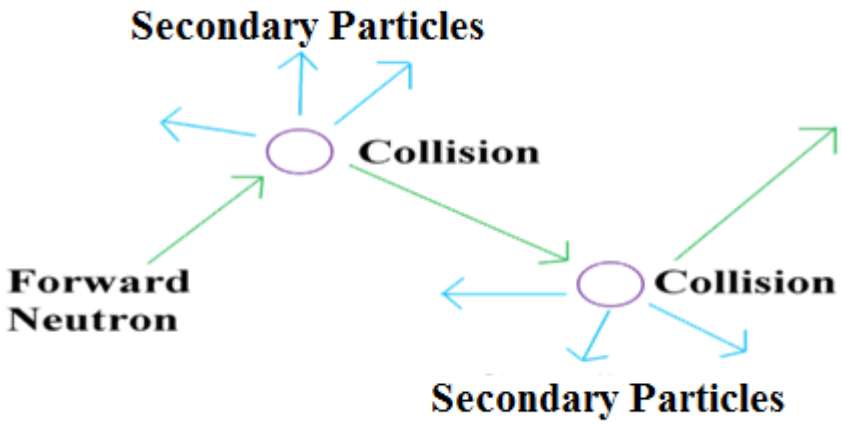

Figure 2.4: Illustration of the Contributon process.

Consider a neutron source Q that is equal to the fission source of a system

$$Q = \lambda F \phi \, .$$

(2.65)

Multiplying Equation 2.65 by the adjoint flux and integrating over phase space gives

$$\langle \phi^* Q \rangle = \lambda \langle \phi^* F \phi \rangle \, .$$

(2.66)

Consider now a neutron emitted in phase space τ_s such that $Q = Q_s \, \delta(\tau - \tau_s)$. Typically Q_s is the weight of the particle in phase space τ_s. This source definition causes Equation 2.66 to be reduced to a form where the importance of the neutron in phase space τ_s can be calculated by

$$\phi^*(\tau_s) = \frac{\lambda}{Q_s} \int_V G(\tau_s \rightarrow r) F^*(r) \, dr \, ,$$

(2.67)

where the transfer function $G(\tau_s \rightarrow r)$ is equal to the expected number of fission neutrons generated in all energies and directions at r due to a source neutron emitted at phase space τ_s and is given by

$$G(\tau_s \rightarrow r) = \frac{1}{Q_s(\tau_s)} \int_E \int_\Omega \nu\Sigma_f(r,E)\phi(r,E,\Omega \mid Q(\tau_s))d\Omega dE \,, \tag{2.68}$$

where $\phi(r,E,\Omega \mid Q(\tau_s))$ is the flux created in phase space (r,E,Ω) due to the source $Q(\tau_s)$. The function $F^*(r)$ is equal to the expected importance generated by a fission neutron emitted at r and is given by

$$F^*(r) = \int_E \int_\Omega \frac{\chi(r,E)}{4\pi} \phi^*(r,E,\Omega)d\Omega dE \,. \tag{2.69}$$

2.5.2 Contributon Methodology Evaluation

Because Equations 2.11 through 2.14 contain forward and adjoint flux terms with three different sets of phase space coordinates, three different secondary particles must be simulated at the site of every collision to tally the importance of that collision. To calculate C_x, one particle is simulated with the same energy and direction as the particle entering the collision at r. To calculate the C_s term one particle is simulated with energy and direction equal to that of the particle emerging from the collision at r. Lastly, to calculate the fission terms C_f and D a particle is simulated with a random direction and an energy that is sampled from the $\chi(E)$ distribution. Depending on the system, a neutron will undergo 10's to 100's of collisions during its lifetime, which can impose a great computational burden and can increase the runtime of a problem by **a factor of hundreds**. Although this runtime increase seems enormous, it is not necessarily prohibitive for performing sensitivity coefficient calculations. Performing sensitivity coefficient calculations using conventional TSUNAMI requires a significant amount of man-hours because the researcher must ensure that the flux mesh is sufficiently-refined to

calculate accurate sensitivity coefficients. In many cases it is more efficient to simulate a Contributon calculation in a single run using a large computing cluster than to spend the time fine-tuning the TSUNAMI-3D flux mesh.

Contributon methodology also requires calculation of the $F^*(r)$ term, which is equal to the average importance generated by a fission neutron emitted at r. Although the Contributon method itself does not require a mesh, the calculation and storage of $F^*(r)$ currently requires a spatial mesh, as discussed in detail in Chapter 4. Currently TSUNAMI-3D contains an option to calculate sensitivity coefficients using Contributon methodology with the assumption that $F^*(r)$ is equal to one everywhere. In general this approximation gives reasonable answers, but this assumption creates noticeable inaccuracies for the sensitivity coefficients of some systems, as discussed in Chapter 4 [17].

The lack of a spatial mesh (except for the $F^*(r)$ term) causes the Contributon method to have small memory requirements, as shown below for a sample problem.

$$38{,}000\ unique\ isotope-regions \times 12\ reactions\ per\ isotope \times 44\ energy\ groups \times 8\ bytes\ per\ double = 0.16\ gigabytes\ of\ memory\,. \tag{2.70}$$

As shown in Equation 2.70, the Contributon method only requires enough memory to store the sensitivity coefficients for different isotopes as a function of energy and reaction, and thus requires the minimum amount of memory possible for storing sensitivity coefficient tallies. Storing the $F^*(r)$ term requires some additional memory, but requires significantly less memory than storing an equally-refined Conventional TSUNAMI mesh due to the lack of energy and angular dependence in the $F^*(r)$ term; storing $F^*(r)$ on a spatial mesh that is equally refined as the mesh in Equation 2.44 for the Conventional TSUNAMI methodology only requires 32 megabytes of memory instead of the 182.8 gigabytes required for the TSUNAMI mesh.

The Contributon method also has the ability to obtain sensitivity coefficient tallies for rare reactions. Consider for example a fast, high-leakage, metal system where one wants to obtain the fast-to-thermal scattering sensitivities; the extremely fast nature of the problem means that very few neutrons scatter to thermal energies, but that very small

number of thermal neutrons may have a very high importance and contribute significantly to the eigenvalue uncertainty. The Differential Operator and Iterated Fission Probability methods cannot tally these rare fast-to-thermal scatter reactions because they calculate sensitivity coefficients by examining the interactions and behavior of forward neutrons and do not interrupt the simulation's random number sequence by simulating secondary particles. The Contributon method allows one to obtain tallies for these rare reactions by simply simulating particles with thermal energies at the site of a collision and weighting the importance estimations for these particles by $p_s(fast \rightarrow thermal)$. However, simulating secondary particles at thermal energies sacrifices the efficiency of fast neutron sensitivity tallies to improve the efficiency for these rare reaction sensitivities.

2.6 CLUTCH Methodology

2.6.1 Method Description and Derivation

An improved method for sensitivity coefficient calculation has been derived based on Contributon theory. This method, which shall be known as the **C**ontributon-**L**inked eigenvalue sensitivity/**U**ncertainty estimation via **T**racklength importance **CH**aracterization (CLUTCH) method, preserves the Contributon method's mesh-free, memory-efficient approach for calculating adjoint-weighted tallies, and circumvents the need to simulate any contributon particles by instead examining the random walks of forward neutrons. Consider a neutron following the random walk shown in Figure 2.5.

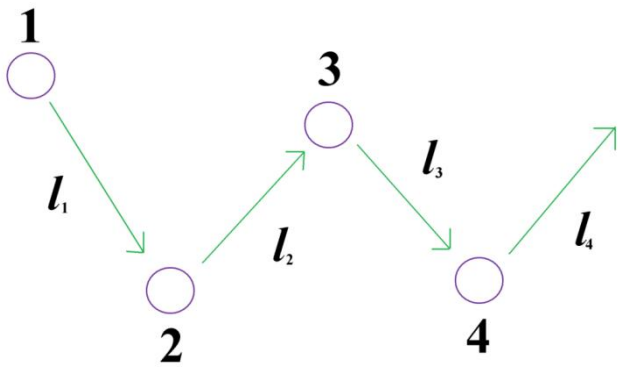

Figure 2.5. A random walk for a sample neutron.

The Contributon method determines $G(\tau_s \rightarrow r)$ in Equation 2.67 for a neutron in phase space τ_s by simulating secondary particles in the phase space τ_s and tracking how many fission neutrons, weighted by $F^*(r)$, each secondary particle creates. The CLUTCH method determines $G(\tau_s \rightarrow r)$ by instead tracking how many fission neutrons are created by the primary neutron after the reaction of interest. Thus the CLUTCH method is similar to the Differential Operator method in that it stores information about each neutron collision and looks "forward in time" to determine the importance of every collision. To calculate C_s at a collision one must determine the importance created by the neutron emerging from the scattering event; thus

$$\begin{aligned}
\Phi^*_{C_s}(\tau_2) &= \frac{\lambda}{w_2}\left[w_2\bar{\nu}\Sigma_{f_2}\Gamma^*(l_2) + w_3\bar{\nu}\Sigma_{f_3}\Gamma^*(l_3) + w_4\bar{\nu}\Sigma_{f_4}\Gamma^*(l_4) + \ldots\right] \\
\Phi^*_{C_s}(\tau_3) &= \frac{\lambda}{w_3}\left[w_3\bar{\nu}\Sigma_{f_3}\Gamma^*(l_3) + w_4\bar{\nu}\Sigma_{f_4}\Gamma^*(l_4) + \ldots\right] \\
\Phi^*_{C_s}(\tau_4) &= \frac{\lambda}{w_4}\left[w_4\bar{\nu}\Sigma_{f_4}\Gamma^*(l_4) + \ldots\right],
\end{aligned} \tag{2.71}$$

where

$$\Gamma^*(l) = \int_l F^*(r)dr\,. \tag{2.72}$$

Because the score that is tallied for C_s at point 2 is calculated using a collisional flux estimate and implicit capture states that $\frac{w_2}{w_1} = \frac{\Sigma_s(r_1,E_1)}{\Sigma_t(r_1,E_1)}$, the score for C_s at point 2 is given by

$$Score\ C_s(z, E \to E') = \Sigma_s(r_1, E_1)\phi(\tau_1)\phi^*(\tau_2) = \frac{w_1\Sigma_s(r_1, E_1)}{\Sigma_t(r_1, E_1)}\frac{\lambda}{w_2}\int_V G(\tau_2 \to r)F^*(r)\,dr$$

$$= \lambda \int_V G(\tau_2 \to r)F^*(r)\,dr$$

$$= \lambda\left[w_2\bar{\nu}\Sigma_{f_2}\mathrm{F}^*(l_2) + w_3\bar{\nu}\Sigma_{f_3}\mathrm{F}^*(l_3) + w_4\bar{\nu}\Sigma_{f_4}\mathrm{F}^*(l_4) + \ldots\right].$$

(2.73)

The Contributon method simulates secondary particles at every collision in fissionable material to tally C_f and D, but this is not possible under the CLUTCH methodology because not every neutron collision creates a fission point. The probability that a collision at point 2 causes a fission and that the fission point is sampled in the next generation, emitting a neutron of energy E', is given by

$$p = w_1\lambda'\frac{\bar{\upsilon}\Sigma_f(r_1, E_1)}{\Sigma_t(r_1, E_1)}\chi(E'),$$

(2.74)

where the factor λ' ensures that the same weight of fission neutrons are sampled in each generation and is equal to the number of fission points created for the current generation divided by the total weight of neutrons that are sampled per generation; it should be noted that λ' is an estimate for λ for an individual generation. The tally that is stored for C_f and D for the collision at point 2 is given by

$$Score\ for\ C_f(z, E \to E') = \bar{\upsilon}\Sigma_f(r_1, E_1)\phi(\tau_1)\phi^*\left(r_1, E', \hat{\Omega}'\right)\chi(E')$$

$$= \lambda'\frac{w_1\Sigma_s(r_1, E_1)}{\Sigma_t(r_1, E_1)}\chi(E')\frac{\lambda}{w_0}\int_V G(\tau_0 \to r)F^*(r)\,dr.$$

(2.75)

where w_0 is the weight of the fission neutron with energy E' at birth; typically this weight is equal to one, but is equal to λ for codes such as Shift that sample every fission site regardless of the number of fission sites produced in the previous generation. Because not every collision contributes towards the tally for C_f and D, each score and must be

divided by the probability of the collision contributing; thus Equation 2.75 is divided by Equation 2.74 to give

$$Score\ for\ C_f(z, E \to E') = \bar{\upsilon}\Sigma_f(r_1, E_1)\phi(\tau_1)\phi^*(r_1, E', \hat{\Omega}')\chi(E')$$
$$= \lambda \int_V G(\tau_0 \to r)F^*(r)\, dr. \tag{2.76}$$

Note that $G(\tau_0 \to r)$ is tallied from the time a neutron is born until it dies. The CLUTCH and the Differential Operator methods produce identical estimates for the chi sensitivity coefficient if one assumes that $F^*(r)$ is equal to one everywhere.

Producing an estimate for C_x is more challenging than estimating C_s, C_f, or D because estimating C_x requires one to calculate the importance for a neutron at a collision by simulating a neutron at the site of the collision as if the collision never occurred; it is not possible for the CLUTCH method to calculate C_x using a collisional estimator for the flux tally because the direction of a neutron must change at the site of each collision. Consider instead a segment of pathlength for a particle traveling between two collisions, as shown in Figure 2.6.

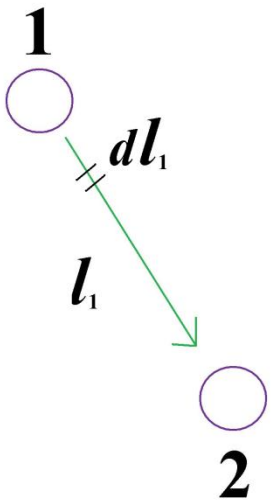

Figure 2.6: Tallying C_x using a flux pathlength estimator.

Calculating $G(\tau_s \rightarrow r)$ for the differential segment dl_1 in Figure 2.6 using a pathlength estimator for the importance, as is done for the C_s, C_f, and D tallies, involves tallying the number of fissions created from dl_1 to point 2, and then from point 2 until the particle's death; it is difficult to use a pathlength estimator to tally C_x because every differential segment produces a different estimate for $G(\tau_s \rightarrow r)$ if the material is fissile. However, the tally for $G(\tau_s \rightarrow r)$ is constant for all points on line l_1 if a collisional estimator is instead used to tally $G(\tau_s \rightarrow r)$. Thus, the importance calculated for C_x in Figure 2.5 using a tracklength estimator for the forward flux and a collisional estimator for $G(\tau_s \rightarrow r)$ is given by

$$\begin{aligned}
\phi^*(\tau_1) &= \frac{\lambda}{w_1}\left[w_1\left(\frac{\nu\Sigma_f}{\Sigma_t}\right)_2 F^*(r_2) + w_2\left(\frac{\nu\Sigma_f}{\Sigma_t}\right)_3 F^*(r_3) + w_3\left(\frac{\nu\Sigma_f}{\Sigma_t}\right)_4 F^*(r_4) + \ldots\right] \\
\phi^*(\tau_2) &= \frac{\lambda}{w_2}\left[w_2\left(\frac{\nu\Sigma_f}{\Sigma_t}\right)_3 F^*(r_3) + w_3\left(\frac{\nu\Sigma_f}{\Sigma_t}\right)_4 F^*(r_4) + \ldots\right] \\
\phi^*(\tau_3) &= \frac{\lambda}{w_3}\left[w_3\left(\frac{\nu\Sigma_f}{\Sigma_t}\right)_4 F^*(r_4) + \ldots\right].
\end{aligned} \tag{2.77}$$

And the score for C_x during track l_1 is given by

$$\begin{aligned}
Score\ for\ C_x(z,E) &= \Sigma_x(r_1,E_1)\phi(\tau_1)\phi^*(\tau_1) \\
&= \Sigma_x(r_1,E_1)\, w_1 l_1\, \frac{\lambda}{w_1}\int_V G(\tau_1 \rightarrow r)F^*(r)\, dr \\
&= \lambda\Sigma_x(l_1,E_1)l_1\left[w_1\left(\frac{\nu\Sigma_f}{\Sigma_t}\right)_2 F^*(r_2) + w_2\left(\frac{\nu\Sigma_f}{\Sigma_t}\right)_3 F^*(r_3)\right. \\
&\quad \left. + w_3\left(\frac{\nu\Sigma_f}{\Sigma_t}\right)_4 F^*(r_4) + \ldots\right].
\end{aligned} \tag{2.78}$$

2.6.2 CLUTCH Methodology Evaluation

The CLUTCH method allows for the calculation of adjoint-weighted sensitivity coefficients without simulating contributon particles or using a flux mesh. Like the Contributon method, the CLUTCH method requires a spatial mesh for calculating and storing $F^*(r)$, but this mesh only occupies a few megabytes of memory, as previously discussed. The CLUTCH method requires the storage of reaction rates as a function of material, and reaction for each track of a particle's lifetime, and requires the same amount of memory storage as the Differential Operator method. Thus the amount of memory required by the CLUTCH method for a typical problem is given by

$$\begin{aligned} 38{,}000\ &unique\ isotope-regions \times 12\ reactions\ per\ isotope \\ &\times 400\ collisions\ per\ particle\ \times 8\ bytes\ per\ double \\ &= 1.46\ gigabytes\ of\ memory\ . \end{aligned} \tag{2.79}$$

The greatest limitation of the CLUTCH method is the need to calculate $F^*(r)$ before tallying sensitivity coefficients. The current approach for tallying $F^*(r)$ involves scoring tallies during the inactive generations allocated for fission source convergence because tallying $F^*(r)$ does not require a converged fission source term; developing an efficient approach for calculating $F^*(r)$ can greatly affect the efficiency of the CLUTCH method, and is discussed in Chapter 4.

2.7 Contributon-IFP Hybrid Methodology

A new approach for calculating eigenvalue sensitivity coefficients has been developed by combining the IFP methodology with the Contributon notion of simulating secondary particles. Instead of storing reaction rates for up to 20 generations when a particle causes a fission event, the Contributon-IFP Hybrid method simulates several generations of secondary particles to estimate the original particle's asymptotic population before that particle is allowed to continue its random walk [9]. This results in a sensitivity coefficient method that does not need to obtain the $F^*(r)$ weighting function used by the Contributon method and does not suffer from the large memory requirements

of the IFP method; in fact, the Contributon-IFP Hybrid method has the same small memory requirements given for the Contributon method in Equation 2.70. Although the Contributon-IFP hybrid method accesses the advantages of the Contributon and IFP methods, its efficiency suffers from the disadvantages inherent to the two methods: the Contributon-IFP Hybrid method suffers the computational burden of simulating secondary particles, and any breaks in the fission chains for these secondary particles returns an importance estimate of zero, which increases the variance of the method's sensitivity coefficient estimates.

Chapter III

Sensitivity Coefficient Calculation Results

The Differential Operator, Iterated Fission Probability, Contributon, CLUTCH, and Contributon-IFP Hybrid methods for calculating eigenvalue sensitivity coefficients were implemented in the Shift Monte Carlo code and used to calculate sensitivity coefficients for six test problems. Development of the Shift continuous-energy physics package was not completed during the time of this research, and all sensitivity calculations in this dissertation are obtained from multigroup calculations. Although Shift's lack of a continuous-energy physics package prevents a full evaluation of the accuracy and performance of the sensitivity coefficient methodologies for continuous-energy applications, these multigroup calculations should suffice as a proof of principle for the new sensitivity coefficient methods and furthermore will allow the methods to be compared with similar TSUNAMI-3D calculations. Because Shift's multigroup physics package does not store microscopic cross sections, the sensitivity coefficients presented in this dissertation are macroscopic, or material-averaged, sensitivity coefficients. Shift's multigroup physics package currently allows for only P0 scattering kinematics, and thus all sensitivity calculations presented in this dissertation used P0 scattering kinematics. Cross sections for all calculations were obtained using the ENDF-V 44-group cross section library in SCALE and the CSAS-I cross section generation sequence of the SCALE code package [1]. All TSUNAMI-3D calculations in this study used an S_{10}

quadrature set to calculate sensitivity coefficients. The energy group structure used in these multigroup calculations is given in Table 3.1 [1].

Table 3.1: Energy bin structure for multigroup calculations [1]

Energy Group	Energy Range	Energy Group	Energy Range
1	2.0000 10^{7} eV - 8.1873 10^{6} eV	23	3.0000 eV - 1.7700 eV
2	8.1873 10^{6} eV - 6.4340 10^{6} eV	24	1.7700 eV - 1.0000 eV
3	6.4340 10^{6} eV - 4.8000 10^{6} eV	25	1.0000 eV - 6.2500 10^{-1} eV
4	4.8000 10^{6} eV - 3.0000 10^{6} eV	26	6.2500 10^{-1} eV - 4.0000 10^{-1} eV
5	3.0000 10^{6} eV - 2.4790 10^{6} eV	27	4.0000 10^{-1} eV - 3.7500 10^{-1} eV
6	2.4790 10^{6} eV - 2.3540 10^{6} eV	28	3.7500 10^{-1} eV - 3.5000 10^{-1} eV
7	2.3540 10^{6} eV - 1.8500 10^{6} eV	29	3.5000 10^{-1} eV - 3.2500 10^{-1} eV
8	1.8500 10^{6} eV - 1.4000 10^{6} eV	30	3.2500 10^{-1} eV - 2.7500 10^{-1} eV
9	1.4000 10^{6} eV - 9.0000 10^{5} eV	31	2.7500 10^{-1} eV - 2.5000 10^{-1} eV
10	9.0000 10^{5} eV - 4.0000 10^{5} eV	32	2.5000 10^{-1} eV - 2.2500 10^{-1} eV
11	4.0000 10^{5} eV - 1.0000 10^{5} eV	33	2.2500 10^{-1} eV - 2.0000 10^{-1} eV
12	1.0000 10^{5} eV - 2.5000 10^{4} eV	34	2.0000 10^{-1} eV - 1.5000 10^{-1} eV
13	2.5000 10^{4} eV - 1.7000 10^{4} eV	35	1.5000 10^{-1} eV - 1.0000 10^{-1} eV
14	1.7000 10^{4} eV - 3.0000 10^{3} eV	36	1.0000 10^{-1} eV - 7.0000 10^{-2} eV
15	3.0000 10^{3} eV - 5.5000 10^{2} eV	37	7.0000 10^{-2} eV - 5.0000 10^{-2} eV
16	5.5000 10^{2} eV - 1.0000 10^{2} eV	38	5.0000 10^{-2} eV - 4.0000 10^{-2} eV
17	1.0000 10^{2} eV - 3.0000 10^{1} eV	39	4.0000 10^{-2} eV - 3.0000 10^{-2} eV
18	3.0000 10^{1} eV - 1.0000 10^{1} eV	40	3.0000 10^{-2} eV - 2.5300 10^{-2} eV
19	1.0000 10^{1} eV - 8.1000 eV	41	2.5300 10^{-2} eV - 1.0000 10^{-2} eV
20	8.1000 eV - 6.0000 1000 eV	42	1.0000 10^{-2} eV - 7.5000 10^{-3} eV
21	6.0000 eV - 4.7500 eV	43	7.5000 10^{-3} eV - 3.0000 10^{-3} eV
22	4.7500 eV - 3.0000 eV	44	3.0000 10^{-3} eV - 1.0000 10^{-5} eV

Reference sensitivity coefficients were obtained through direct perturbation Shift calculations, in which the various neutron cross sections and physics parameters of interest were perturbed and a corresponding set of perturbed eigenvalues was gathered. The parameter perturbations used in this study were ± 2% and ± 4%, and the perturbed eigenvalues were used to calculate sensitivity coefficients using weighted linear regression. In many cases these perturbations were not sufficiently large to give reliable estimates of the sensitivity coefficients, and only perturbation regression fits with coefficients of determination that were greater than 0.90 were included as reference

sensitivity coefficients. Perturbations larger than 2% and 4% could have been used to generate direct perturbation sensitivity coefficients, but were not used to avoid any second-order effects that may have arisen from by larger perturbations. Because the criteria of having a strong regression fit greatly reduced the number of available reference sensitivity coefficients, an additional set of reference sensitivity coefficients was generated for each problem by performing an Iterated Fission Probability calculation using 20 latent generations; these reference cases will be referred to as IFP-20 throughout this chapter. To evaluate the accuracy of each sensitivity method, each method's sensitivities were compared with the references' sensitivities, and difference between the two (in terms of the number of effective standard deviations) was calculated. An uncertainty of 5×10^{-13} was included when calculating the effective standard deviation for the difference between two sensitivity coefficients to account for the fact that SHIFT only gave sensitivity coefficients to 6 digits past the decimal place. The sum of the squares of the sensitivity coefficient differences was collected to generate a χ^2 coefficient, which was then used to obtain a p-value for the equivalence of the different methods. Only sensitivity coefficients with an absolute value larger than 10^{-5} were included in this calculation to reduce the effect of round-off error and to ensure that the sensitivity coefficients that were examined had well-converged variance estimates.

Unless otherwise noted, the Monte Carlo calculations for each problem simulated the same number of active neutron histories, and all simulations typically used 5,000 particles per generation. Each simulation included 200 inactive neutron histories to allow for full fission source convergence [21]. The efficiency of each sensitivity calculation was determined by calculating the energy-integrated, material-averaged Figure of Merit (FoM) for each sensitivity coefficient. A commonly-used metric to evaluate the performance of Monte Carlo simulations, the Figure of Merit is defined as

$$FoM = \frac{1}{R^2 T}, \tag{3.1}$$

where R is the relative error for the parameter of interest and T is the simulation runtime [12]. All FoM presented in this study have units of s^{-1}.

A list of the problems examined in this study, as well as a brief description and nickname for each problem is given in Table 3.2. These problems were selected to form a small but representative set of criticality safety problems with various fuel materials, absorber materials, reflector materials, and boundary conditions, and include several well-known problems for criticality safety applications.

Table 3.2: Problems examined using different sensitivity coefficient methods

Model	Nickname	Description
Infinitely-Reflected PWR Pin Cell	Fuel Pin	An infinitely-reflected, 2.7% enriched PWR pin cell [22].
Godiva	Godiva	A highly-enriched uranium metal sphere with vacuum boundary conditions [23].
MIX-COMP-THERM-004-001	MCT	A benchmark experiment for the validation of criticality safety calculations for a shipping cask containing an unsymmetrical array of MOX fuel is partially flooded by water [23].
PU-SOL-THERM-014 Case 30	PST	Four steel cylinders containing a Pu-nitrate solution arranged in a rectangle within a concrete room [23].
LEU-COMP-THERM-050 Case 14	LCT	An irregular 25x25 array of fuel pins partially submersed in water and surrounding a solution containing dissolved samarium [23].
Full-Core PWR	PWR	A 2D, full-core model of a PWR with three enrichments of UO2 fuel [22].

Determining the necessary number of latent generations for the Iterated Fission Probability calculations and the necessary $F^*(r)$ mesh refinements for Contributon-based calculations for each problem is discussed in detail in chapters 3.8 and 4, respectively. The PWR problem was selected as a challenge problem and the necessary $F^*(r)$ mesh refinement and necessary number of latent generations for IFP calculations were not pre-determined for this problem; instead, sensitivity coefficients were calculated for this problem using the lessons learned from chapters 3.8 and 4. The Iterated Fission Probability calculations in this Chapter are often referred to as "*IFP-X*," where *X* is the number of latent generations used in the calculation. The Contributon-IFP Hybrid calculations for each case used the same number of latent generations when simulating

secondary neutron fission chains as was used by the corresponding IFP calculation for the corresponding case.

3.1 Infinitely-Reflected PWR Pin Cell Results

The first problem used for evaluating the sensitivity coefficient methods was an infinitely-reflected model of a 2.7%-enriched fuel pin lattice cell from the PWR model discussed in chapter 3.6. Unlike the full-core PWR model, the Fuel Pin model contained only fuel and moderator regions, and did not include the fuel clad. The case modeled a quarter of the fuel pin lattice cell to take advantage of the X- and Y- symmetry present in the cell. Figures 3.1 through 3.5 graph the fuel absorption, scatter, fission, $\bar{\nu}$, and constrained chi sensitivity coefficients, respectively, and Figures 3.6 and 3.7 show the moderator absorption and scatter sensitivity coefficients, respectively. The "Reference" sensitivity coefficients in the figures give the sensitivity coefficients that were calculated by the IFP-20 simulation. The sensitivity coefficients in these figures have been integrated over the energy range for each energy group used in the simulation. One-sigma error bars are included in these and all sensitivity coefficient plots, but are often invisible because the sensitivity coefficient uncertainties were typically very small. The absorption sensitivity coefficients presented here and throughout this dissertation account for the eigenvalue sensitivity due to the removal of neutrons from both fission and parasitic capture reactions.

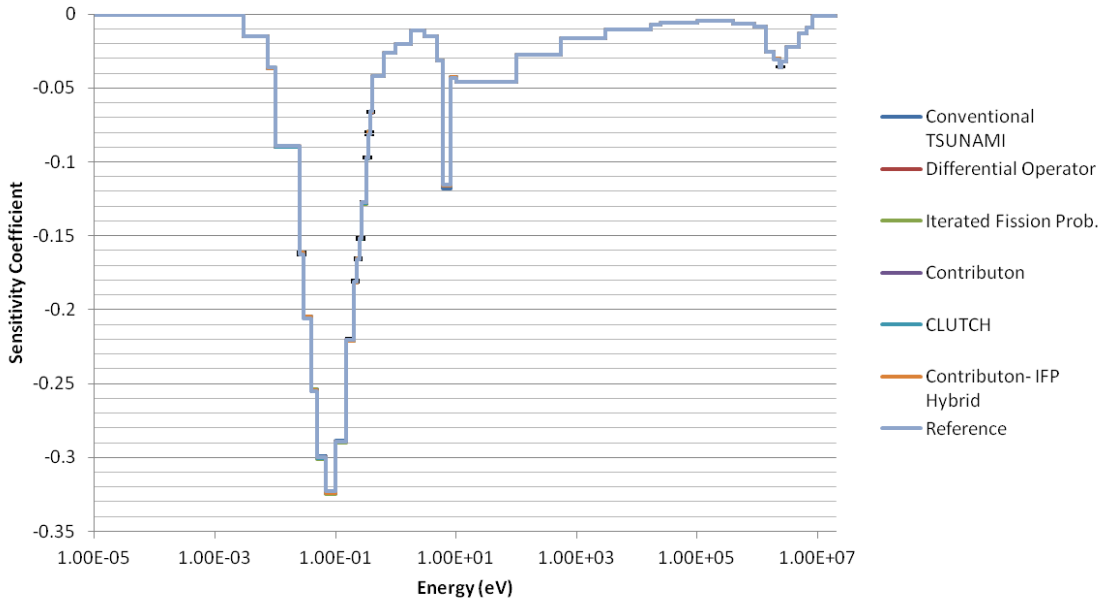

Figure 3.1: Fuel Pin fuel absorption sensitivity coefficients.

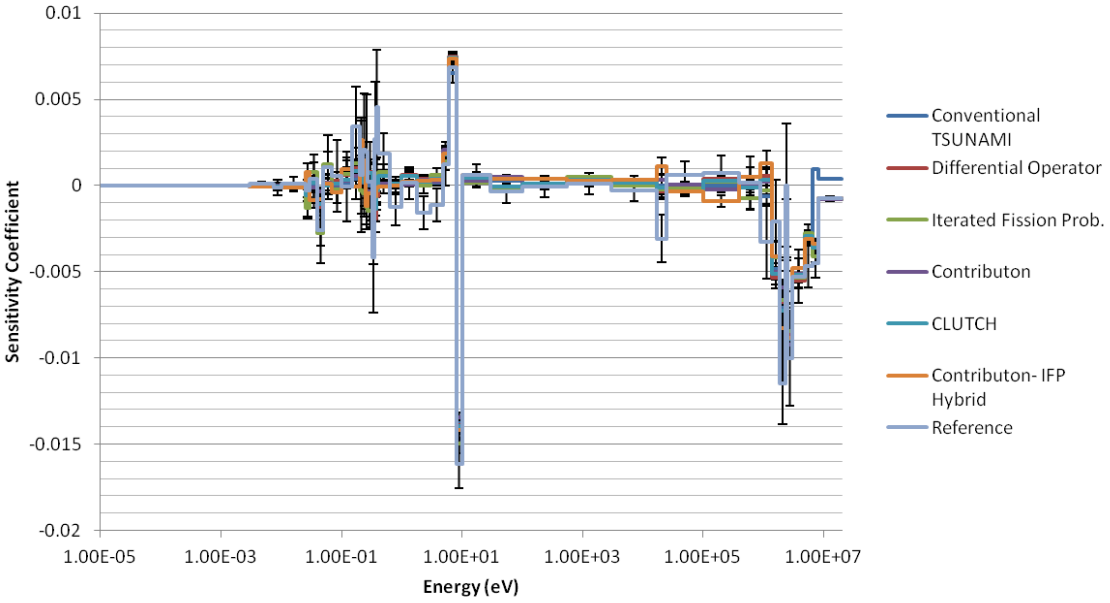

Figure 3.2: Fuel Pin fuel scatter sensitivity coefficients.

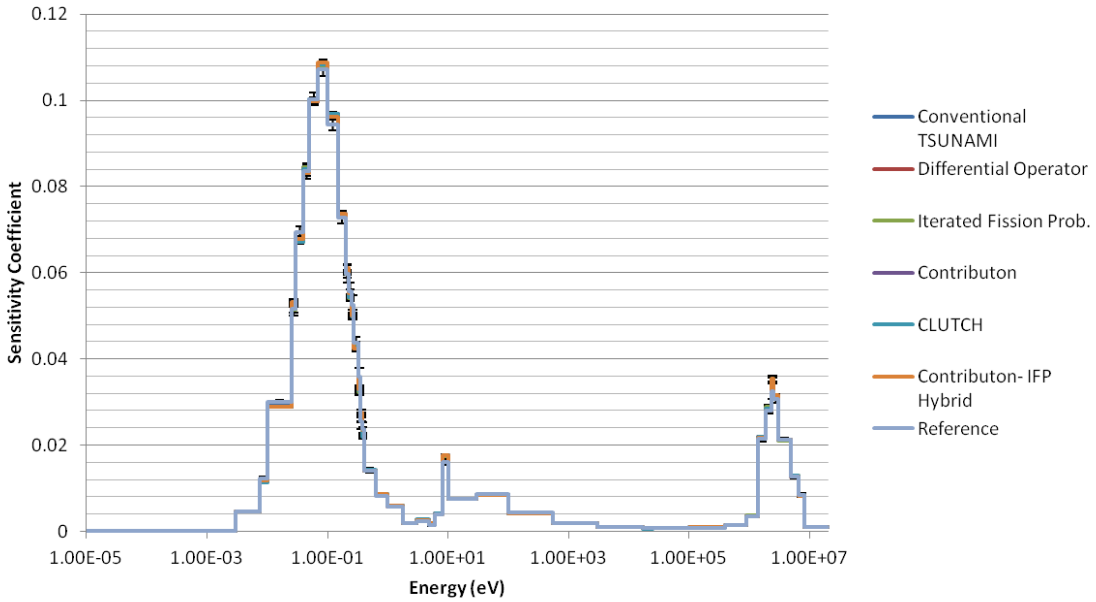

Figure 3.3: Fuel Pin fuel fission sensitivity coefficients.

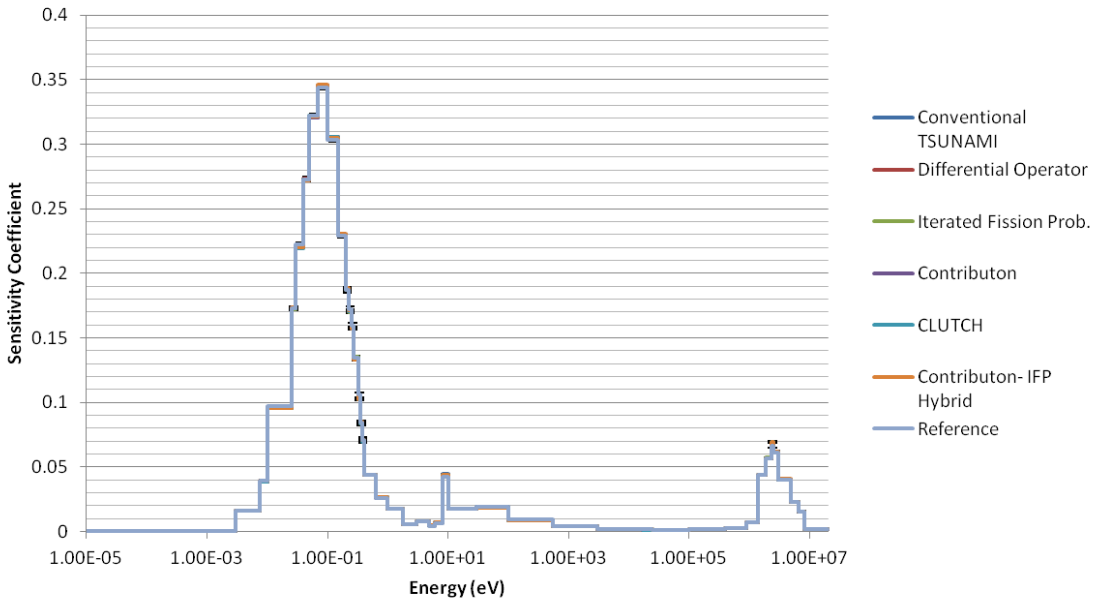

Figure 3.4: Fuel Pin fuel $\bar{\nu}$ sensitivity coefficients.

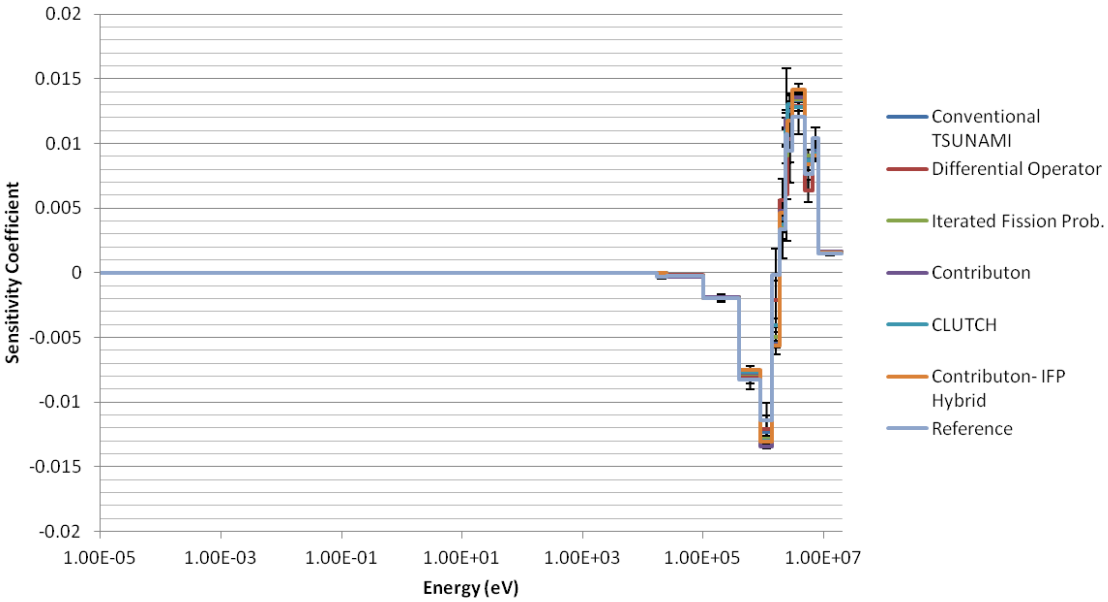

Figure 3.5: Fuel Pin fuel constrained chi sensitivity coefficients.

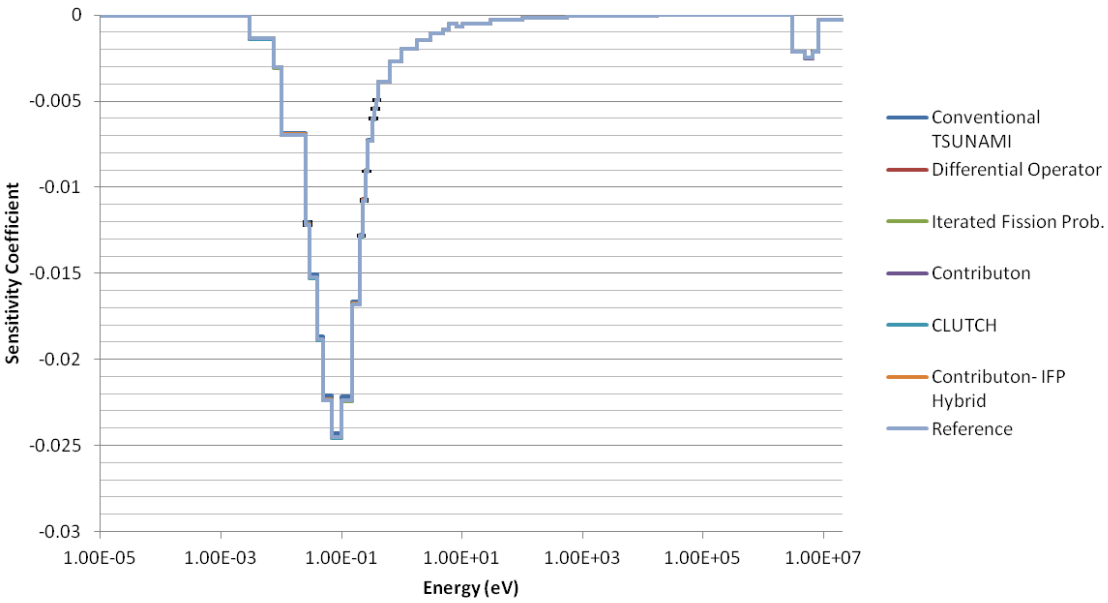

Figure 3.6: Fuel Pin moderator absorption sensitivity coefficients.

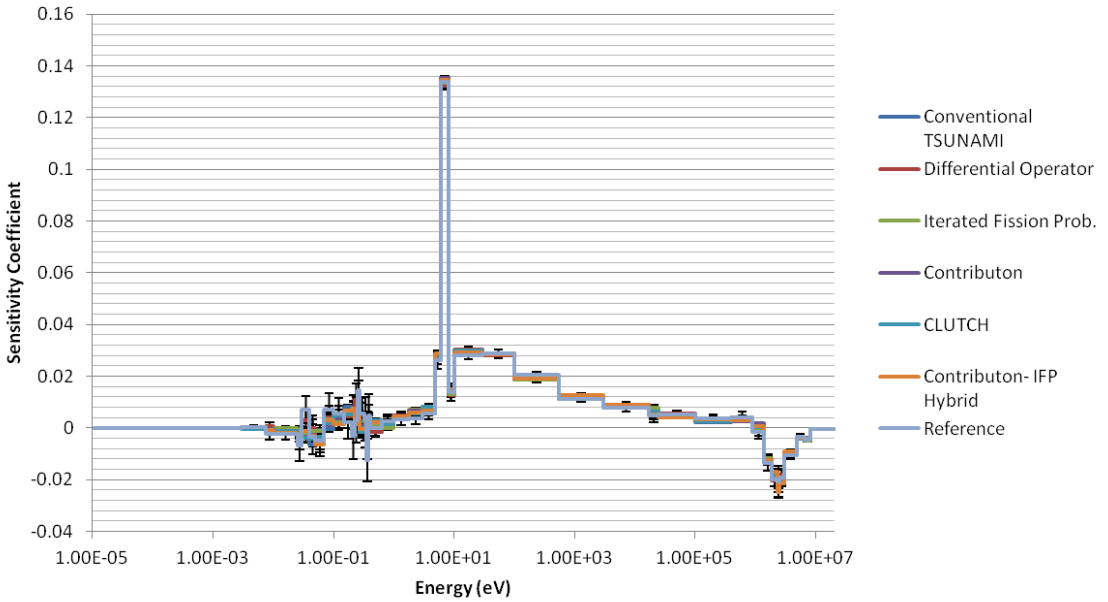

Figure 3.7: Fuel Pin moderator scatter sensitivity coefficients.

As seen in the figures, the fuel fission, absorption, and $\bar{\nu}$ sensitivities reach a maximum value in the thermal energy range. Although the moderator absorption cross section is more-or-less constant over all energies, the moderator absorption sensitivity coefficient varies greatly as a function of energy because moderator absorption at select energies removes neutrons that would otherwise enter the fuel and undergo important fission reactions. This is also true for the scattering sensitivity coefficients, which are large near energies containing important absorption resonances (such as the large U-238 absorption resonance at 6.67 eV) because scatter reactions at these energies allow neutrons to escape from the resonance energy range. The constrained chi sensitivity is negative for lower energies because neutrons born at these energies enter the resonance absorption energy range, and becomes positive around 1.85 MeV because neutrons at these energies experience a lower capture to fission ratio and can cause fissions in U-238.

The sensitivity coefficients shown in Figures 3.1 through 3.7 agree well for the different sensitivity methods, and disagreement between the methods is often imperceptible in the figures. More disagreement is seen in the scattering sensitivities, which have larger statistical uncertainties because they are calculated by taking the difference of two terms that are often very similar in magnitude. Tables 3.3 and 3.4 show

the results from the chi-squared comparison between the results of each of the sensitivity method with the IFP-20 and direct perturbation reference cases, respectively. The normalized (norm.) χ^2 term was obtained by dividing the χ^2 statistic for each method by the number of degrees of freedom in the sensitivity coefficient comparison. In general, data that exhibits good agreement with reference data has a normalized χ^2 value that is about equal to one.

Table 3.3: Comparison with the IFP-20 reference case for the Fuel Pin problem

	Conven. TSUNAMI	**Diff. Operator**	**IFP-2**	**Contrib.**	**CLUTCH**	**Contrib.- IFP Hybrid**
Norm. $\chi2$	1.6929	0.6239	0.7062	0.8358	0.7831	0.7929
p-value	0.0000	0.9999	0.9999	0.9790	0.9964	0.9948

Table 3.4: Comparison with the direct perturbation cases for the Fuel Pin Problem

	Conven. TSUNAMI	**Diff. Operator**	**IFP-2**	**Contrib.**	**CLUTCH**	**Contrib.- IFP Hybrid**
Norm. $\chi2$	1.2207	1.2581	1.2389	1.2404	1.2326	1.2193
p-value	0.1983	0.1670	0.1825	0.1813	0.1878	0.1997

The results presented in Tables 3.3 and 3.4 indicate that all of the Shift sensitivity coefficients methods produced accurate estimates for the sensitivity coefficients in the Fuel Pin model. In fact, the χ^2 values for many of the methods gave p-values close to 1.0, indicating better agreement than is expected. These high p-values could indicate that Shift is overestimating the uncertainty for the IFP-20 reference sensitivity coefficients, but are likely due to the simple nature of the Fuel Pin problem. Although very large p-values typically cause a chi-squared test to reject the null hypothesis, large p-values were not used as a basis for rejection in this study because many of the sensitivity methods calculate sensitivity coefficients without interrupting the random walks in a simulation, and large p-values simply indicate that the methods are producing very similar estimates for the importance of neutrons in the system. In this study, simulations that produced p-

values less than 0.10 were interpreted to show a statistically significant difference in sensitivity coefficients compared to reference simulations.

Although it lacks the capability to perform adjoint-weighted sensitivity tallies, the Differential Operator method agrees well with the reference sensitivity coefficients for the Fuel Pin case; such good agreement was not achieved by the Differential Operator method for the more-complex problems presented later in this chapter. The conventional TSUNAMI method shows significant disagreement with the IFP-20 reference, but this disagreement should be taken with a grain of salt because of the differences in the TSUNAMI-3D and Shift physics packages. TSUNAMI's physics package allows for some neutron interactions, such as *(n,2n)* reactions, which cannot currently occur in Shift, and two codes that are simulating a different set of physical phenomenon should not produce identical sensitivity coefficients. *(n,2n)* reactions are typically treated as part of the scattering sensitivity coefficient, and omitting the scattering sensitivity coefficients for energy groups greater than 1.0 MeV from the χ^2 comparison drops the conventional TSUNAMI's normalized χ^2 from 1.6929 to 1.2073, indicating that much of the difference seen between the TSUNAMI and Shift sensitivity methods is due to differences in the code physics packages.

The comparison between the sensitivity methods and the direct perturbation results was not as strong as the comparison with the IFP-20 results because of the much smaller number of usable sensitivity coefficients for this comparison. The much lower number of comparable sensitivities for the direct perturbation data indicates the difficulty involved in generating reliable, energy-dependent reference sensitivity coefficients with the direct perturbation method. In direct perturbation calculations, sensitivity coefficients must be large enough to cause a significant change in the eigenvalue, the eigenvalue uncertainties for each perturbation case must be small enough to show this impact, and eigenvalue must behave linearly around the perturbation to achieve accurate sensitivity coefficients. The uncertainty for the direct perturbation sensitivity coefficients was typically one to two orders of magnitude larger than that from the IFP-20 reference case, and the fact that each of the sensitivity methods produced nearly the same normalized χ^2 values indicates that much of this disagreement is due to uncertainty in the direct perturbation results.

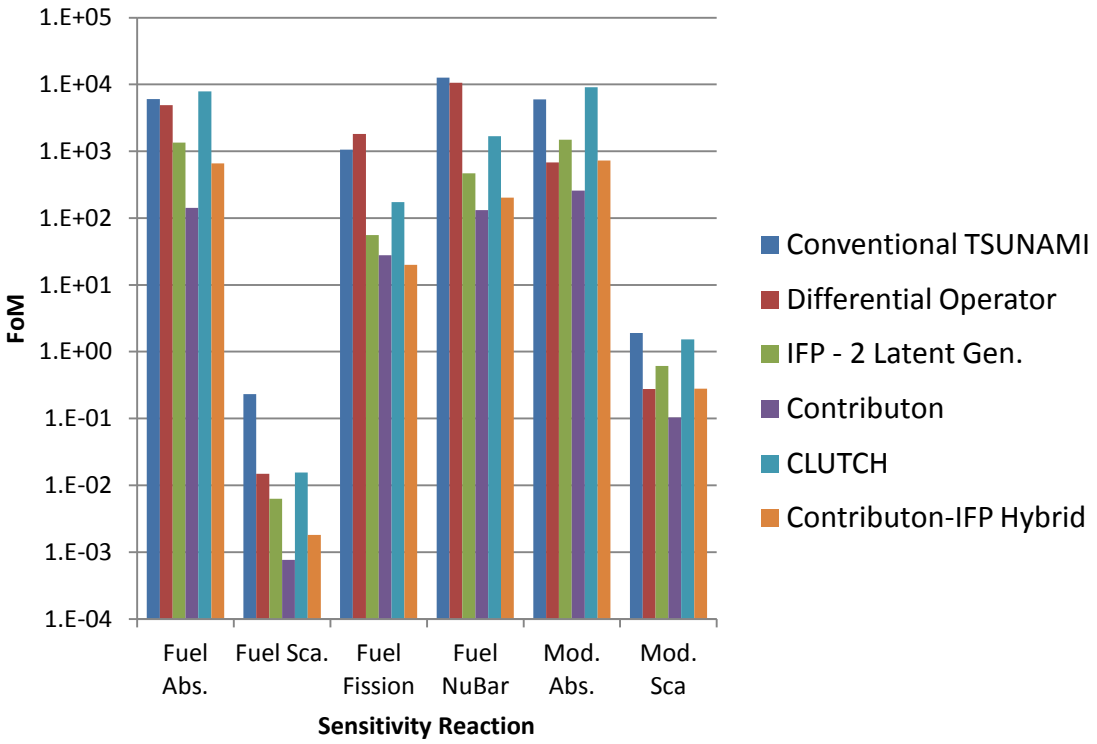

Figure 3.8: Figure of Merit comparison for the Fuel Pin sensitivity coefficients.

Figure 3.8 shows the FoM that were obtained for the sensitivity coefficients in the Fuel Pin model. All of the sensitivity coefficient calculations in this dissertation except for the conventional TSUNAMI calculation were simulated on the Orthanc cluster at ORNL, which contains uniform-speed computational nodes. The conventional TSUNAMI calculations were not simulated on the ORNL Orthanc cluster because they routinely required more memory than was available on the cluster, and were instead simulated on similar nodes on the ORNL CPILE2 cluster. Thus, comparing the conventional TSUNAMI FoM calculations with the results from the other methods does not provide a truly fair comparison, but was included in this study anyway to at least quantify the efficiency of the conventional TSUNAMI method. The conventional TSUNAMI, Differential Operator and CLUTCH methods produced the largest FoM, followed by the IFP method. These methods performed better than the IFP method because they guarantee non-zero sensitivity coefficient tallies for essentially every particle tracklength and collision, whereas the IFP method requires a complete fission

chain of progeny to determine the importance of an initial progenitor, and particles that leak from the system or are absorbed without causing a fission return importance estimates of zero. The Contributon and Contributon-IFP Hybrid methods produced the smallest FoM because of their need to simulate secondary particles to calculate sensitivity coefficients. The Contributon-IFP Hybrid method FoM were typically greater than the Contributon FoM because the Contributon-IFP Hybrid method simulates fission chains of particles after every fission event instead of simulating secondary particles after every collision. The Contributon-IFP Hybrid method may not always produce higher FoM than the Contributon method, especially for systems that require a higher number of latent generations for IFP calculations.

Table 3.5: Fuel Pin runtime comparison

	Conven. TSUNAMI	**Diff. Operator**	**IFP-2**	**Contrib.**	**CLUTCH**	**Contrib. -IFP Hybrid**
Runtime (minutes)	381.38	56.42	85.13	2353.07	54.95	254.63
Runtime Increase	774.3%	29.3%	95.2%	5294.2%	26.0%	483.7%

Table 3.5 gives the runtimes for each sensitivity coefficient calculation and the percentage increase in the runtime observed versus a case with no sensitivity coefficient calculations. Examining the runtimes reaffirms the trends observed by comparing the FoM for the different methods: the Differential Operator and CLUTCH methods performed the most efficient sensitivity coefficient calculations, followed by the IFP method, and then the two secondary-particle methods. Although the Contributon and Contributon-IFP Hybrid methods produced similar FoM, the Contributon runtime was much longer than the Contributon-IFP Hybrid method; this occurs because, although it simulates fewer secondary particles, the IFP methodology used by the Contributon-IFP Hybrid method is less efficient than that used by the Contributon method because any breaks in the IFP fission chains result in importance tallies of zero.

3.2 Godiva Results

The next problem used for evaluating the different sensitivity coefficient methods was a model of Godiva, an 8.741 cm sphere of highly-enriched uranium surrounded by vacuum [23]. Godiva was selected as a test problem to evaluate sensitivity coefficient calculations for a highly-enriched, high-leakage system. A $1/8^{th}$ model of Godiva was used for all sensitivity coefficient calculations to take advantage of the spatial X-, Y-, and Z-symmetry in the system. Figures 3.9 through 3.13 show the fuel absorption, scatter, fission, $\bar{\nu}$, and constrained chi sensitivity coefficients for the Godiva problem. Once again, one-sigma error bars were included in the figures, but are often not visible because the sensitivity coefficient uncertainties were very small for the problem.

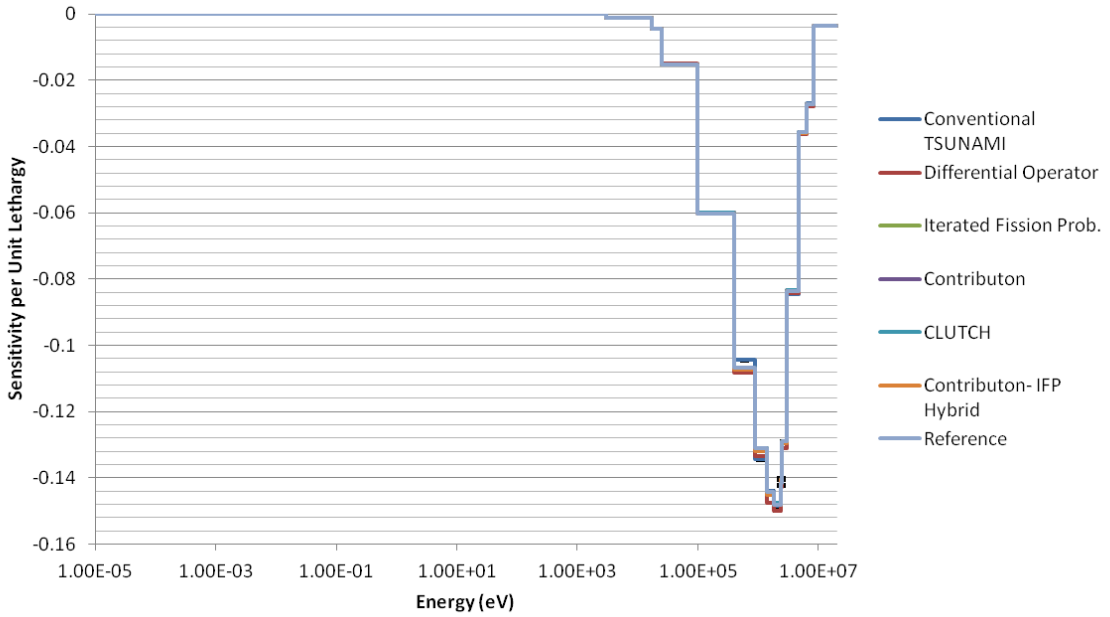

Figure 3.9: Godiva absorption sensitivity coefficients.

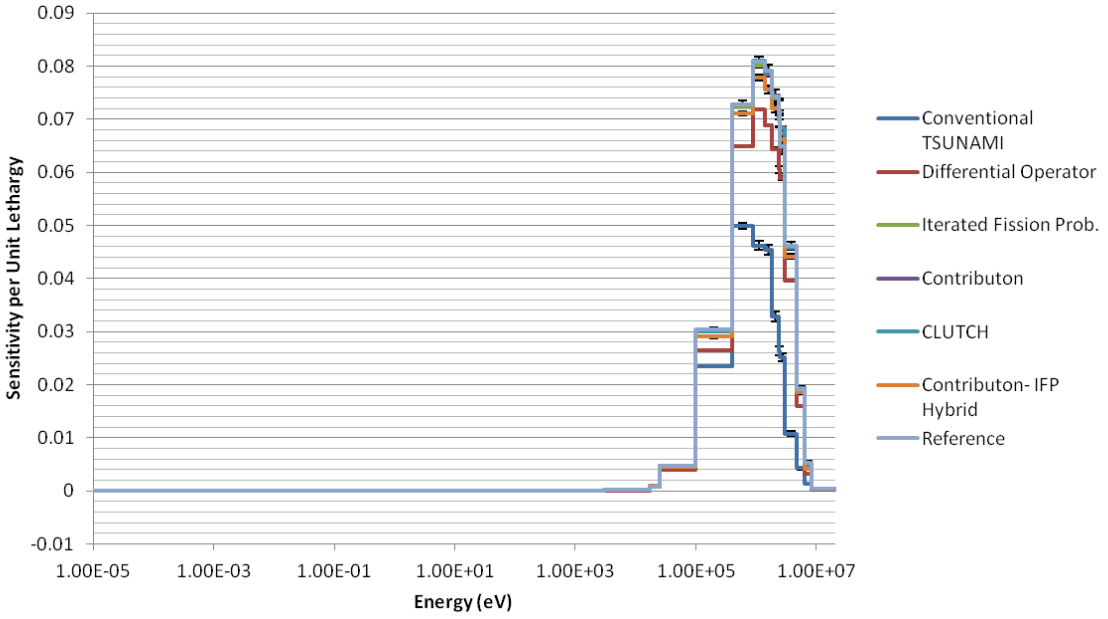

Figure 3.10: Godiva scatter sensitivity coefficients.

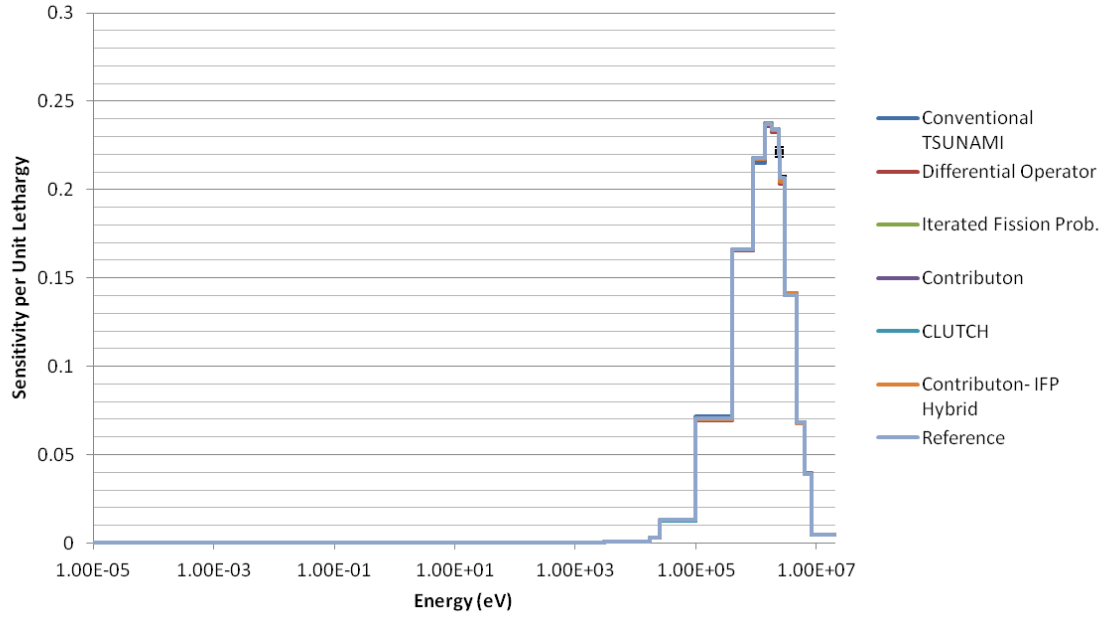

Figure 3.11: Godiva fission sensitivity coefficients.

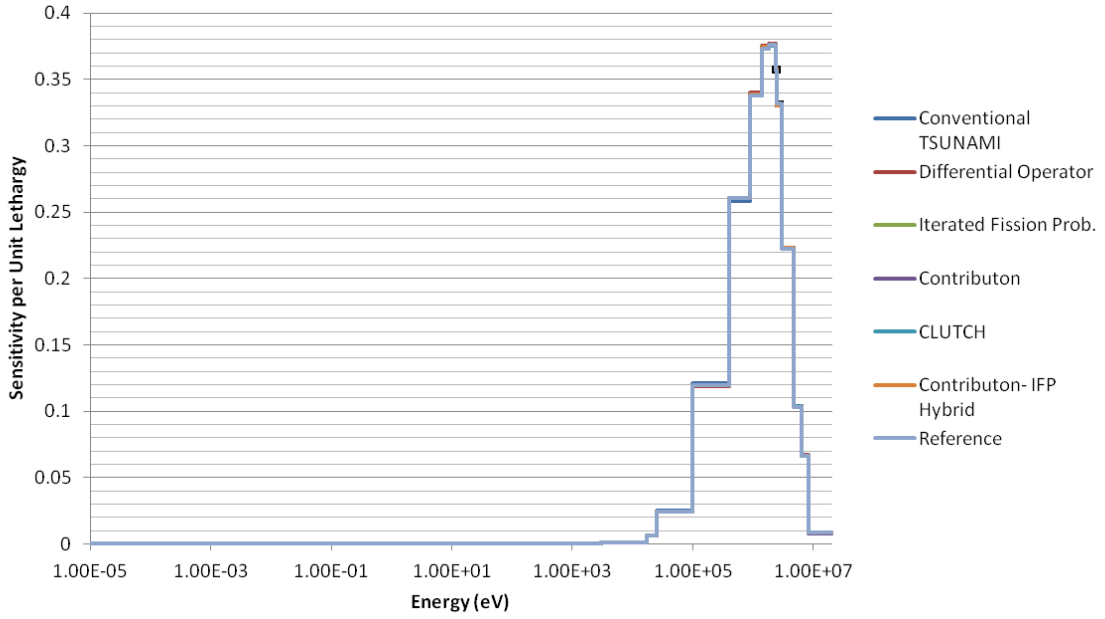

Figure 3.12: Godiva $\bar{\nu}$ sensitivity coefficients.

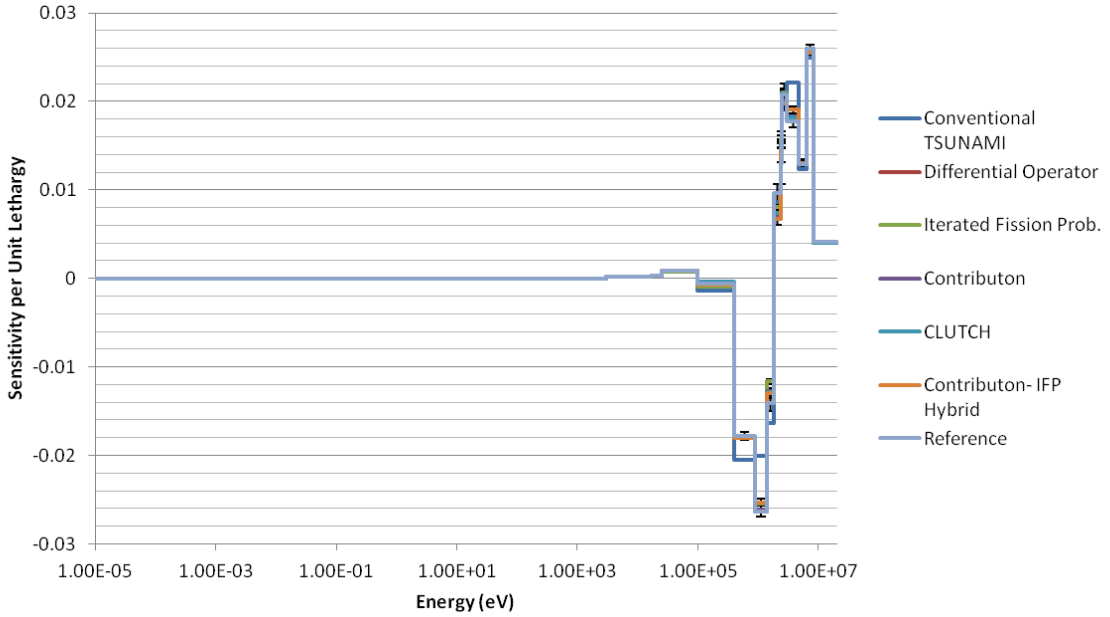

Figure 3.13: Godiva constrained chi sensitivity coefficients.

The fast nature of the neutron spectrum in Godiva is apparent when examining the sensitivity coefficients, few of which are nonzero for energies below 1 keV. The scattering sensitivities for Godiva are larger and more positive than were observed in the

Fuel Pin problem. Negative scattering sensitivity coefficients occurred in the Fuel Pin problem because these scattering reactions removed neutrons from the more important energy groups into groups with absorption resonances or higher capture-to-fission ratios. The scattering reaction sensitivities in Godiva are almost all positive because of the high amount of neutron leakage seen in the system and because scattering events prevent neutrons from leaking. The amplitude of the chi sensitivity coefficients is larger for the Godiva problem than the fuel pin because neutrons have a shorter lifetime in Godiva, and their birth energy has a greater impact on their contributon to the eigenvalue during their lifetime. The Godiva chi sensitivity coefficient is, as seen for the Fuel Pin problem, negative for lower energies but becomes positive for higher energies because the capture-to-fission ratio is lower at these high energies.

As shown in the figures, the different methods for calculating sensitivity coefficients agreed well for the Godiva problem. It is typically not possible to distinguish the sensitivity coefficients produced by the different methods in the figures, and usually only the Differential Operator and conventional TSUNAMI methods differ visibly from the other sensitivity coefficients. Indeed, these two methods are expected to produce differences in the sensitivity coefficients because the Differential Operator method does not use adjoint-weighted importance tallies, and the conventional TSUNAMI method is using a different physics package than Shift. Table 3.6 and 3.7 give the results of the chi-squared comparison between the sensitivity coefficients obtained using the different sensitivity coefficient methods and those from the IFP-20 and direct perturbation reference cases, respectively.

Table 3.6: Comparison with the IFP-20 reference case for the Godiva problem

	Conven. TSUNAMI	**Diff. Operator**	**IFP-2**	**Contrib.**	**CLUTCH**	**Contrib. -IFP Hybrid**
Norm. $\chi 2$	88.5729	14.8339	0.9814	0.9247	0.8968	1.5607
p-value	0	0	0.5242	0.6622	0.7258	0.0013

Table 3.7: Comparison with the direct perturbation cases for the Godiva problem

	Conven. TSUNAMI	**Diff. Operator**	**IFP-2**	**Contrib.**	**CLUTCH**	**Contrib. -IFP Hybrid**
Norm. $\chi 2$	8.0720	1.8640	1.4200	1.4313	1.4285	1.3743
p-value	0.0000	0.0007	0.0411	0.0377	0.0385	0.0577

Table 3.6 indicates that although most of the methods agreed well with the IFP-20 reference sensitivities, significant differences were observed for the sensitivity coefficients produced by the conventional TSUNAMI, Differential Operator, and Contributon-IFP Hybrid methods. The reason for the disagreement produced by the conventional TSUNAMI and Differential Operator methods has previously been discussed, but it is surprising that the Contributon-IFP Hybrid method produced sensitivity coefficients that did not show good agreement with the reference sensitivities. This disagreement could be caused by an underestimation of the uncertainty for the sensitivity coefficients produced by the Contributon-IFP Hybrid method. Although the Differential Operator and Contributon-IFP Hybrid methods failed the chi-squared test in Table 3.6, it should be noted that they generally agreed well with the reference sensitivity coefficients. With the exception of the scattering sensitivities, which had large statistical uncertainties, these methods typically gave sensitivity coefficients that differed from reference values by less than one percent; however, the chi-squared test does not examine the percent differences between sensitivity coefficients, but rather the difference in terms of the effective number of standard deviations, and thus these methods failed the chi-squared test. Although these methods fail the chi-squared test used to evaluate the

sensitivity coefficient methodologies here, methods that obtain sensitivity coefficients that are within one percent of reference sensitivities are typically considered successful in criticality safety calculations.

Although all of the sensitivity methods failed the chi-squared test in Table 3.7, it does not necessarily mean that the methods are producing inaccurate sensitivity coefficient estimates. As mentioned earlier, using direct perturbation calculations to calculate sensitivity coefficients is somewhat of an art, and the fact that several different methods produced similar normalized χ^2 statistics suggests that the direct perturbation sensitivity coefficients may not be accurate.

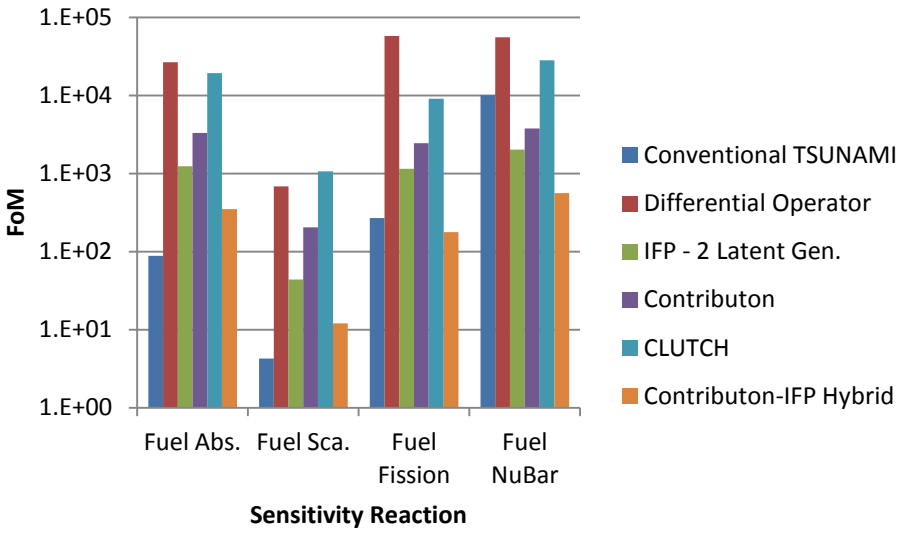

Figure 3.14: Figure of Merit comparison for the Godiva sensitivity coefficients.

Figure 3.14 shows the FoM that were produced for the different sensitivity reaction types using each sensitivity coefficient calculation method. As seen in the figure, the Differential Operator and CLUTCH methods once again gave the largest FoM, and were followed not by the IFP method, but by the Contributon method. The Contributon method, which produced small FoM for the Fuel Pin problem because of its need to simulate a large number of secondary particles, showed a large increase in efficiency for the Godiva model both because neutrons in Godiva see fewer collisions from birth until death, and also because the average lifetime, and thus simulation time, are much lower for neutrons in Godiva than in the infinitely-reflected fuel pin problem.

The much lower neutron simulation time for the Godiva problem allowed the Contributon method to produce larger FoM than the IFP and conventional TSUNAMI methods, which both saw large increases in problem runtime, as shown in Table 3.8, due to the large amount of data processing inherent to the methods. The superior performance exhibited by the Contributon method is not expected to continue when continuous-energy sensitivity calculations are performed. The runtime increase due to data processing seen for the IFP method, as well as for the Differential Operator and CLUTCH methods, should become less significant for continuous-energy simulations because of the large increase in runtime required for the time-consuming continuous-energy cross-section lookups; continuous-energy Contributon and Contributon-IFP Hybrid calculations should see a runtime increase that is similar to what was seen here because a relatively small portion of their runtime is used for data processing.

Table 3.8: Godiva runtime comparison

	Conven. TSUNAMI	**Diff. Operator**	**IFP-2**	**Contrib.**	**CLUTCH**	**Contrib. -IFP Hybrid**
Runtime (minutes)	110.24	18.28	118.40	208.33	21.65	134.46
Runtime Increase	696.3%	32.0%	755.2%	1404.8%	56.4%	871.3%

3.3 MIX-COMP-THERM-004-001 Results

The MCT problem was chosen next to evaluate the different sensitivity coefficient methods because obtaining accurate sensitivity coefficients for the MCT problem has historically been very difficult. The MCT problem, shown in Figure 3.15, describes a criticality safety benchmark where a shipping cask containing an irregular assembly of reprocessed fast reactor fuel is partially flooded by water. The MCT model used in this study was slightly simplified by the removal of several spacer grids and other assembly structure. The MCT problem is difficult to solve because of the complex isotopic composition of the fast reactor fuel, the thick water reflector region surrounding the fuel, and the requirement for a very fine flux mesh; the problem requires a

conventional TSUNAMI mesh that is less than 0.5 cm in width in the fuel region, which causes the TSUNAMI flux mesh to require nearly 64 GB in memory [17]. It should be noted that the $F^*(r)$ mesh required for calculating sensitivity coefficients for the MCT problem with the CLUTCH and Contributon methods is much more coarse than the mesh required by the conventional TSUNAMI flux mesh, as described in chapter 4.3. The flux mesh used for the conventional TSUNAMI sensitivity coefficient calculations in this study is identical to the mesh used in Reference 17.

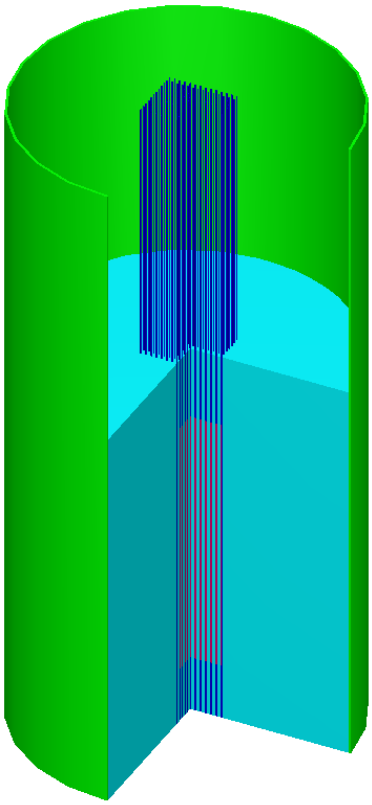

Figure 3.15: KENO-3D image of the MCT model; reprocessed fast reactor fuel (red) in a fuel assembly (dark blue) sits partially submerged in water (light blue) inside of a steel cask (green).

Figures 3.16 through 3.20 show the sensitivity coefficients that were calculated for the fuel absorption, scatter, fission, $\bar{\nu}$, and Constrained chi sensitivity coefficients, respectively, Figures 3.21 and 3.22 show the water moderator absorption and scatter sensitivity coefficients, respectively, and Figures 3.23 and 3.24 show the clad absorption and scatter sensitivity coefficients, respectively. All simulations for the MCT problem

used 1,400 active generations containing 5,000 neutron histories each except for the Contributon method simulation; the Contributon simulation instead used 350 active generations because of its extremely long runtimes (a factor of approximately 600 increase) for the MCT problem.

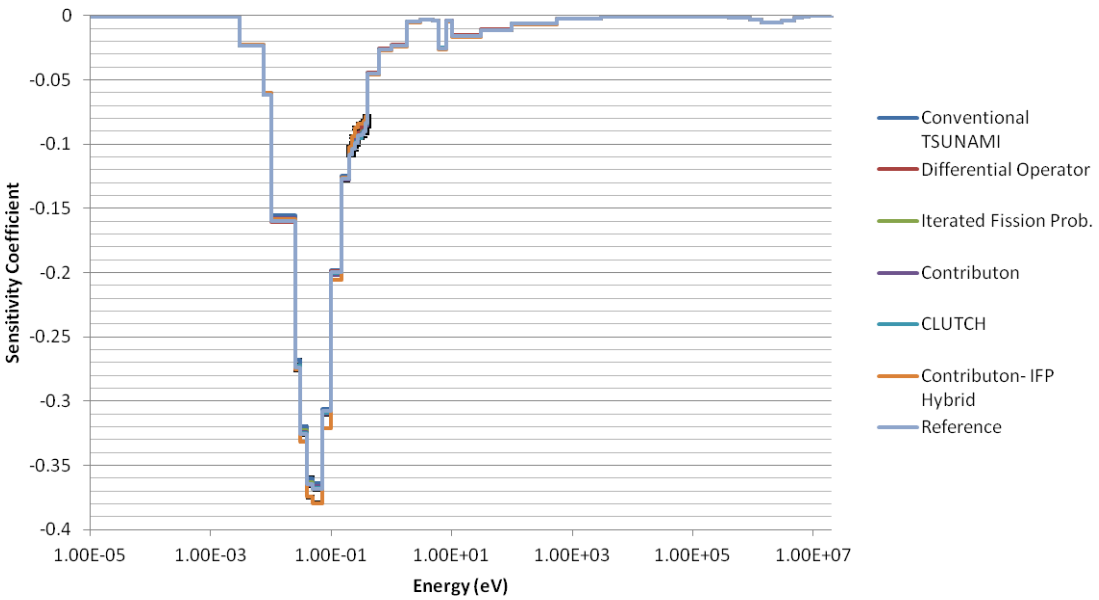

Figure 3.16: MCT fuel absorption sensitivity coefficients.

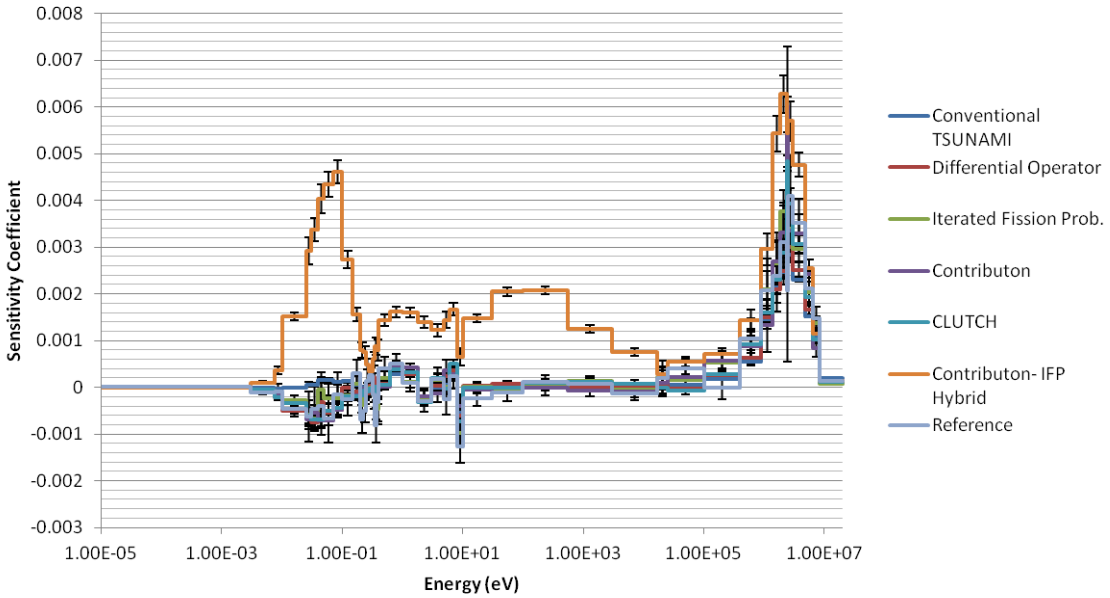

Figure 3.17: MCT fuel scatter sensitivity coefficients.

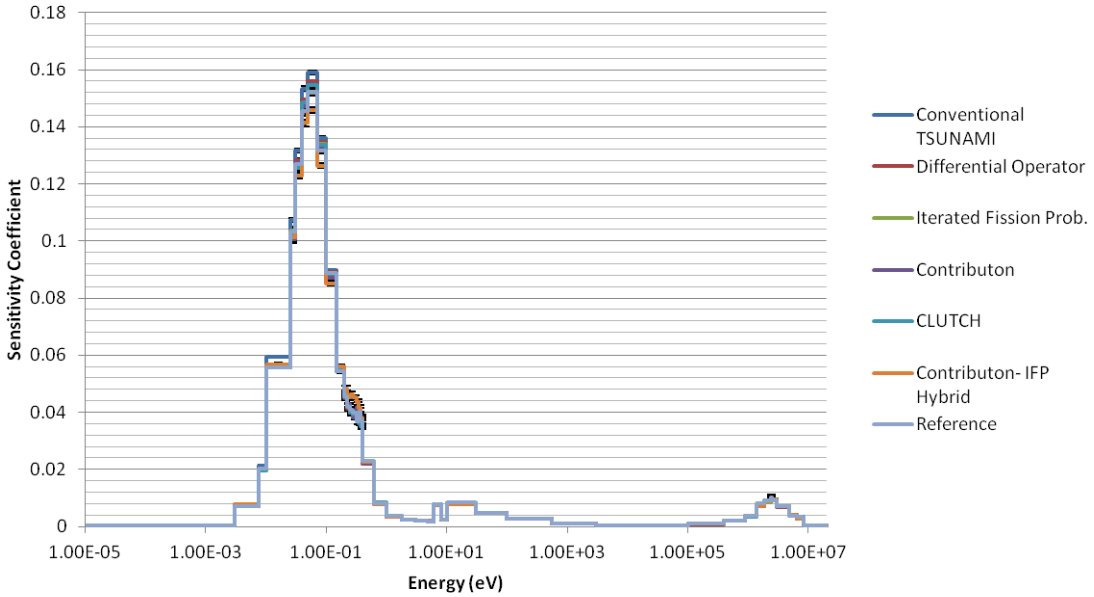

Figure 3.18: MCT fuel fission sensitivity coefficients.

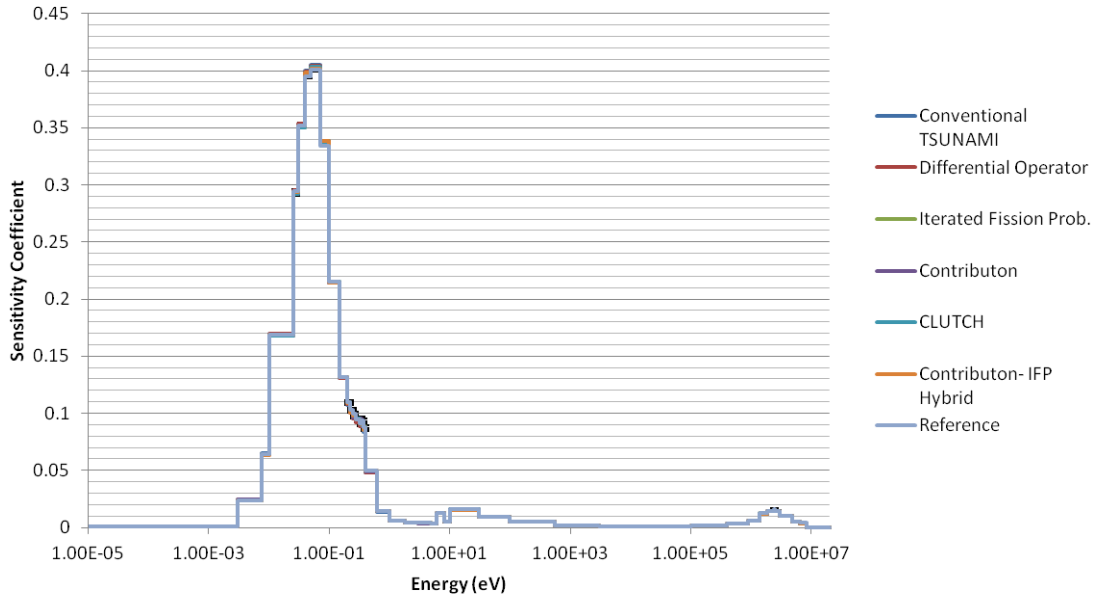

Figure 3.19: MCT fuel $\bar{\nu}$ sensitivity coefficients.

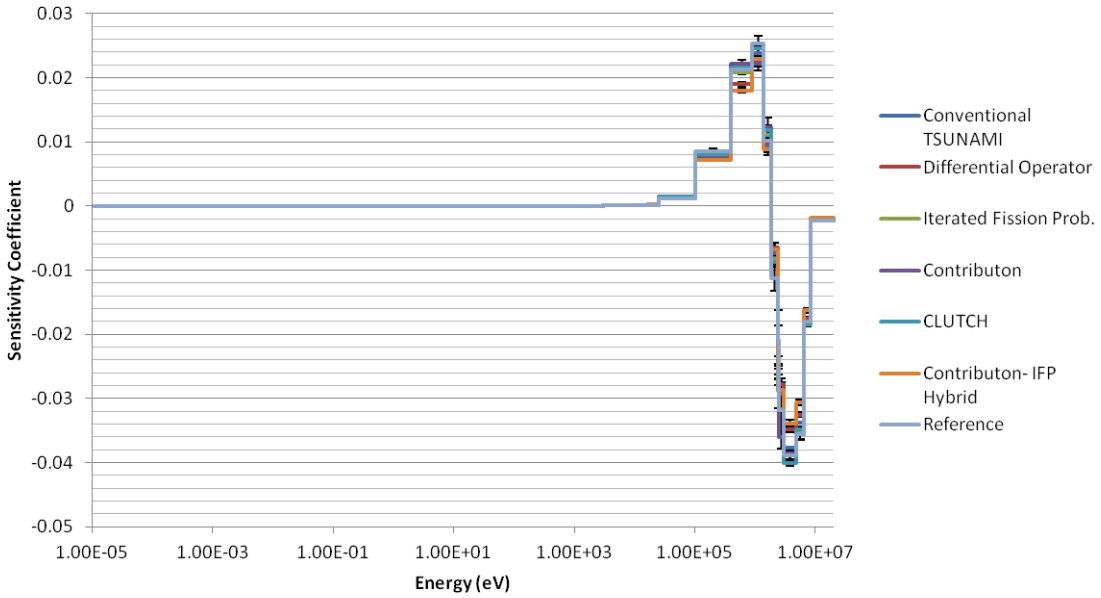

Figure 3.20: MCT fuel constrained chi sensitivity coefficients.

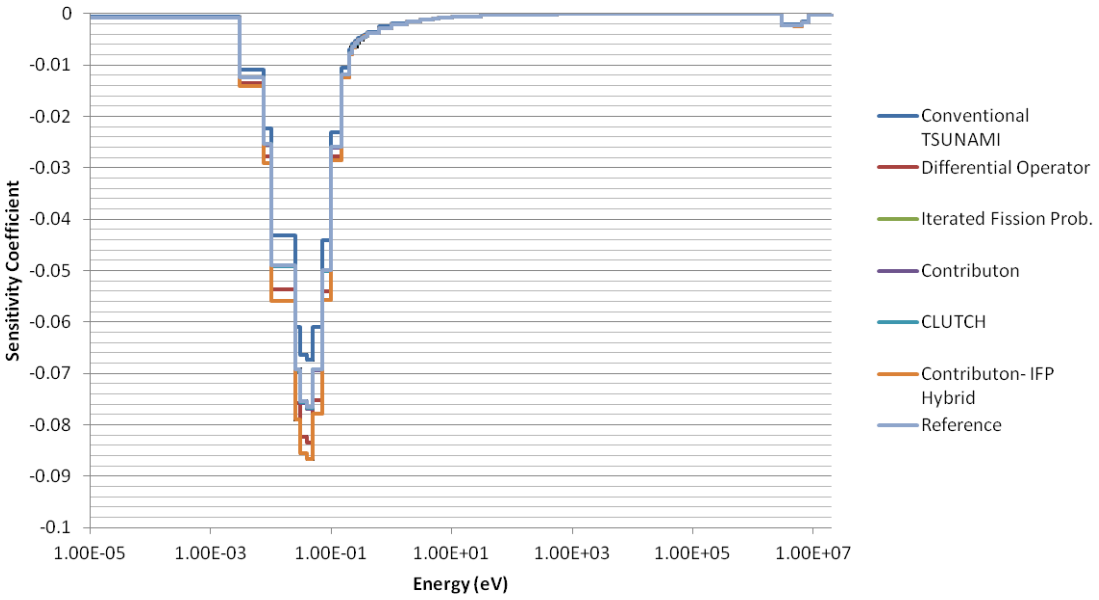

Figure 3.21: MCT moderator absorption sensitivity coefficients.

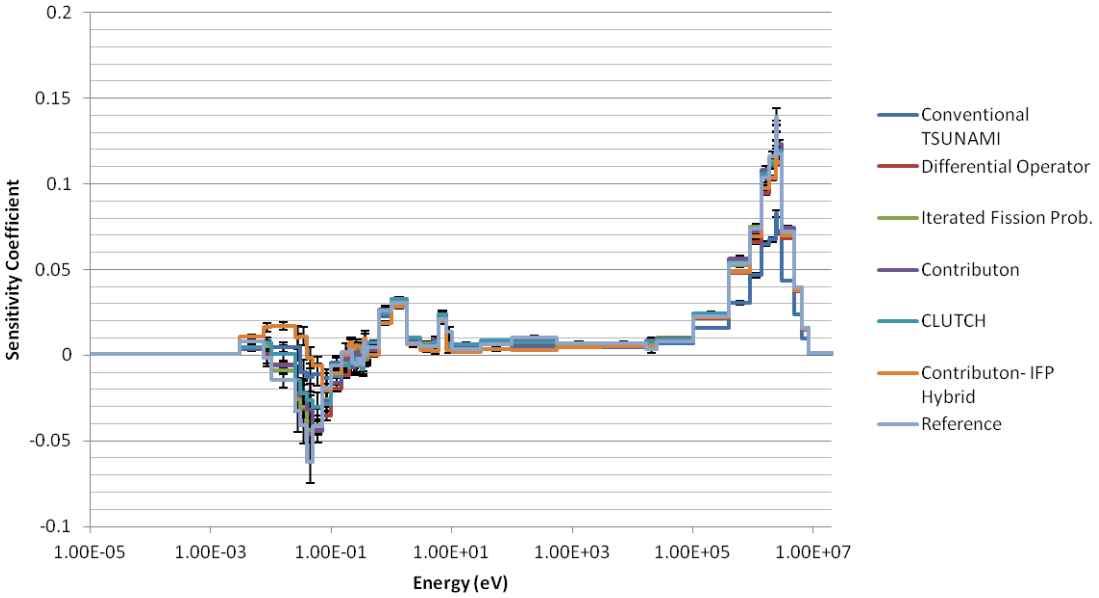

Figure 3.22: MCT moderator scatter sensitivity coefficients.

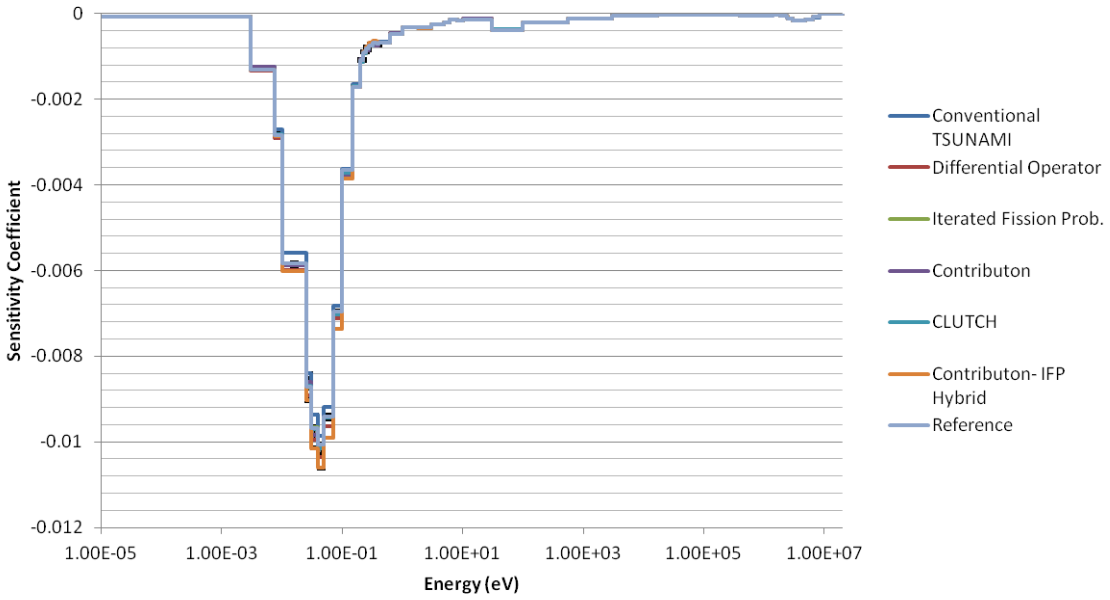

Figure 3.23: MCT clad absorption sensitivity coefficients.

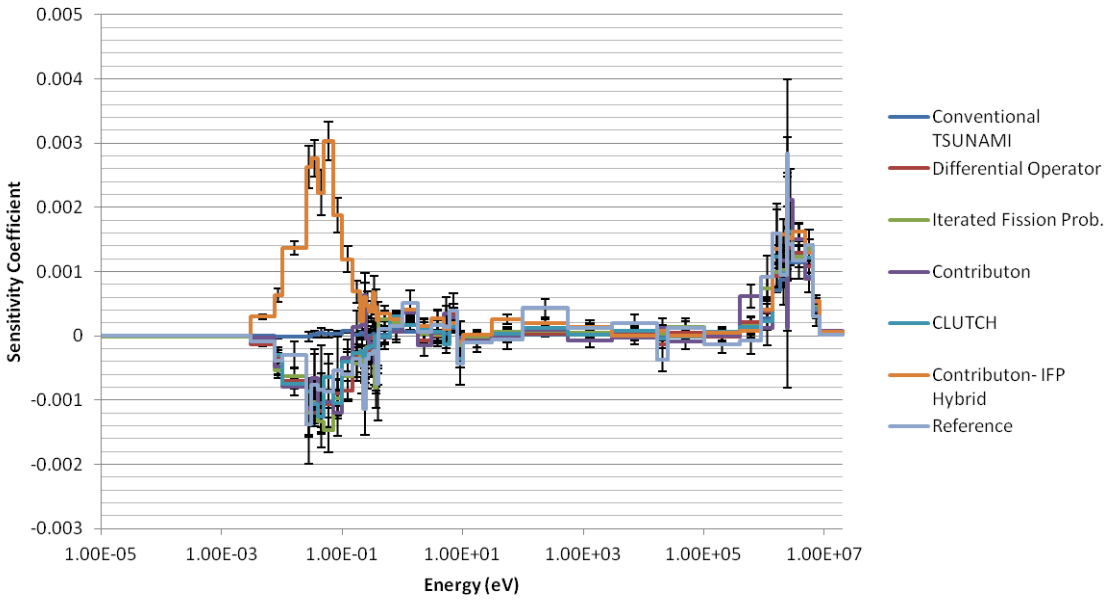

Figure 3.24: MCT clad scatter sensitivity coefficients.

As shown in Figures 3.16 through 3.24, the sensitivity coefficients once again somewhat followed the cross-section plots for the fuel in the problem, and the effect of the plutonium in the MCT fuel is clearly indicated by the large sensitivity coefficients

present near the thermal and near-thermal plutonium cross-section resonance energies. Unlike in the Fuel Pin and Godiva problems, the fission spectrum sensitivities for the MCT problem were positive at lower energies and became negative at higher energies. This phenomenon occurs because neutrons born at faster energies are more likely to leak from the system, whereas neutrons born at lower energies are more likely to collide in the moderator region and reach the important thermal energy groups. This hypothesis is further supported by the fact that the scattering sensitivities were at their maximum for the fast energy groups, indicating the large effect of leakage in the system. As expected, the clad sensitivity coefficients were generally much smaller than the fuel and moderator sensitivity coefficients.

The methods all produced sensitivity coefficients that generally agreed well, but the conventional TSUNAMI, Differential Operator, and Contributon-IFP Hybrid methods produced noticeable disagreement for some of the sensitivity coefficients. The Contributon-IFP Hybrid method's sensitivity coefficients showed especially poor agreement for the scattering sensitivities; however, the scattering sensitivities where this poor agreement was observed were typically small, and it is notoriously difficult to calculate small sensitivity coefficients that are calculated by taking the difference of two similar terms. The Differential Operator method performed better than expected for this difficult problem, and the IFP-5, Contributon, CLUTCH, and reference sensitivity coefficients are once again indistinguishable from the reference sensitivity coefficients in the figures.

Tables 3.9 and 3.10 show the results of the chi-squared tests comparing the sensitivity coefficient methods with the IFP-20 and direct perturbation reference sensitivity coefficients, respectively. As shown in Table 3.9, the IFP-5, Contributon, and CLUTCH methods performed well when compared with the IFP-20 sensitivity coefficients, and the conventional TSUNAMI, Differential Operator, and Contributon-IFP Hybrid methods gave sensitivity coefficients that were significantly different from the reference sensitivities. The Contributon and CLUTCH methods produced p-values that were smaller than the IFP-5 p-values because the $F^*(r)$ mesh refinement used for these cases was selected to maximize the performance of the methods while still producing a p-value indicative of no statistically significant difference. It is somewhat

surprising that the Differential Operator method produced such a large normalized χ^2 statistic because the method's sensitivity coefficients in Figures 3.16 through 3.24 generally look to agree well with the reference sensitivities.

Table 3.9: Comparison with the IFP-20 reference case for the MCT problem

	Conven. TSUNAMI	**Diff. Operator**	**IFP-5**	**Contrib.**	**CLUTCH**	**Contrib. -IFP Hybrid**
Norm. $\chi 2$	85.5237	29.5003	0.6534	1.0803	1.0716	57.8276
p-value	0.0000	0.0000	0.9999	0.1437	0.1701	0.0000

Table 3.10: Comparison with the direct perturbation cases for the MCT problem

	Conven. TSUNAMI	**Diff. Operator**	**IFP-5**	**Contrib.**	**CLUTCH**	**Contrib. -IFP Hybrid**
Norm. $\chi 2$	1.6069	1.6513	1.6025	1.5844	1.5931	1.5844
P-value	0.0582	0.0484	0.0593	0.0639	0.0615	0.0639

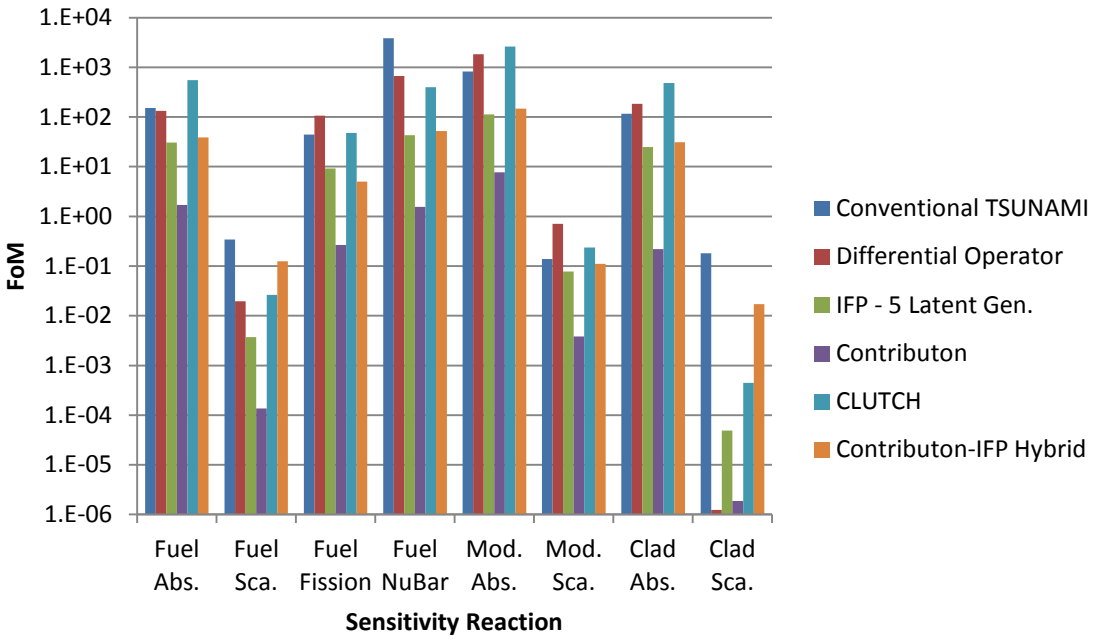

Figure 3.25: Figure of Merit comparison for the MCT sensitivity coefficients.

The FoM for the sensitivity coefficients produced by each sensitivity coefficient method are given in Figure 3.25. Although the Contributon simulation used a different number of active generations than the other methods, a FoM comparison is still applicable. In general, the FoM for quantities are constant regardless of the number of active histories used if the variance estimates for the tallies in question are well converged. As observed for the previous cases, the conventional TSUNAMI, Differential Operator, and CLUTCH methods gave the largest FoM, followed by the IFP-5 method, which produced FoM that were about an order of magnitude smaller. The FoM for the Contributon method were especially low due to the large water region surrounding the fuel assembly in the problem; neutrons leaking from the fuel region experienced a large number of collisions in the moderator region, causing the Contributon method to simulate many secondary particles, considerably increasing the problem runtime. This large runtime increase and FoM reduction was not seen for the Contributon-IFP Hybrid method, which simulates secondary particles after every fission event instead of after every collision. Although the Contributon-IFP Hybrid method produced FoM that were larger than the IFP FoM for many sensitivity coefficients, this method's superior performance is not likely to occur for continuous-energy calculations. Similar to the way

the Contributon method produced larger FoM than the IFP method for the Godiva problem, the MCT Contributon-IFP Hybrid simulation was able to outperform the IFP-5 simulation because a large amount of the IFP-5 simulation's runtime was spent processing the large amount of data used by the method. As shown in Table 3.11, the runtimes for the IFP-5 and the Contributon-IFP Hybrid calculations were very similar for the MCT problem. As these methods are extended to continuous-energy problems, the time consumed by data processing for the IFP method should become insignificant when compared to the amount of time required for cross-section lookups, and the efficiency advantage seen here for the Contributon-IFP method will likely be lost. The runtime increase for the Contributon method is not given in Table 3.11 because the Contributon simulation used a different number of active generations than the other simulations.

Table 3.11: MCT runtime comparison

	Conven. TSUNAMI	**Diff. Operator**	**IFP-5**	**Contrib.**	**CLUTCH**	**Contrib. -IFP Hybrid**
Runtime (minutes)	207.24	118.46	525.23	6955.07	122.04	603.11
Runtime Increase	191.8%	66.8%	639.4%	9691.7%	---	749.1%

3.4 PU-SOL-THERM-014 Case 30 Results

As shown in Figure 3.26, the PST problem describes a rectangular arrangement of four stainless-steel cylinders containing a Plutonium-Nitrate solution inside of a large concrete room. The PST problem is difficult to solve using the conventional TSUNAMI method because the large size of the concrete room containing the fuel cylinders requires a large number of spatial meshes; furthermore, it will be shown in chapter 4.3 that the large size of the regions containing the Pu-Nitrate solution adds to the difficulty of calculating $F^*(r)$ using the Contributon-based methods. All of the sensitivity coefficient methods calculated sensitivity coefficients for the PST problem over 1,800 active generations each containing 5,000 neutron histories.

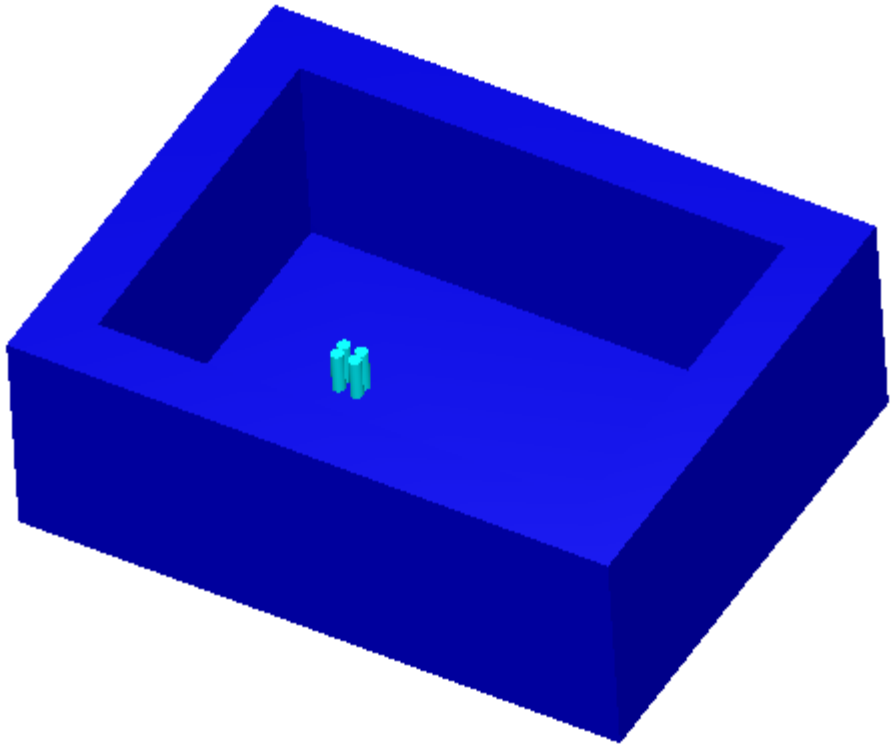

Figure 3.26: KENO-3D image of the PST problem; 4 steel cylinders partially filled with a Plutonium-Nitrate solution are arranged in a rectangle inside of a large, concrete room.

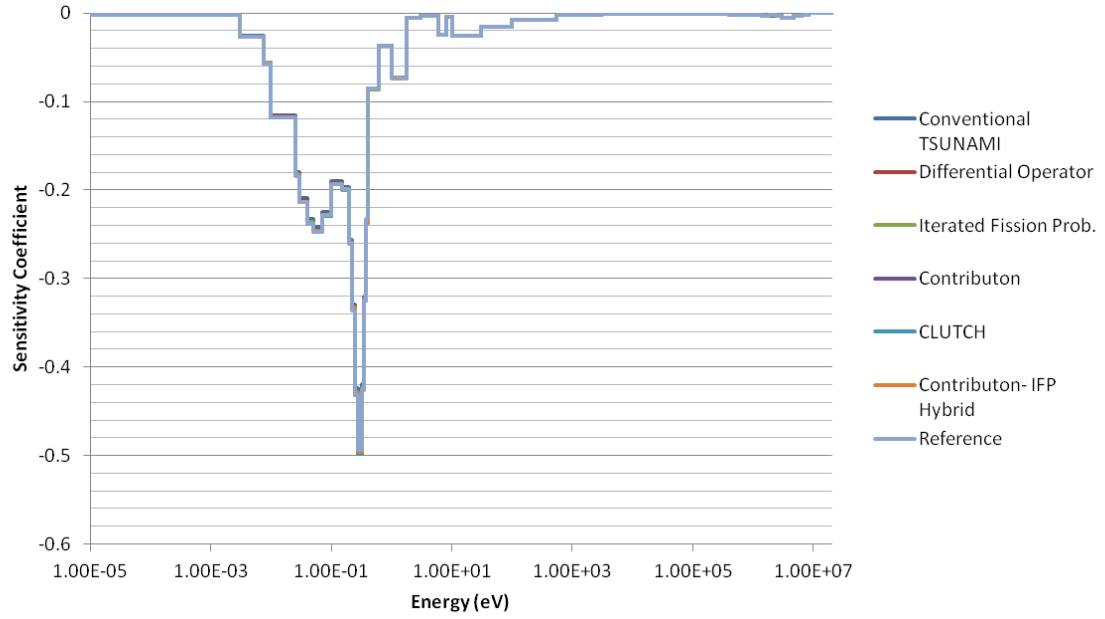

Figure 3.27: PST fuel absorption sensitivity coefficients.

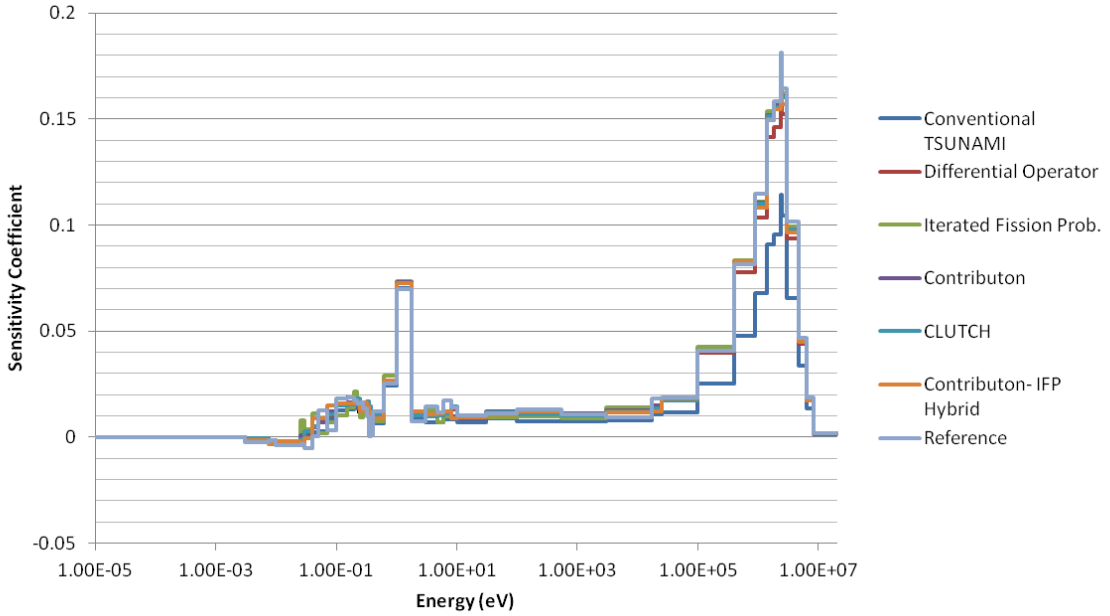

Figure 3.28: PST fuel scatter sensitivity coefficients.

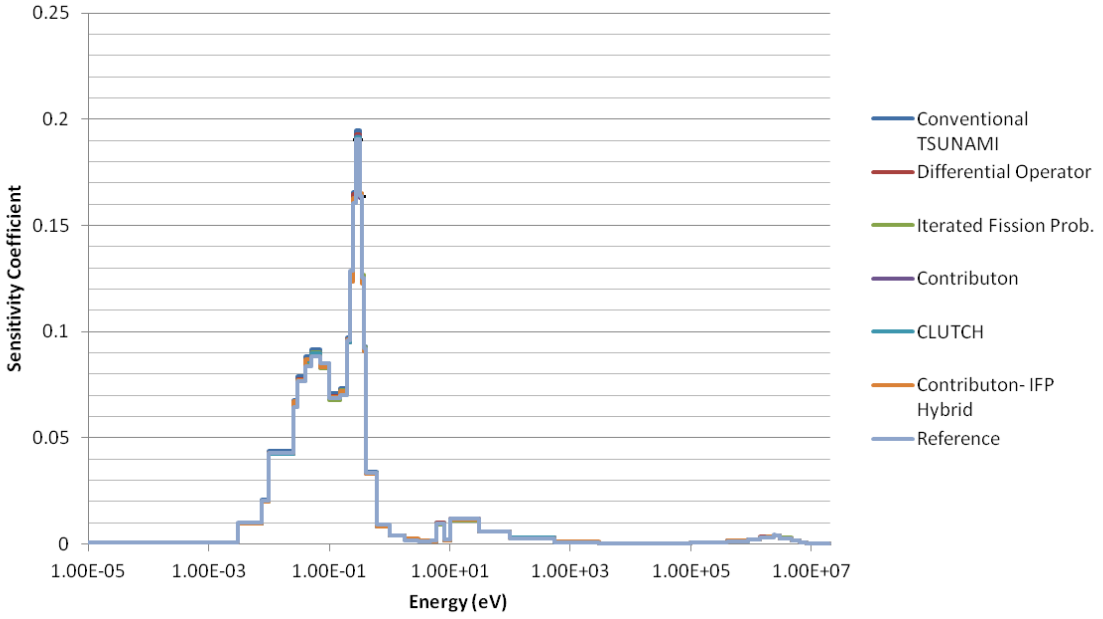

Figure 3.29: PST fuel fission sensitivity coefficients.

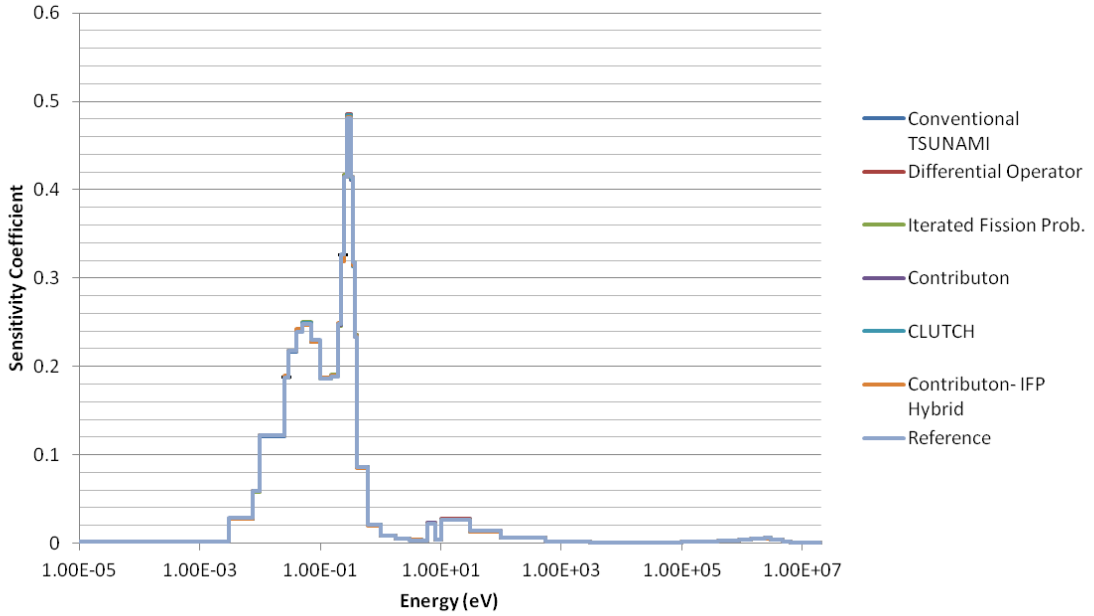

Figure 3.30: PST fuel $\bar{\nu}$ sensitivity coefficients.

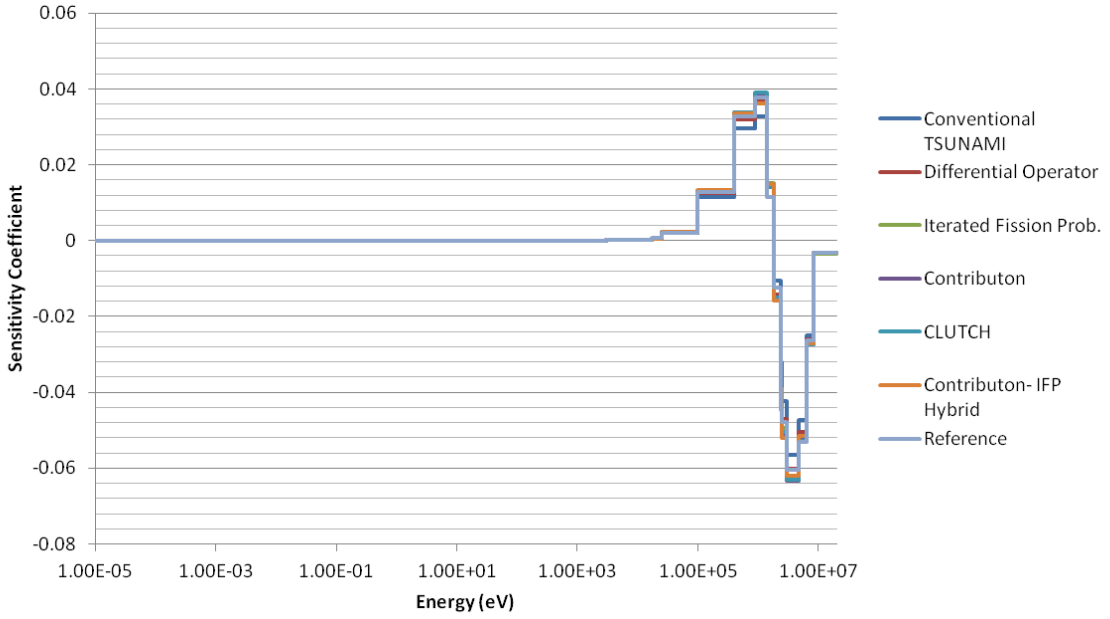

Figure 3.31: PST fuel constrained chi sensitivity coefficients.

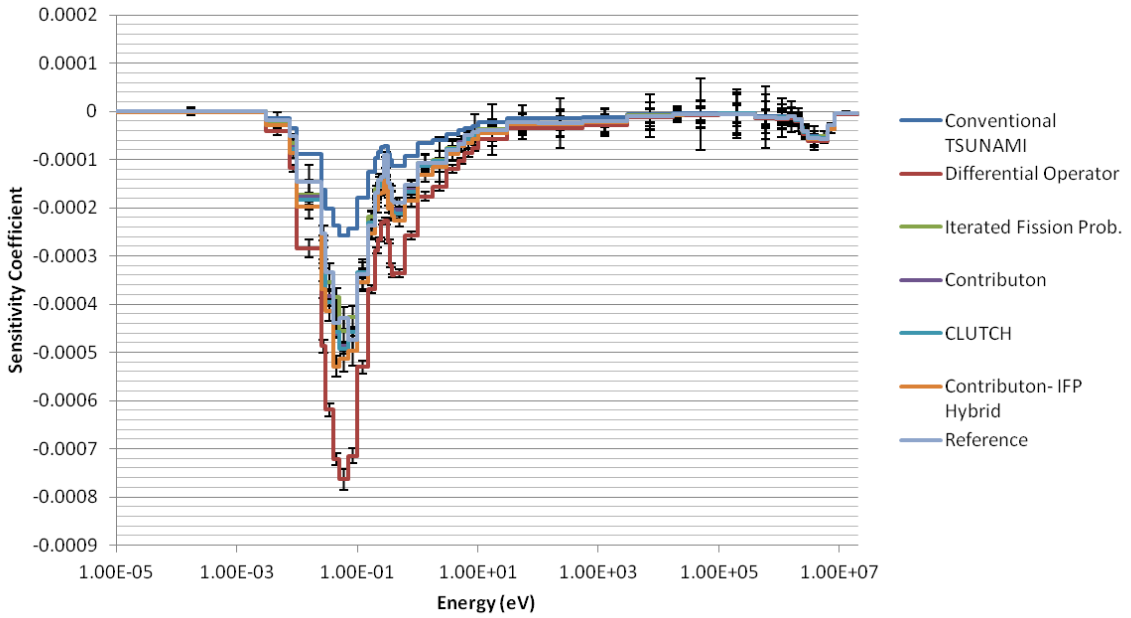

Figure 3.32: PST steel absorption sensitivity coefficients.

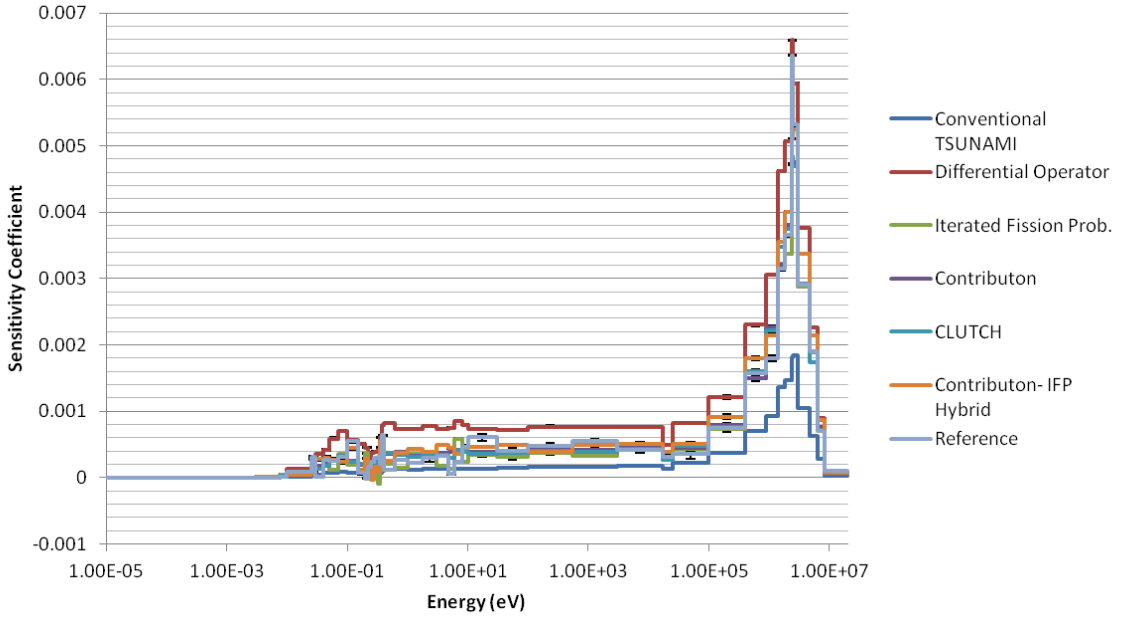

Figure 3.33: PST steel scatter sensitivity coefficients.

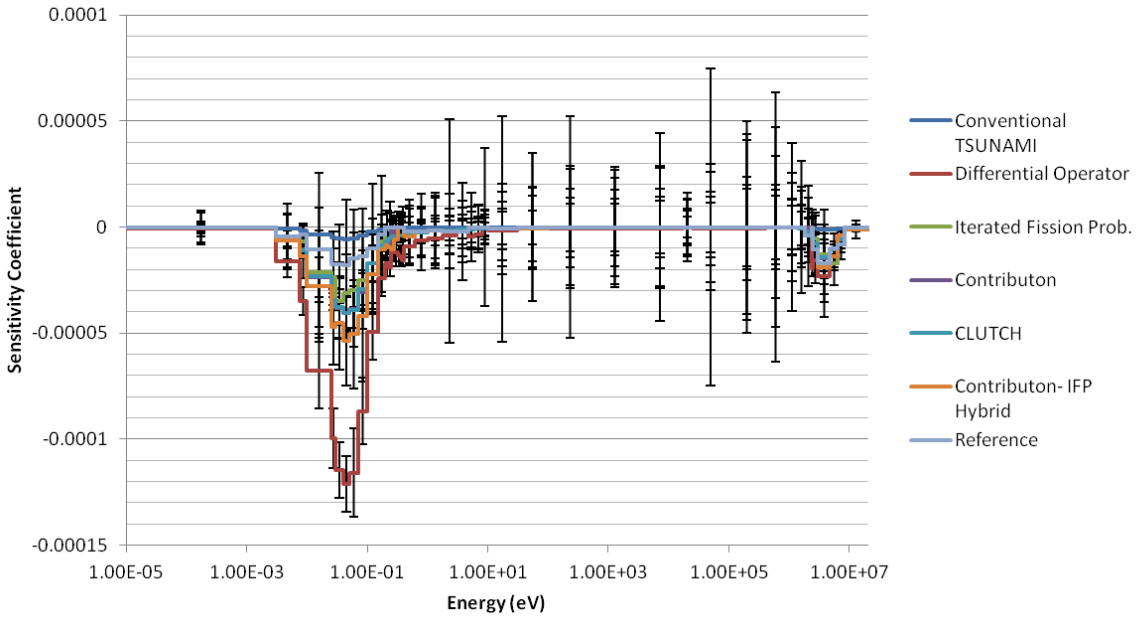

Figure 3.34: PST concrete absorption sensitivity coefficients.

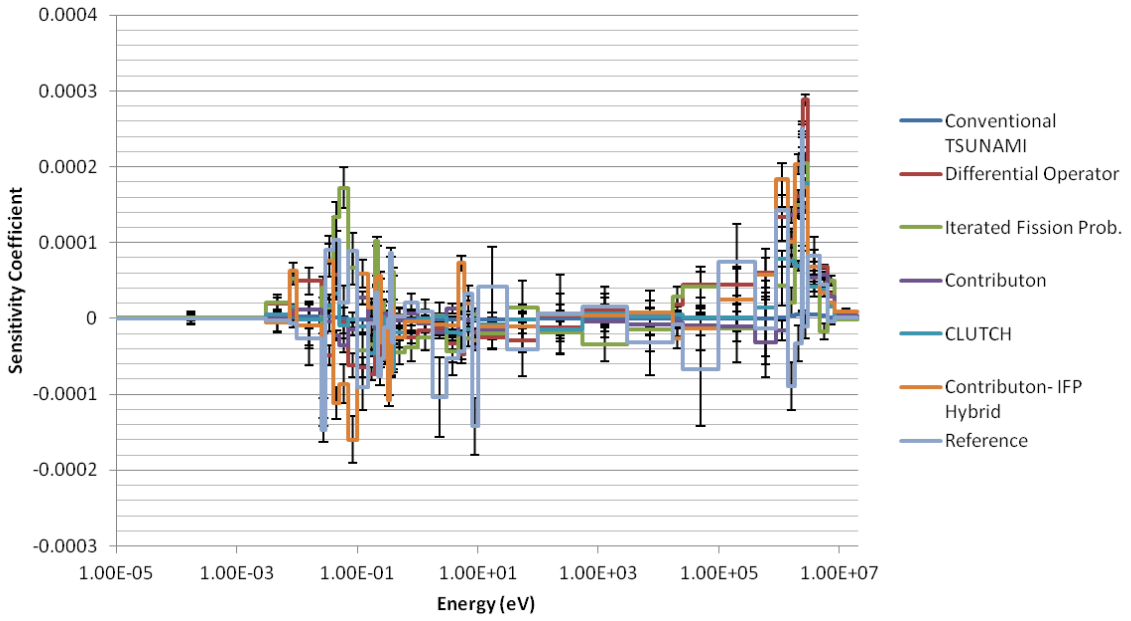

Figure 3.35: PST concrete scatter sensitivity coefficients.

Figures 3.27 through 3.31 give the fuel absorption, scatter, fission, $\bar{\nu}$, and constrained chi sensitivity coefficients, respectively, for the Plutonium-Nitrate fuel solution, Figures 3.32 and 3.33 give the absorption and scatter sensitivity coefficients, respectively, for the steel containers, and Figures 3.34 and 3.35 give the absorption and scatter sensitivity coefficients, respectively, for the concrete walls of the room. The sensitivity coefficients in Figures 3.27 through 3.35 behave similarly to the sensitivity coefficients that were calculated for the MCT problem, and the fuel absorption, fission, and $\bar{\nu}$ sensitivity coefficients reach their largest values for the thermal energies containing plutonium capture and fission resonances. The scattering sensitivities are generally positive, reaching their maximum values at fast energies because scattering events at these energies prevent fast neutrons from leaking out of the system. The fuel scattering sensitivity coefficient sees a sharp peak near 1.0 eV because scattering events at this energy allow neutrons to escape the large, Pu-240 absorption resonance at this same energy. As seen for the MCT problem, the PST constrained-chi sensitivity coefficients are positive at lower energies and negative for higher energies because faster neutrons have a higher probability of leaking from the system.

While all of the sensitivity coefficient methods agreed well for the fuel absorption, fission, $\bar{\nu}$, and constrained-chi sensitivity coefficients, the conventional TSUNAMI method produced poor sensitivity coefficient estimates for the fuel scatter, steel, and concrete sensitivities, and the Differential Operator and Contributon-IFP Hybrid methods showed poor agreement for the steel and concrete sensitivity coefficients. Because the steel and concrete sensitivity coefficients were generally very small, the disagreement seen for their values should not significantly affect the calculation for the total amount of uncertainty in the eigenvalue for the PST problem. The IFP-5, Contributon, and CLUTCH sensitivity coefficients were once again indistinguishable from the reference sensitivities in the figures.

Table 3.12: Comparison with the IFP-20 reference case for the PST problem

	Conven. TSUNAMI	**Diff. Operator**	**IFP-5**	**Contrib.**	**CLUTCH**	**Contrib. -IFP Hybrid**
Norm. $\chi 2$	20.5808	12.3360	1.0748	1.1052	1.0867	1.3907
p-value	0.0000	0.0000	0.1847	0.1094	0.1542	0.0000

Table 3.13: Comparison with the direct perturbation case for the PST problem

	Conven. TSUNAMI	**Diff. Operator**	**IFP-5**	**Contrib.**	**CLUTCH**	**Contrib. -IFP Hybrid**
Norm. $\chi 2$	4.2119	1.6366	1.4226	1.4336	1.4502	1.3498
p-value	0.0000	0.0038	0.0299	0.0271	0.0234	0.0539

Tables 3.12 and 3.13 show the results of the chi-squared comparison between the calculated sensitivity coefficients, and those from the IFP-20 and direct perturbation reference cases, respectively. The results of the chi-squared comparison in Table 3.12 confirms the trends seen in PST sensitivity coefficient graphs; the IFP-5, Contributon, and CLUTCH methods agree well with the reference sensitivity coefficients and the conventional TSUNAMI and Differential Operator methods produced sensitivity

coefficients that were significantly different from the reference sensitivities. Although the Contributon-IFP Hybrid method produced a normalized χ^2 statistic that was much closer to one than those from the conventional TSUNAMI and Differential Operator methods, its sensitivity coefficients were still significantly different from the reference sensitivities. The comparison with the direct perturbation sensitivity coefficients that is shown in Table 3.13 suggests that the methods produced poor estimates of the sensitivity coefficients for the PST problem, but this is again likely a result of a poor set of direct perturbation reference sensitivities.

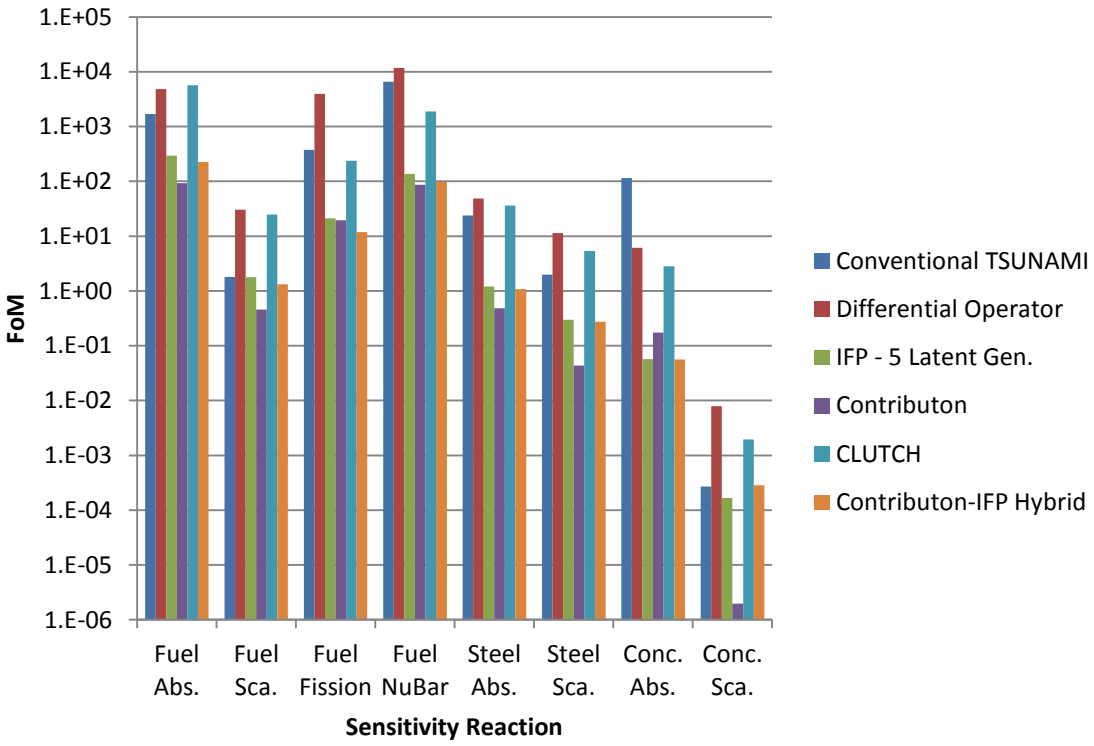

Figure 3.36: Figure of merit comparison for the PST sensitivity coefficients.

Figure 3.36 shows the FoM that were generated using each sensitivity coefficient method, and indicates that the conventional TSUNAMI, Differential Operator, and CLUTCH methods once again produced the highest FoM. The Contributon method, which was seen to produce very low FoM for the sensitivity coefficients in the MCT problem, performed much better for the PST problem, producing FoM that were similar in magnitude to those from the IFP-5 and Contributon-IFP Hybrid calculations. This was

surprising considering the large runtime increase shown in Table 3.14 that was caused by the Contributon method.

Table 3.14: PST runtime comparison

	Conven. TSUNAMI	**Diff. Operator**	**IFP-5**	**Contrib.**	**CLUTCH**	**Contrib. -IFP Hybrid**
Runtime (minutes)	207.24	32.79	96.95	4933.04	40.61	217.88
Runtime Increase	621.3%	14.1%	237.4%	17068.3%	41.3%	658.3%

3.5 LEU-COMP-THERM-050 Case 14 Results

The LCT problem was chosen to test the sensitivity coefficient methods due to the significant amount of heterogeneity present in the system. As shown in Figure 3.37, the LCT problem consists of an irregular lattice of fuel pins surrounding a central column containing an aqueous solution of samarium and other fission products, sitting on a steel plate and partially submerged in water. The LCT model used in this study was slightly simplified by the removal of some structural components, and Figure 3.38 shows part of the experimental setup for the LCT approach to criticality experiment. The spatial effects caused by the heterogeneity present in the system and the spectral effects caused by the samarium-149 near thermal absorption resonances make the LCT problem difficult to solve. Most simulations for the LCT problem tallied sensitivity coefficients over 1,000 active generations, but the Contributon simulation used only 75 active generations because of the large (about a factor of 600) increase in runtime seen for the problem. Generating the $F^*(r)$ mesh for the Contributon and CLUTCH methods is described in chapter 4. Figures 3.39 through 3.43 show the fuel absorption, scatter, fission, $\bar{\nu}$, and constrained chi sensitivity coefficients obtained for the LCT problem, respectively. Figures 3.44 and 3.45 show the water moderator absorption and scatter sensitivity coefficients, respectively, Figures 3.46 and 3.47 show the clad absorption and scatter sensitivity coefficients, respectively, Figures 3.48 and 3.49 show the samarium solution

absorption and scatter sensitivity coefficients, respectively, and Figures 3.50 and 3.51 show the steel plate absorption and scatter sensitivity coefficients, respectively.

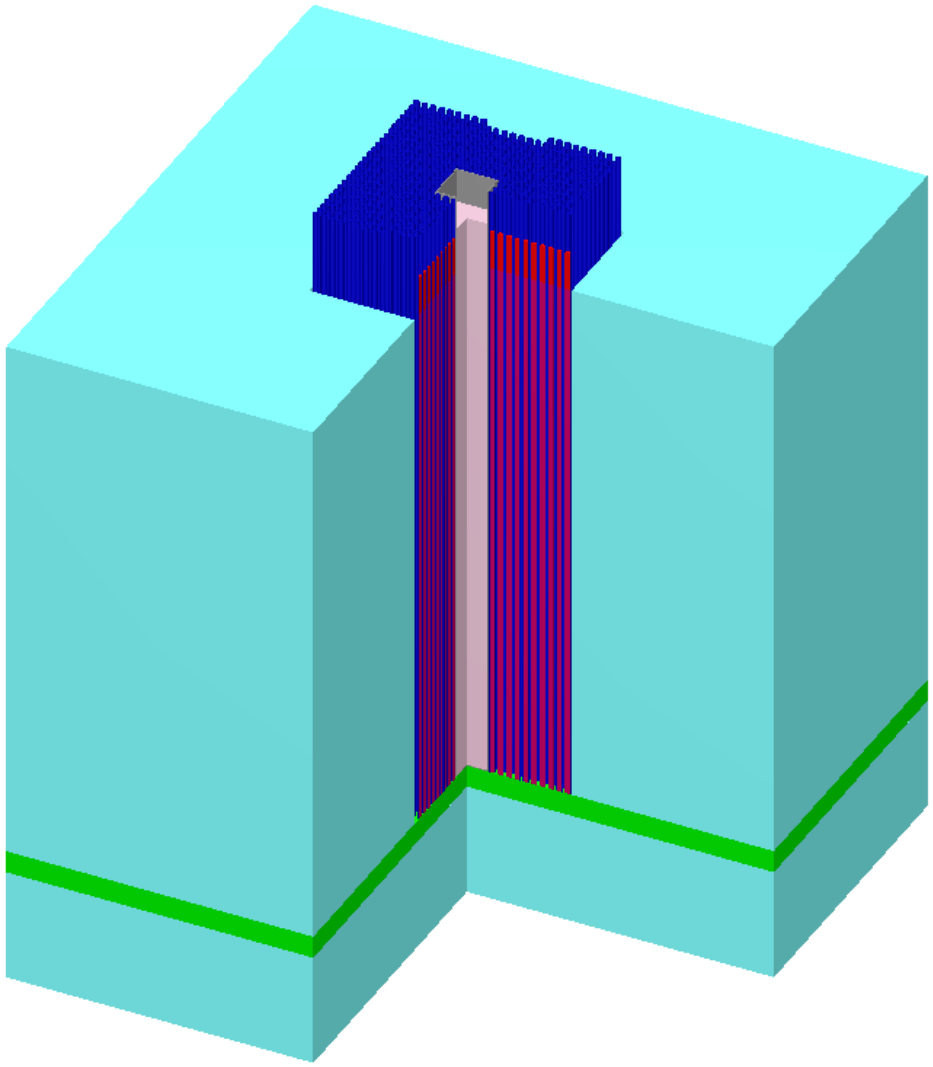

Figure 3.37: KENO-3D image of the LCT problem; fuel (red) sits inside of clad (dark blue) and on top of a steel plate (green), surrounding a samarium solution (pink) and surrounded by water (light blue).

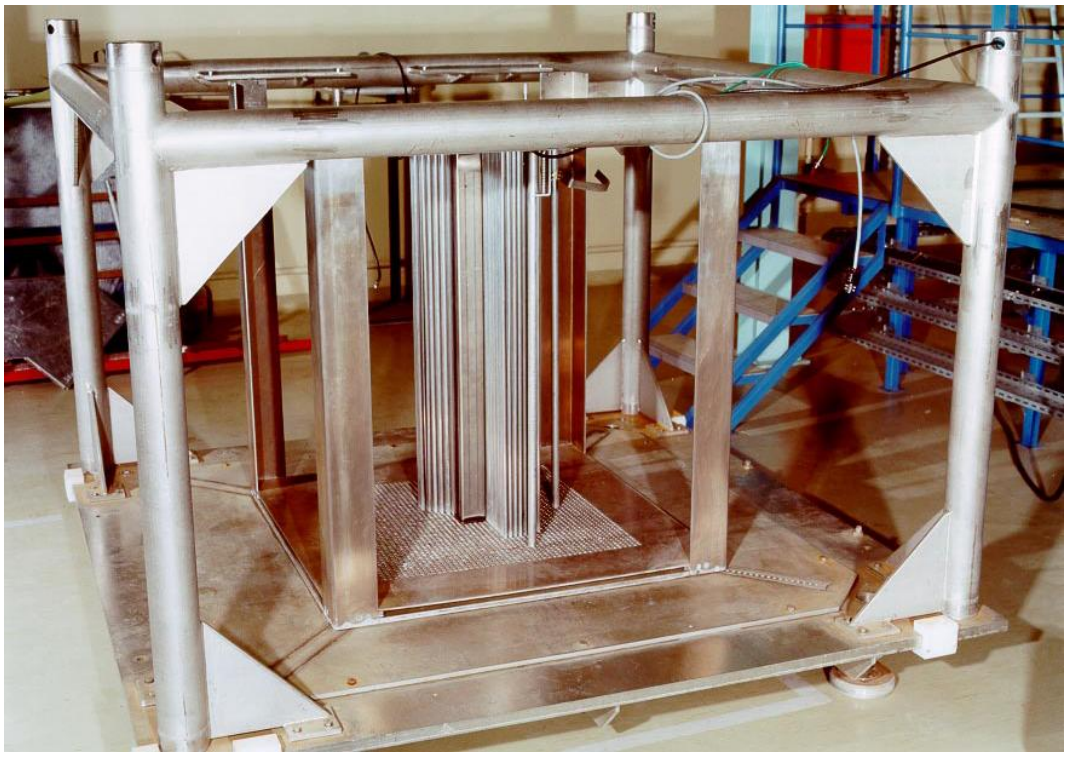

Figure 3.38: View of the central samarium solution tank partially surrounded by the fuel rod array [23].

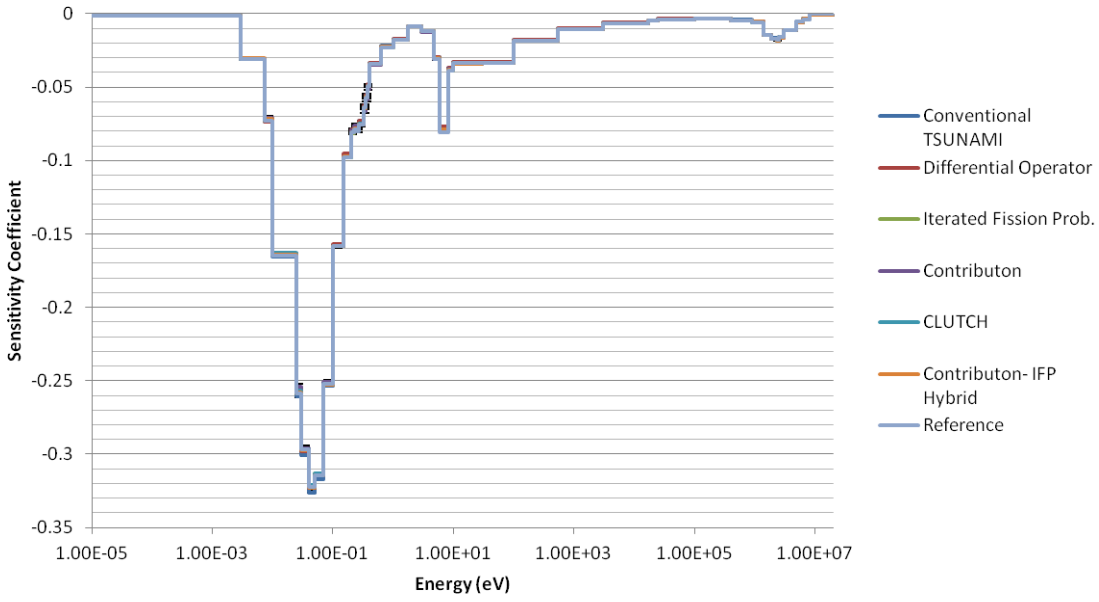

Figure 3.39: LCT fuel absorption sensitivity coefficients.

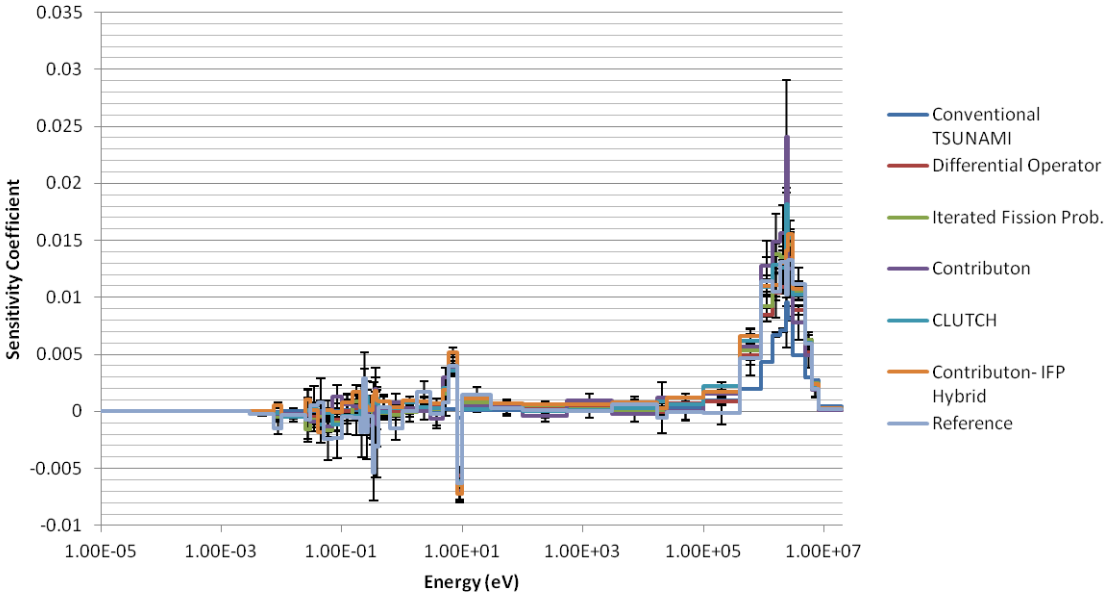

Figure 3.40: LCT fuel scatter sensitivity coefficients.

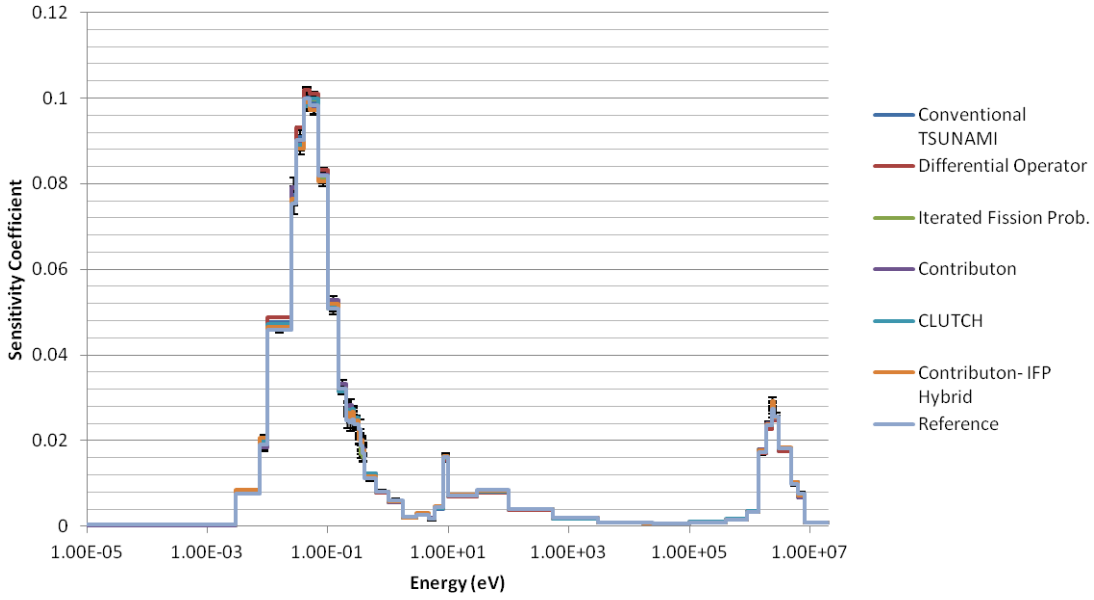

Figure 3.41: LCT fuel fission sensitivity coefficients.

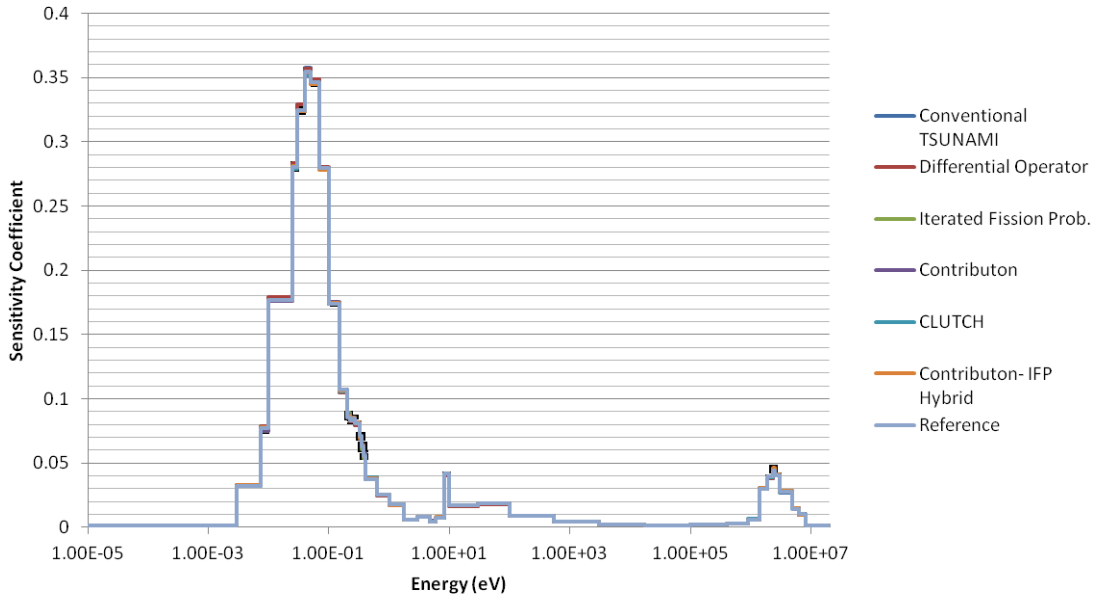

Figure 3.42: LCT fuel $\bar{\nu}$ sensitivity coefficients.

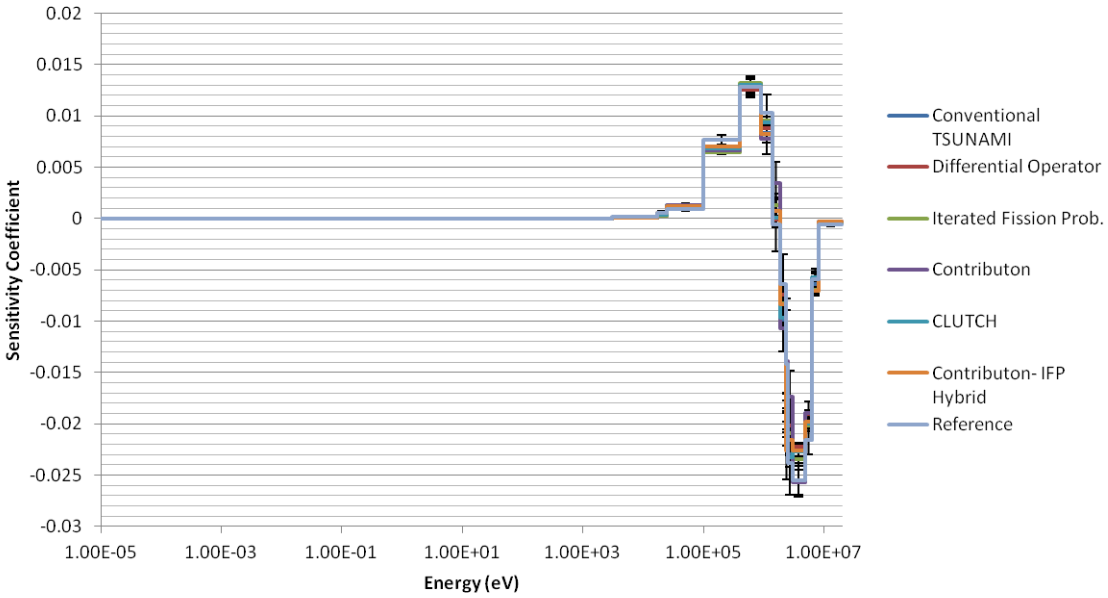

Figure 3.43: LCT fuel constrained chi sensitivity coefficients.

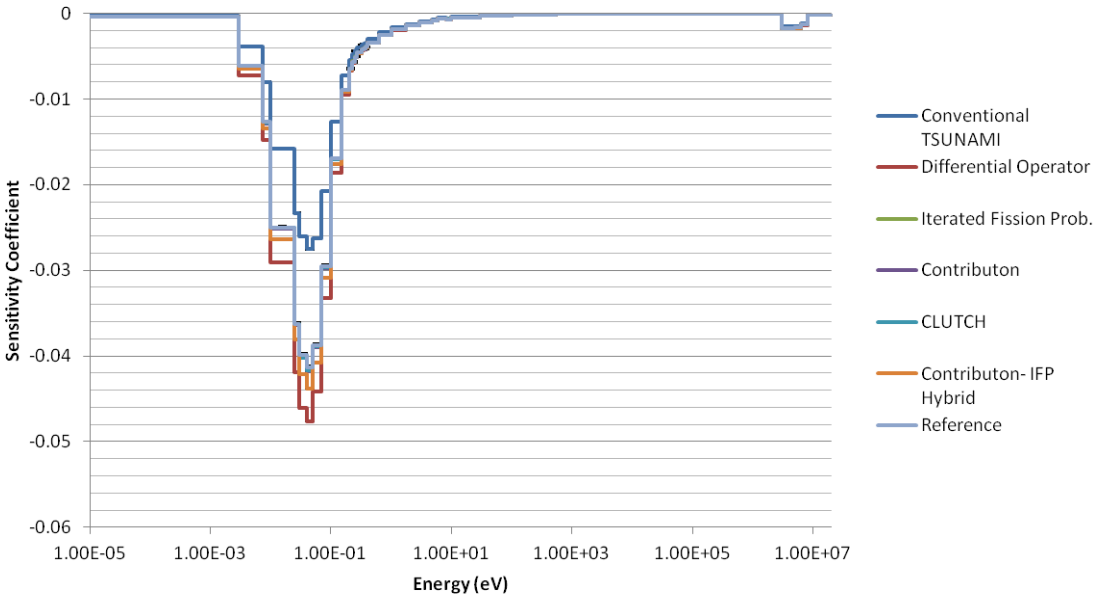

Figure 3.44: LCT moderator absorption sensitivity coefficients.

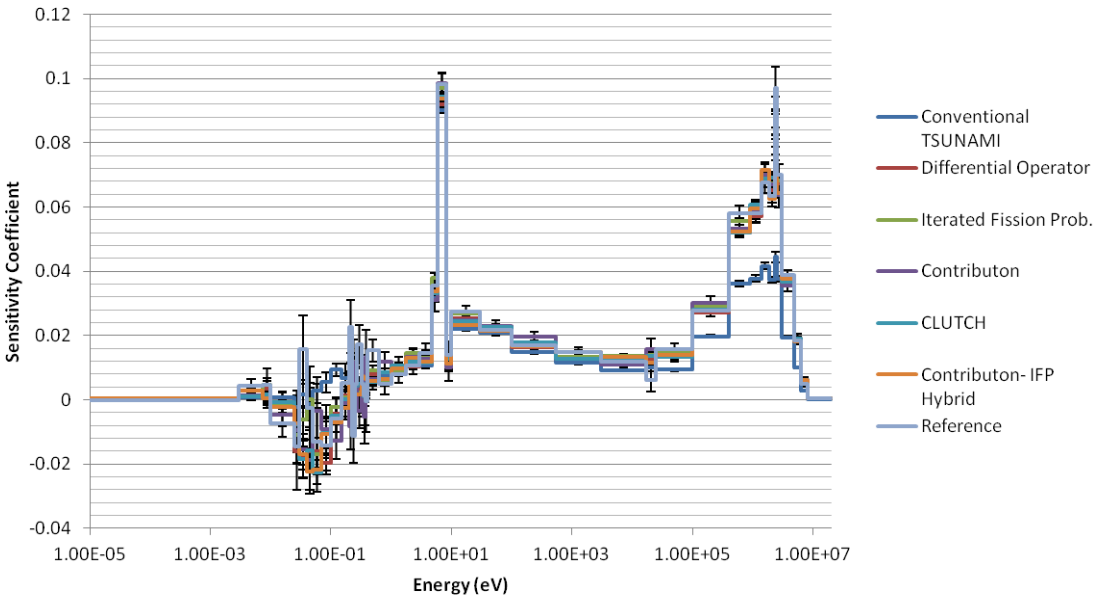

Figure 3.45: LCT moderator scatter sensitivity coefficients.

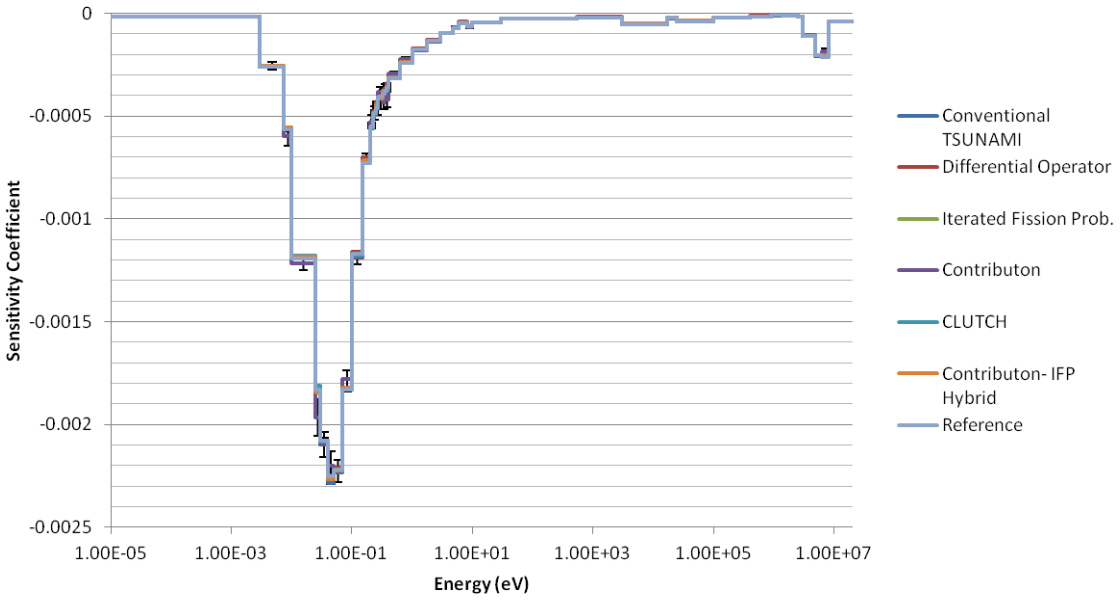

Figure 3.46: LCT clad absorption sensitivity coefficients.

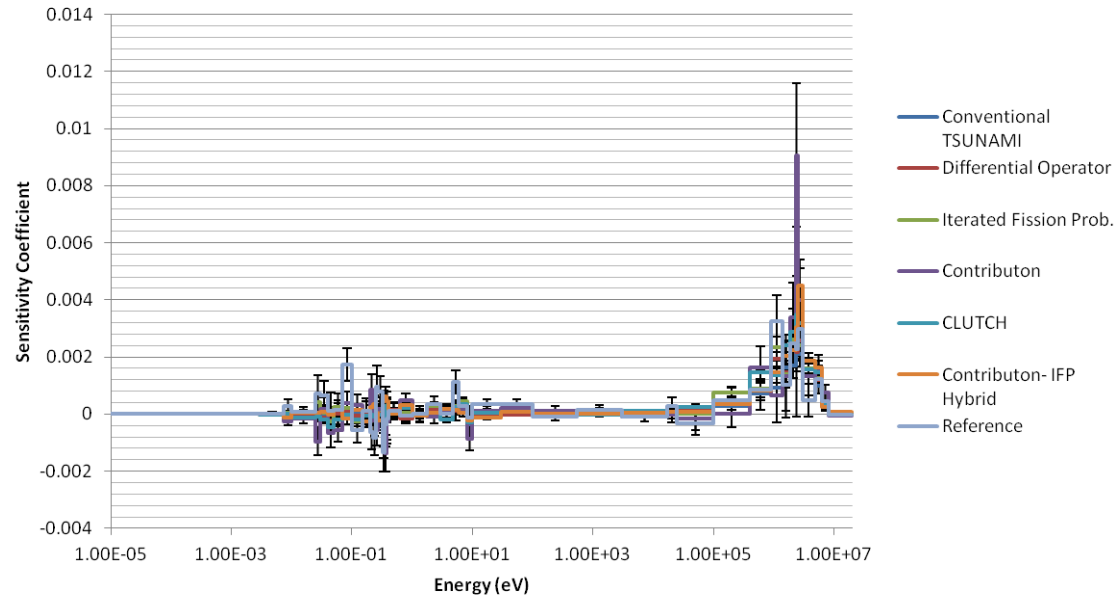

Figure 3.47: LCT clad scatter sensitivity coefficients.

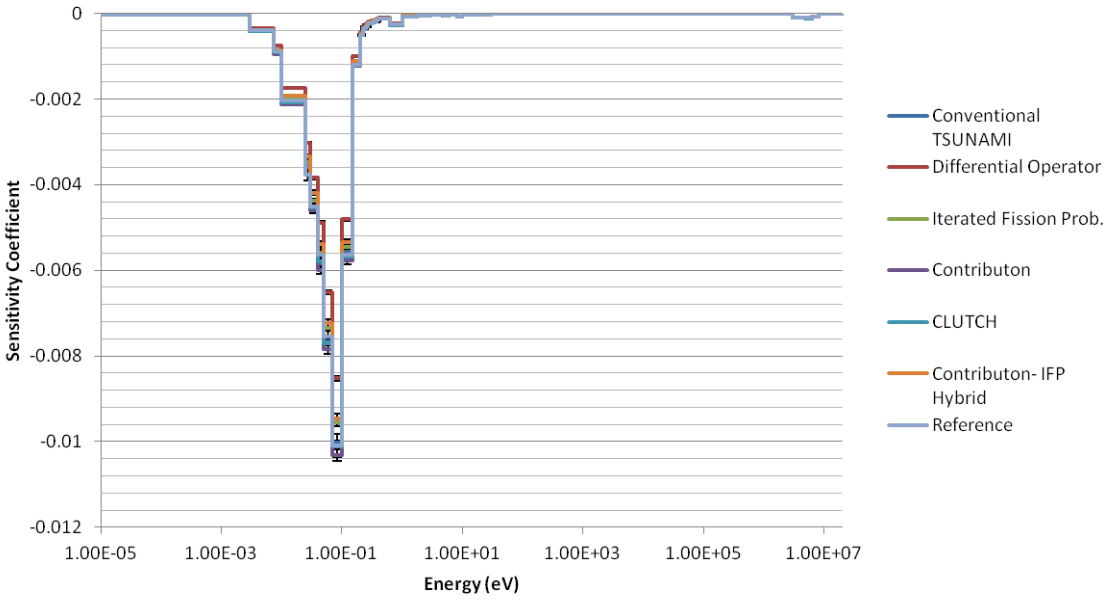

Figure 3.48: LCT samarium solution absorption sensitivity coefficients.

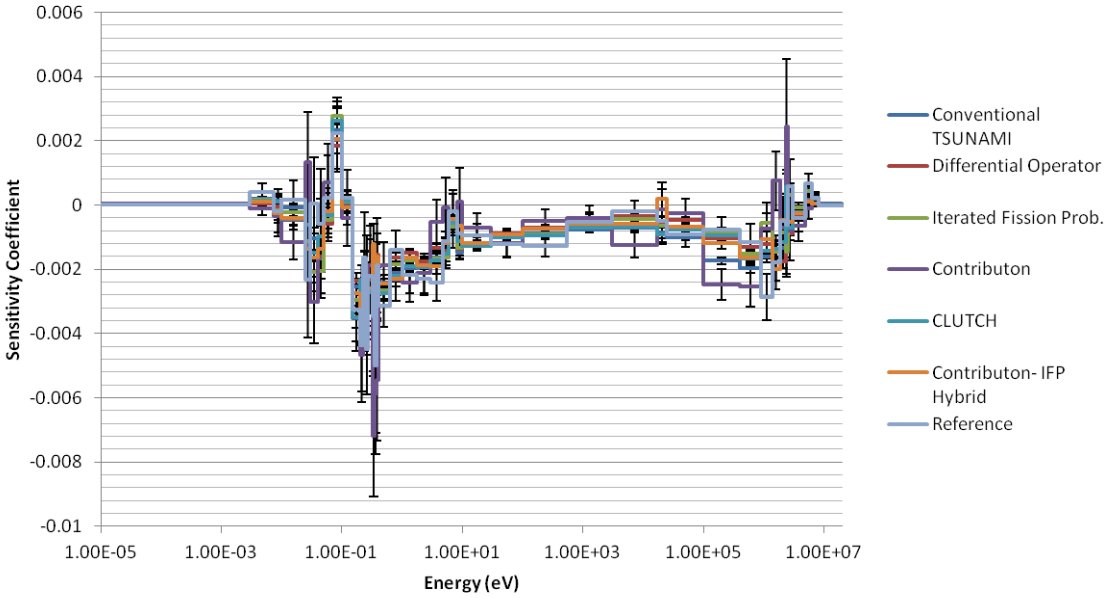

Figure 3.49: LCT samarium solution scatter sensitivity coefficients.

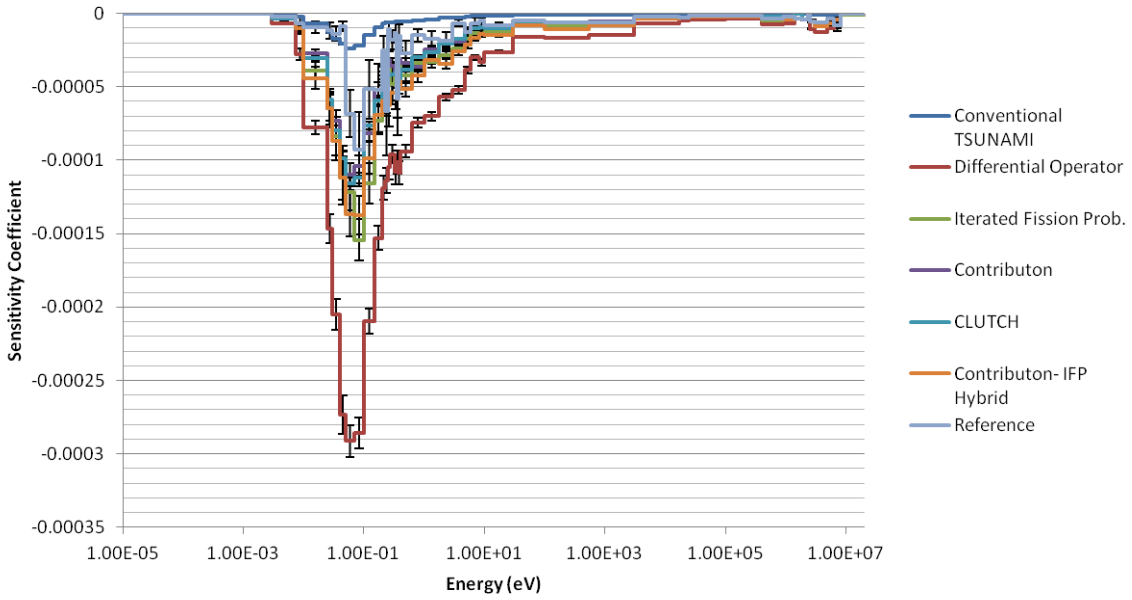

Figure 3.50: LCT steel plate absorption sensitivity coefficients.

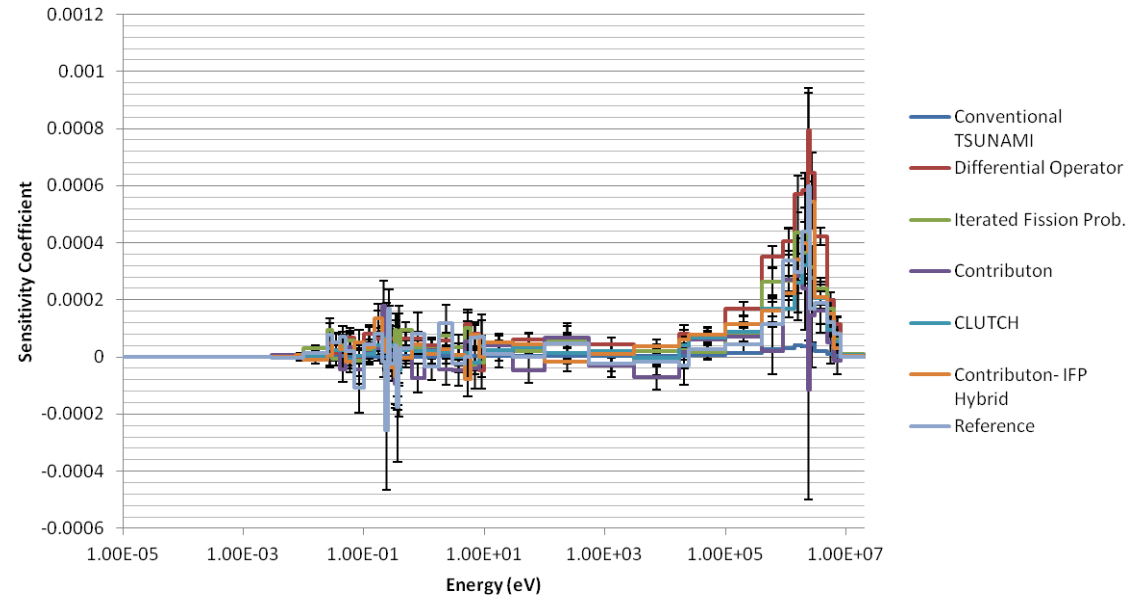

Figure 3.51: LCT steel plate scatter sensitivity coefficients.

Although the MCT and LCT models contain fuel with different isotopic compositions, the sensitivity coefficients generated for the problems behave similarly. The sensitivity coefficients typically reach their maximum value near the thermal

energies where the fission cross sections are at their maximum, and the scattering sensitivities are generally larger at higher energies because scattering events at these energies prevent fast neutrons from escaping the system. The steel and clad sensitivities were typically small, and exhibited large uncertainties for the scattering reactions. While the fuel absorption sensitivity coefficient peaks around 0.01 eV, the samarium solution absorption sensitivity coefficient peaks near 0.1 eV because of the large Sm-149 absorption resonances that occur near this energy. The samarium solution scattering sensitivity coefficients are negative because any scattering events in samarium stop neutrons that would otherwise stream back into the fuel region and also because scattering events allow neutrons to downscatter into the Sm-149 resonance range while they are in the samarium solution. As was observed in the MCT problem, the LCT chi sensitivity coefficients are positive for lower energies and negative at higher energies, indicating that the increase in the fast fission factor caused by birthing neutrons at fast energies is more than offset by the increased leakage probability for neutrons at these energies.

As shown in Figures 3.39 through 3.51, the IFP-5, Contributon, and CLUTCH sensitivity coefficients were again mostly indistinguishable from the reference sensitivity coefficients; the results of the chi-squared test comparing the sensitivity coefficient methods with the IFP-20 reference sensitivities in Table 3.15 confirm this, and these three sensitivity methods produced p-values that did not indicate a statistically-significant difference from the reference sensitivities. Direct perturbation sensitivity coefficient calculations were not performed for the LCT problem. With the exception of the moderator absorption and steel plate sensitivity coefficients, the Differential Operator method sensitivities are usually very close to the reference sensitivity coefficients in Figures 3.39 through 3.51; however, the results of the chi-squared comparison in Table 3.15 indicate that the Differential Operator method differed significantly from the reference calculation. The Contributon-IFP Hybrid method produced sensitivity coefficients that were close to the reference sensitivities in Figures 3.39 through 3.51 and resulted in a normalized χ^2 statistic that was not outrageously far from a statistic that would produce good p-values; however, the method once again produced sensitivity coefficients that differed significantly from the reference sensitivities. The conventional

TSUANMI sensitivity coefficients generally agreed well with the reference sensitivities, but large differences were observed for some of the absorption sensitivity coefficients. While these differences may be due to the differences in the TSUNAMI and Shift physics packages and could be attributed to an insufficiently resolved TSUNAMI flux mesh, these differences may be caused by an assumption inherent to the TSUNAMI methodology. When tallying sensitivity coefficients TSUNAMI groups the angular fluxes into solid angle bins that assume a constant angular flux within the bin. As shown in Eq. 2.11, the absorption sensitivity coefficient is calculated by integrating the product of the forward and adjoint fluxes over all energies. Thus, when calculating the absorption sensitivities TSUNAMI calculates the product of averages instead of the average of products because of its grouping of the angular flux into solid angle bins. TSUNAMI's approach of binning the angular flux tallies into angular bins introduces more inaccuracy for the absorption sensitivity coefficient calculations than the fission source and chi sensitivity terms because the angular flux terms in the expressions for the fission source and chi sensitivity terms are used to calculate scalar fluxes, and are not multiplied together before being integrated over all angles. TSUNAMI's approach of binning the angular fluxes into angular bins may be responsible for the disagreement seen for the conventional TSUNAMI absorption sensitivity coefficients.

Table 3.15: Comparison with the IFP-20 reference case for the LCT problem

	Conven. TSUNAMI	**Diff. Operator**	**IFP-2**	**Contrib.**	**CLUTCH**	**Contrib. -IFP Hybrid**
Norm. $\chi 2$	837.7880	18.5387	0.5077	1.0679	0.9741	2.9758
p-value	0.0000	0.0000	0.9999	0.1512	0.6451	0.0000

Figure 3.52 compares the FoM that were produced by each sensitivity coefficient method for the LCT problem. The trends in the sensitivity coefficient method efficiency that were previously observed were once again seen for the LCT problem: the conventional TSUANMI, Differential Operator, and CLUTCH methods produced sensitivity coefficients with the highest FoM, followed by the IFP and Contributon-IFP Hybrid methods, and followed lastly by the Contributon method. The IFP and

Contributon-IFP Hybrid methods once again produced FoM that were similar in magnitude, but the performance of the IFP method is expected to improve for continuous-energy calculations.

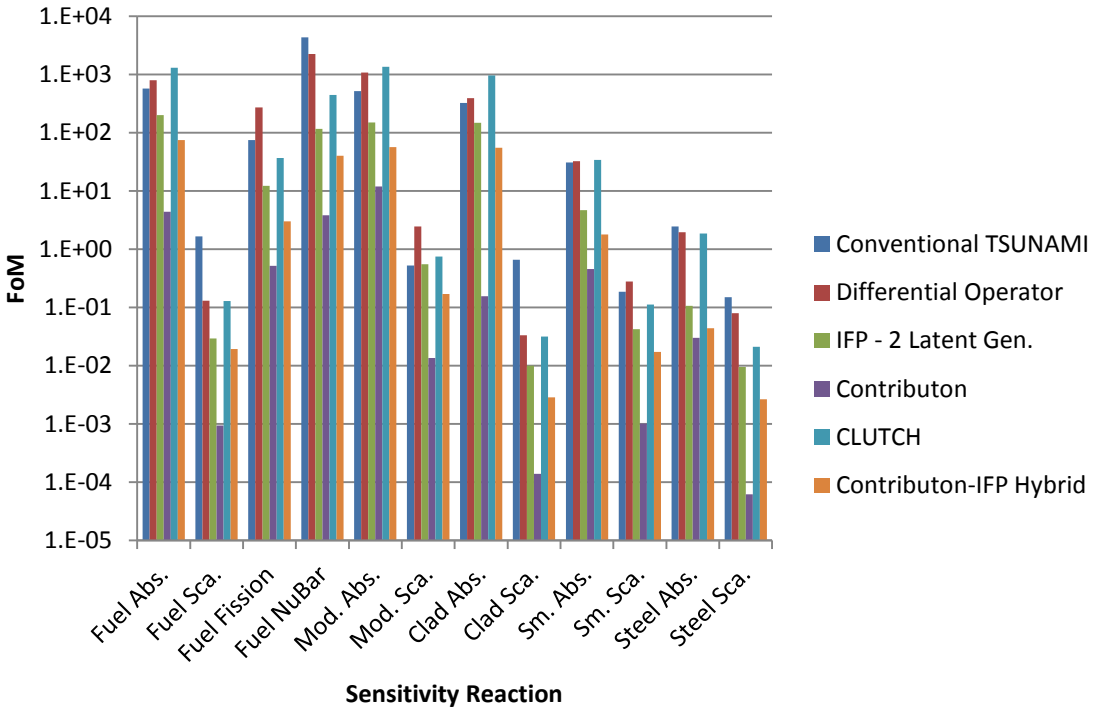

Figure 3.52: Figure of merit comparison for the LCT sensitivity coefficients.

Table 3.16 compares the runtimes for the LCT problem for each sensitivity coefficient method. The runtime increased caused by the Contributon method is not shown in the table because the Contributon method used a different number of active generations than the other simulations. The Differential Operator, IFP, and CLUTCH methods resulted in a significant increase in problem runtime, but this large runtime increase will most likely not be seen for continuous-energy calculations because it is likely due to the increased amount of data processing required by these methods. On the other hand, the runtime increase seen for the CLUTCH and Contributon-IFP methods is caused by the simulation of secondary particles, and will likely propagate to continuous-energy calculations.

Table 3.16: LCT runtime comparison

	Conven. TSUNAMI	**Diff. Operator**	**IFP-2**	**Contrib.**	**CLUTCH**	**Contrib. -IFP Hybrid**
Runtime (minutes)	202.82	78.46	198.18	1463.07	96.16	472.21
Runtime Increase	240.6%	31.7%	232.8%	---	61.5%	692.9%

3.6 Full-Core PWR Challenge Problem

Lastly, each of the sensitivity coefficient methods was used to calculate sensitivity coefficients for a challenge problem: a 2-D, full-core model of a PWR. As shown in Figure 3.53, the PWR model contains 192 fuel assemblies with 264 fuel pins each, and there are three different enrichments of fuel in the system: 2.2%, 2.7%, and 3.2%. Although Figure 3.53 shows a quarter of the core, the sensitivity coefficient calculations were performed for a full-core model. This problem was selected as a challenge problem because the PWR core is a very large system with significant spectral effects occurring both between fuel assemblies of different enrichments and at the edge of the core. Although the PWR model used here only contained three different fuel enrichments and a modest number of isotopes, more detailed full-core models can require sensitivity coefficient calculations using many thousands of isotopes, and memory limitations may prevent TSUNAMI and IFP sensitivity coefficient calculations for models of this scale [18].

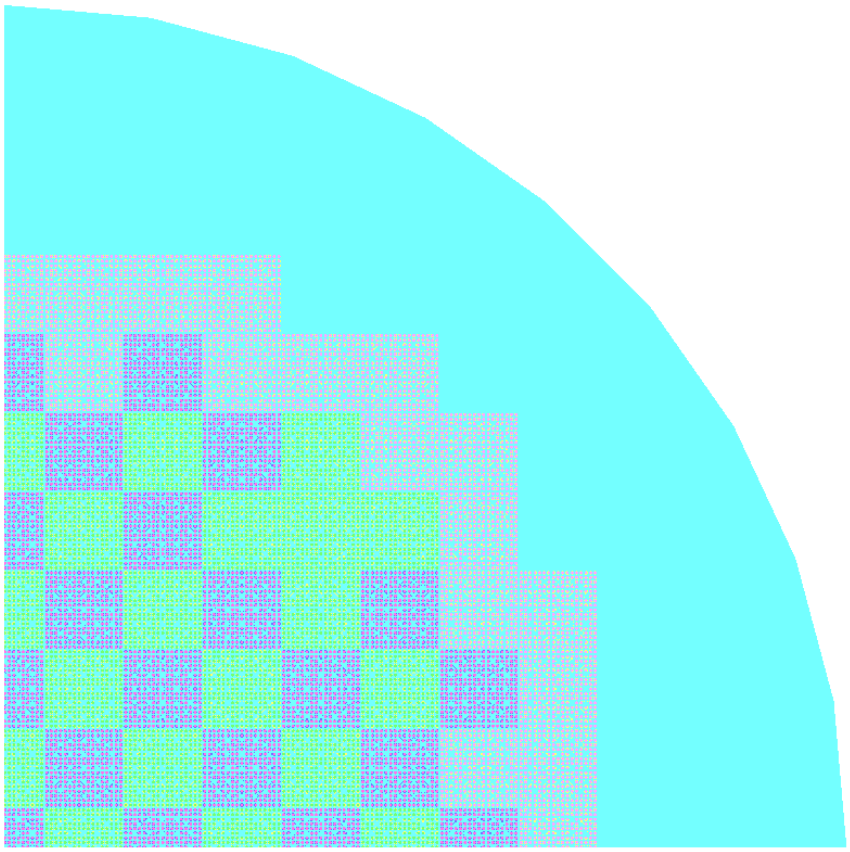

Figure 3.53: KENO-3D image of the PWR problem; fuel assemblies containing 2.2%- (green), 2.7%- (purple), and 3.2%-enriched (pink) fuel for a PWR core and are surrounded by a water reflector (light blue).

Sensitivity coefficient calculations were performed for the PWR problem using the lessons learned for chapters 4 and 3.8 for the Contributon-based and IFP methods, respectively. All Contributon-based calculations used an $F^*(r)$ mesh that placed each fuel pin in its own mesh cell, and calculated $F^*(r)$ using an IFP-based approach over 10,000 inactive generations, which corresponded to about 1,000 inactive neutron histories per each $F^*(r)$ mesh cell. All IFP calculations used a conservative 10 latent generations for calculating the asymptotic population of a progenitor. Most of these sensitivity coefficient calculations were performed over 700 active generations with 5,000 neutron histories each, but the Contributon calculation was performed using 75 active generations. Figures 3.54 through 3.68 give the absorption, scatter, fission, $\bar{\nu}$, and constrained chi sensitivity coefficients, respectively, for the 2.2%-, 2.7%-, and 3.2%-

enriched fuel, respectively, and Figures 3.69 through 3.72 give the moderator absorption, moderator scatter, clad absorption, and clad scatter sensitivity coefficients, respectively.

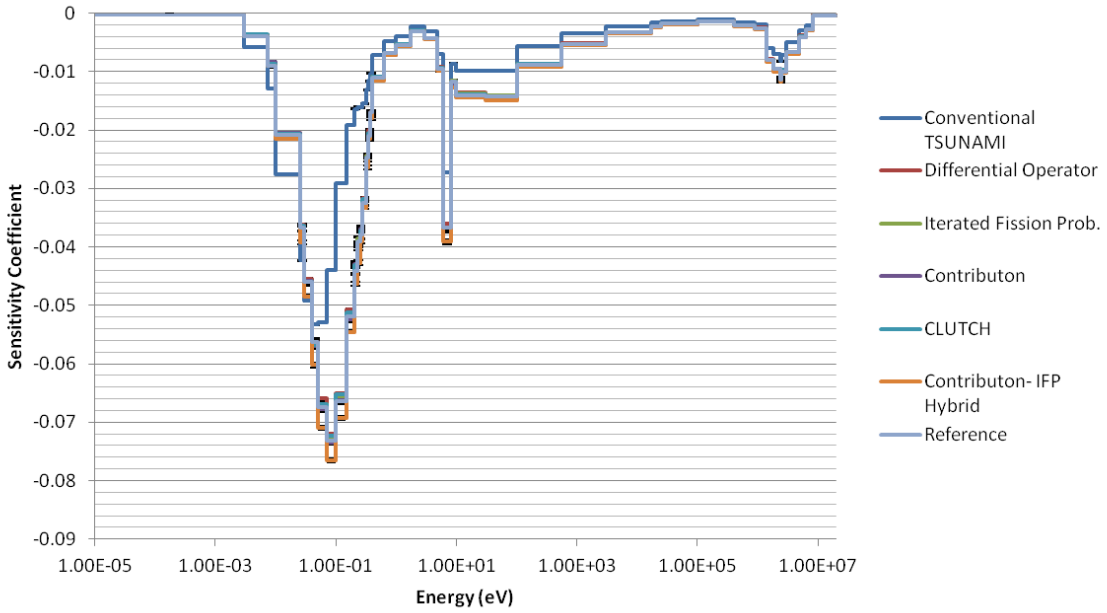

Figure 3.54: PWR 2.2%-enriched fuel absorption sensitivity coefficients.

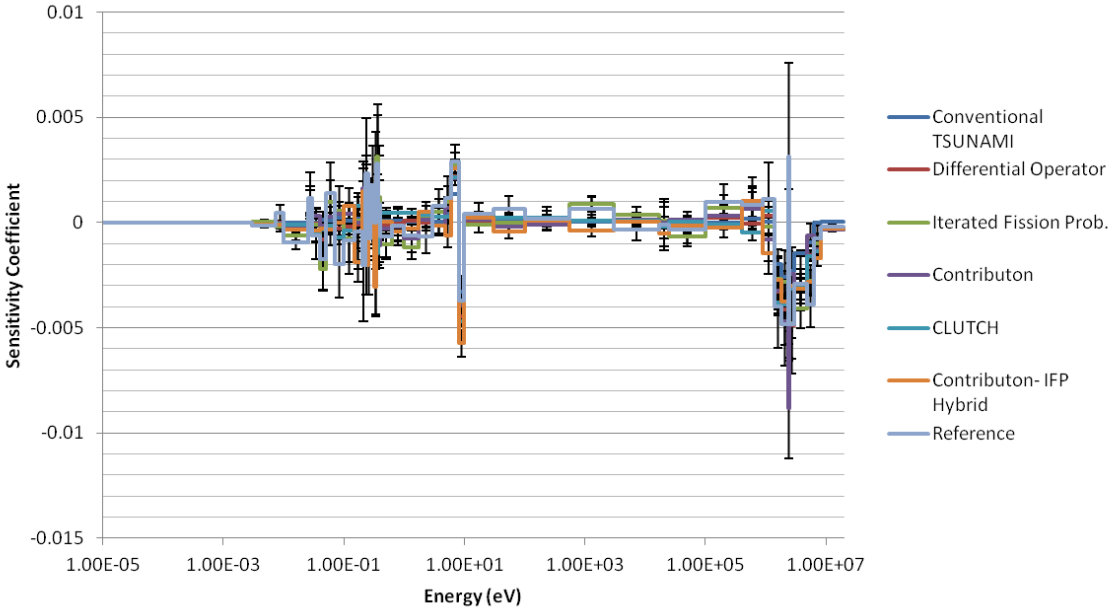

Figure 3.55: PWR 2.2%-enriched fuel scatter sensitivity coefficients.

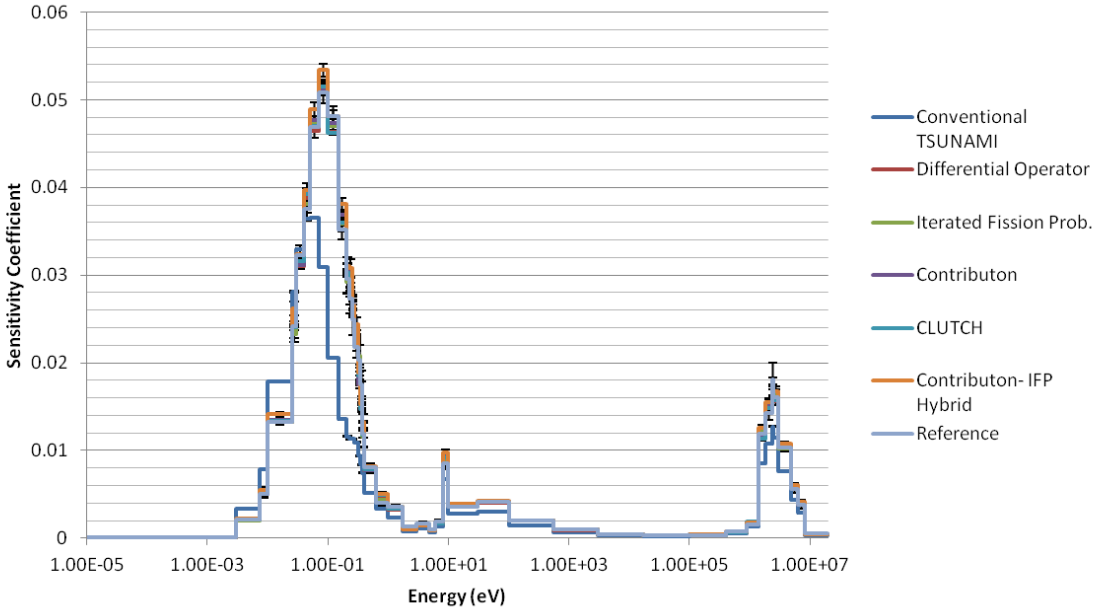

Figure 3.56: PWR 2.2%-enriched fuel fission sensitivity coefficients.

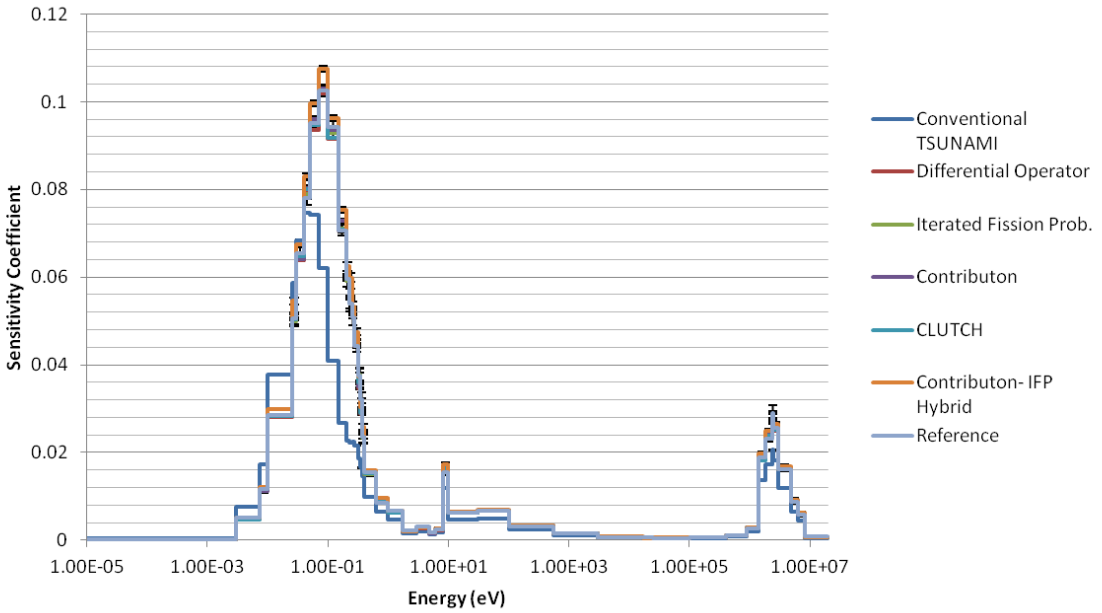

Figure 3.57: PWR 2.2%-enriched fuel $\bar{\nu}$ sensitivity coefficients.

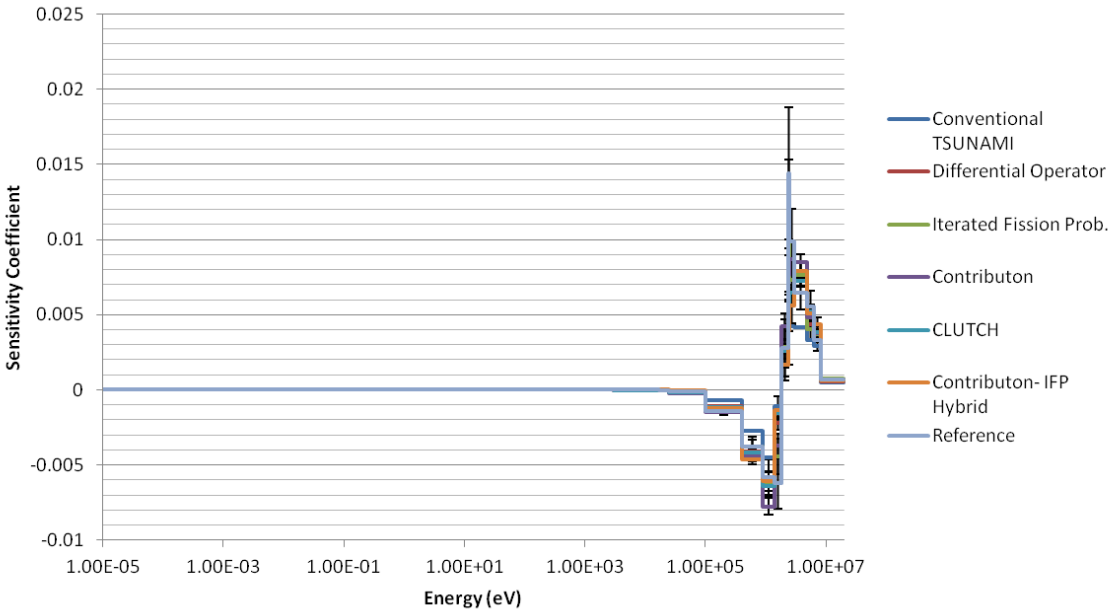

Figure 3.58: PWR 2.2%-enriched fuel constrained chi sensitivity coefficients.

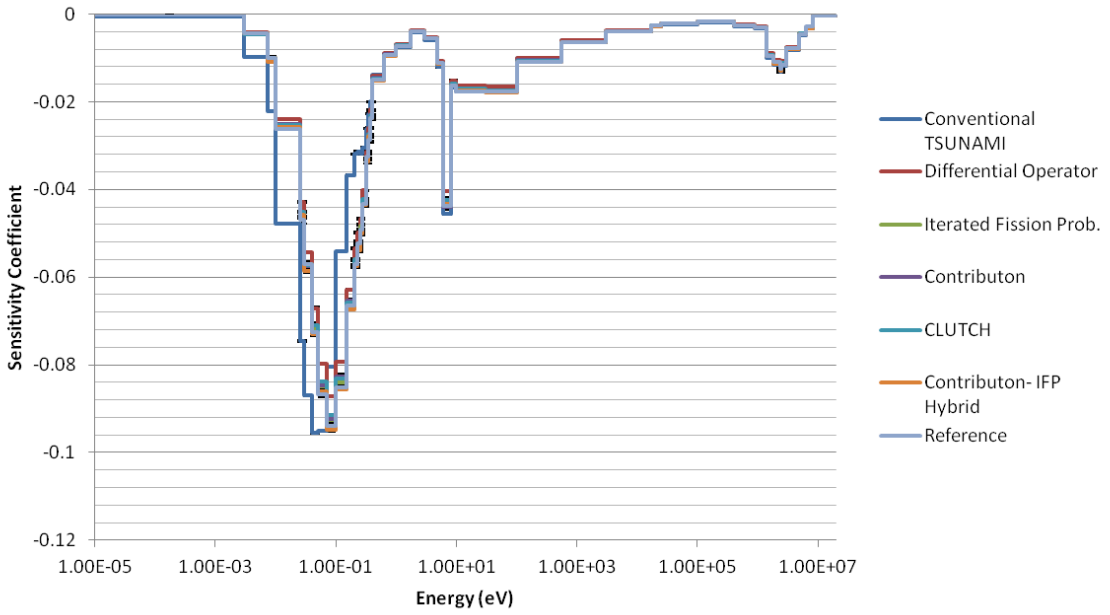

Figure 3.59: PWR 2.7%-enriched fuel absorption sensitivity coefficients.

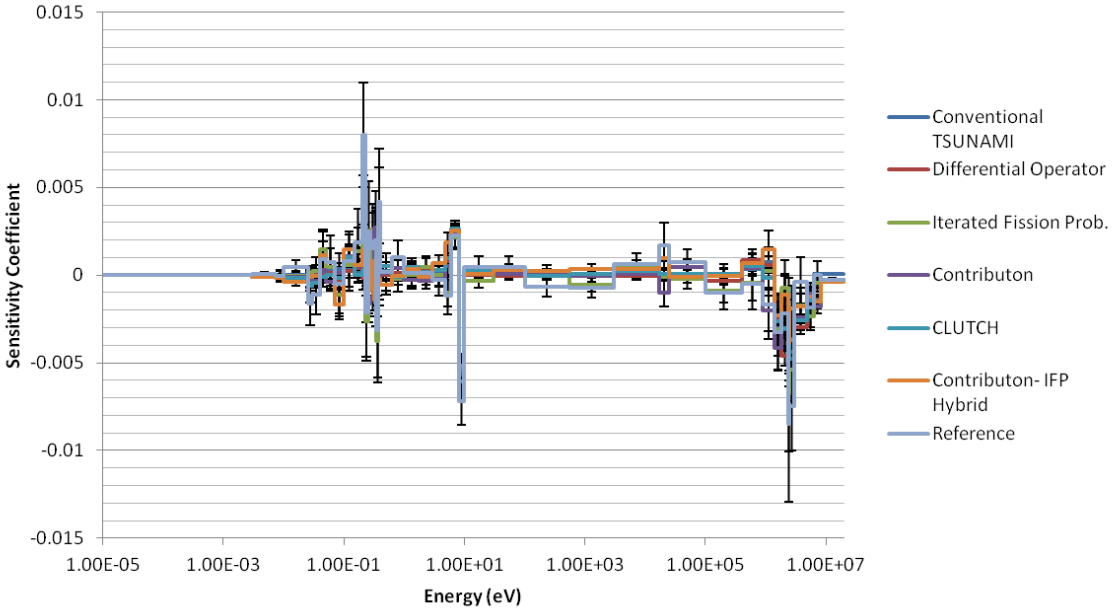

Figure 3.60: PWR 2.7%-enriched fuel scatter sensitivity coefficients.

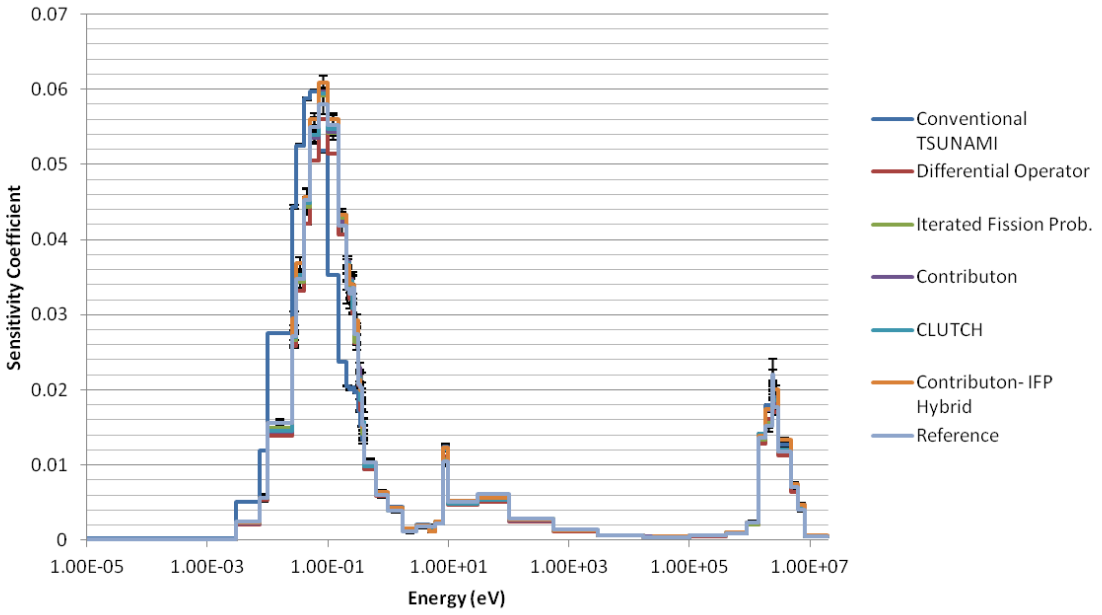

Figure 3.61: PWR 2.7%-enriched fuel fission sensitivity coefficients.

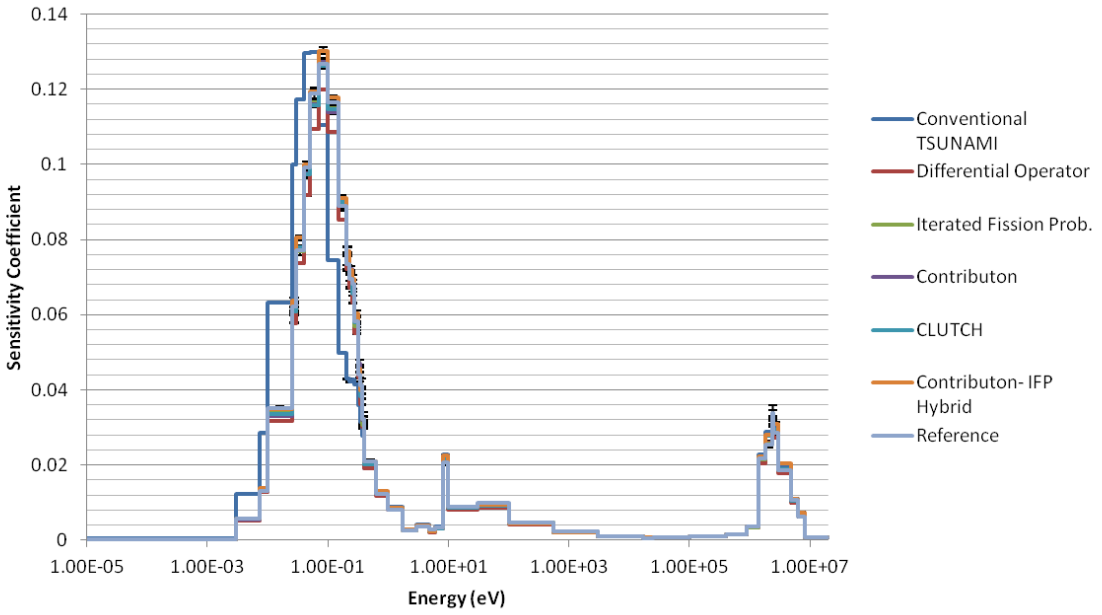

Figure 3.62: PWR 2.7%-enriched fuel $\bar{\nu}$ sensitivity coefficients.

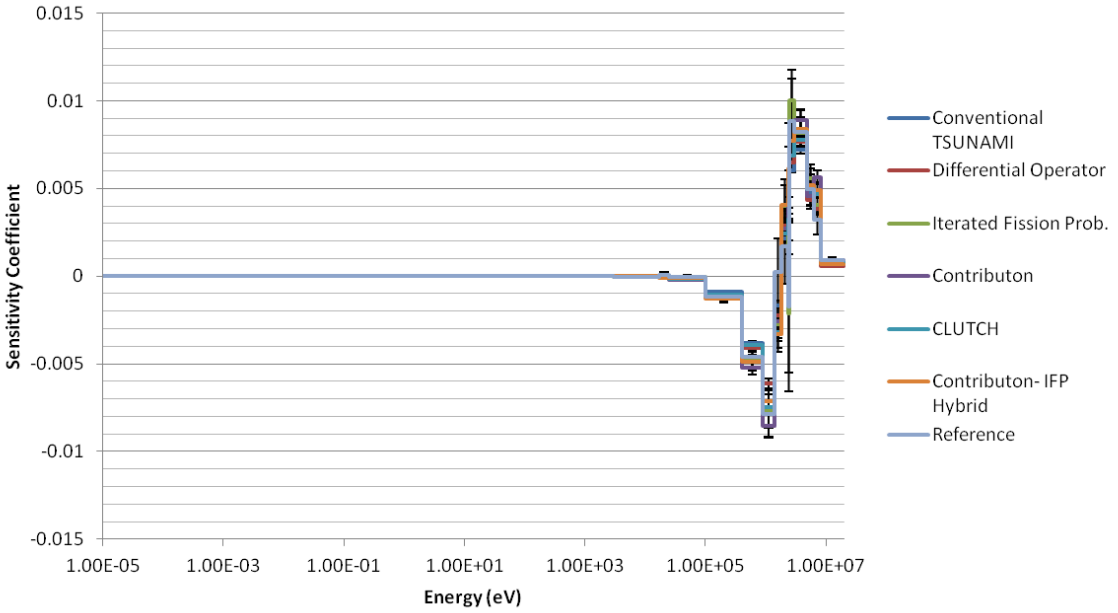

Figure 3.63: PWR 2.7%-enriched fuel constrained chi sensitivity coefficients.

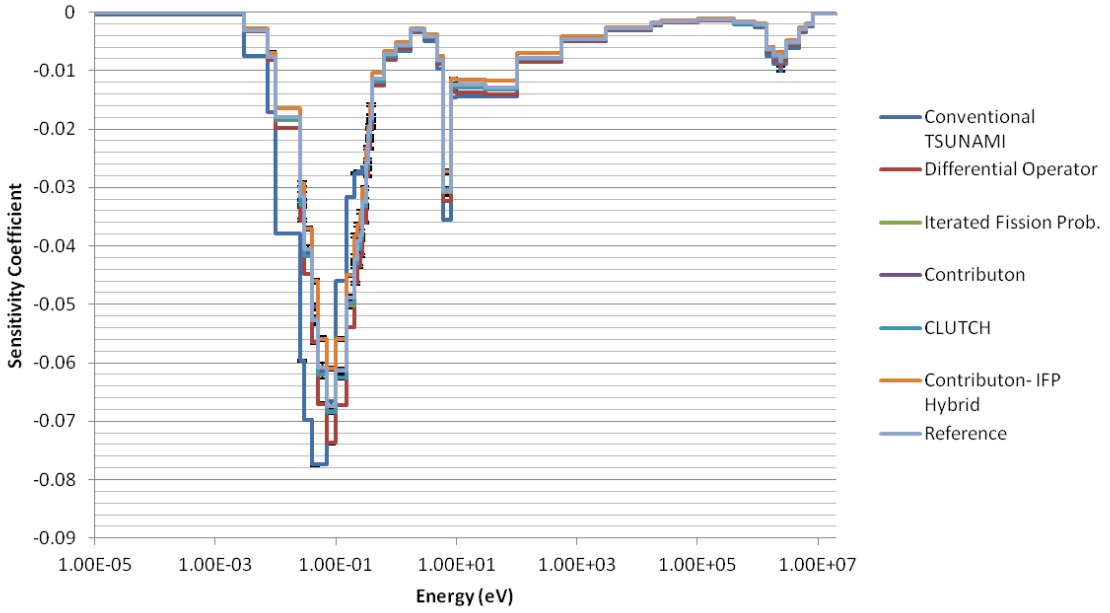

Figure 3.64: PWR 3.2%-enriched fuel absorption sensitivity coefficients.

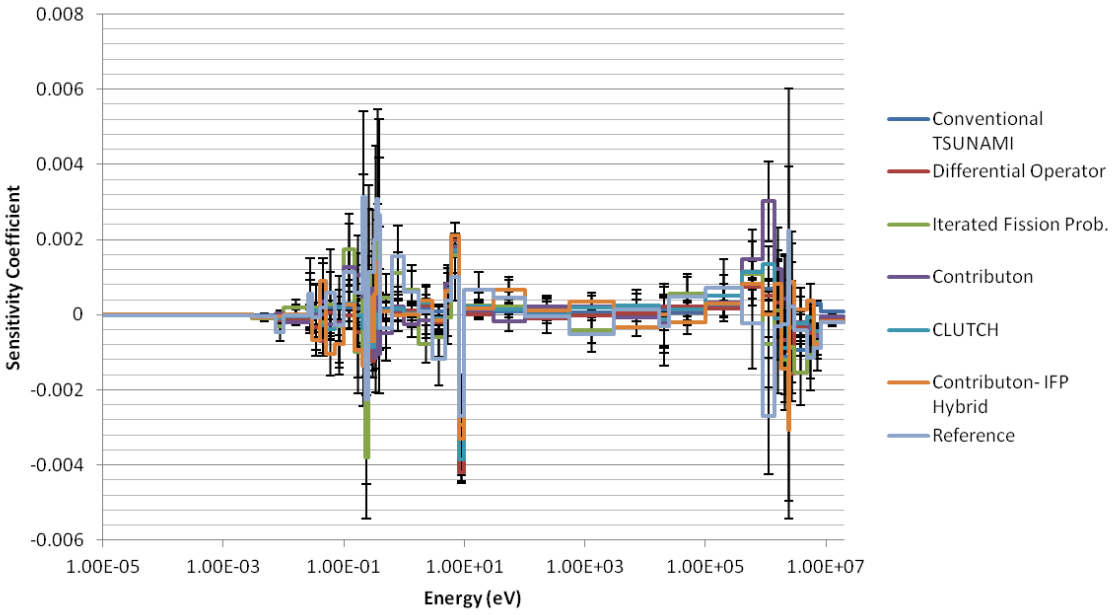

Figure 3.65: PWR 3.2%-enriched fuel scatter sensitivity coefficients.

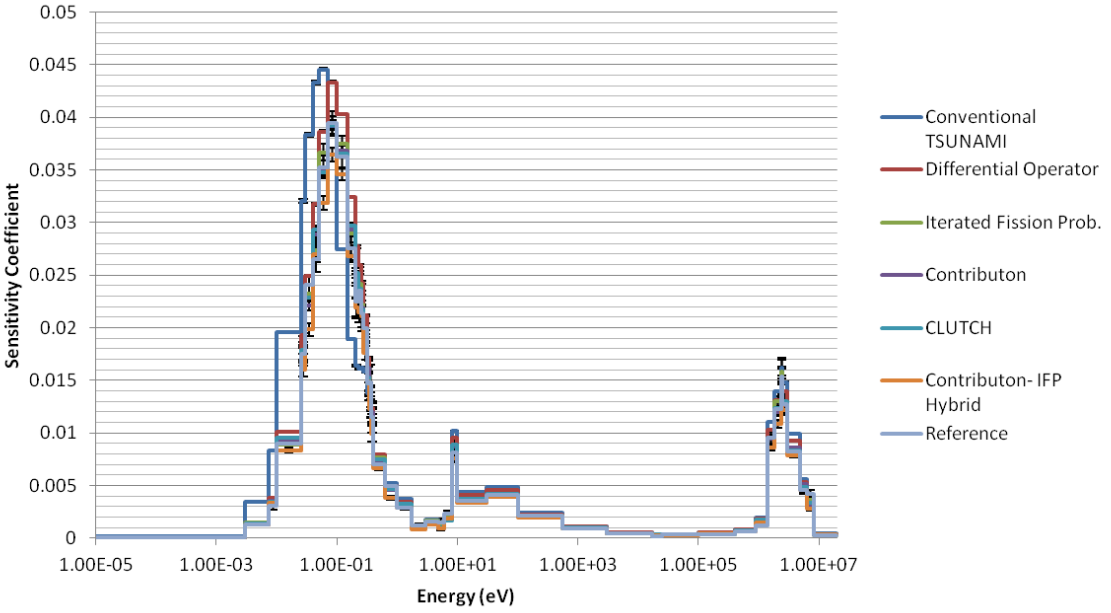

Figure 3.66: PWR 3.2%-enriched fuel fission sensitivity coefficients.

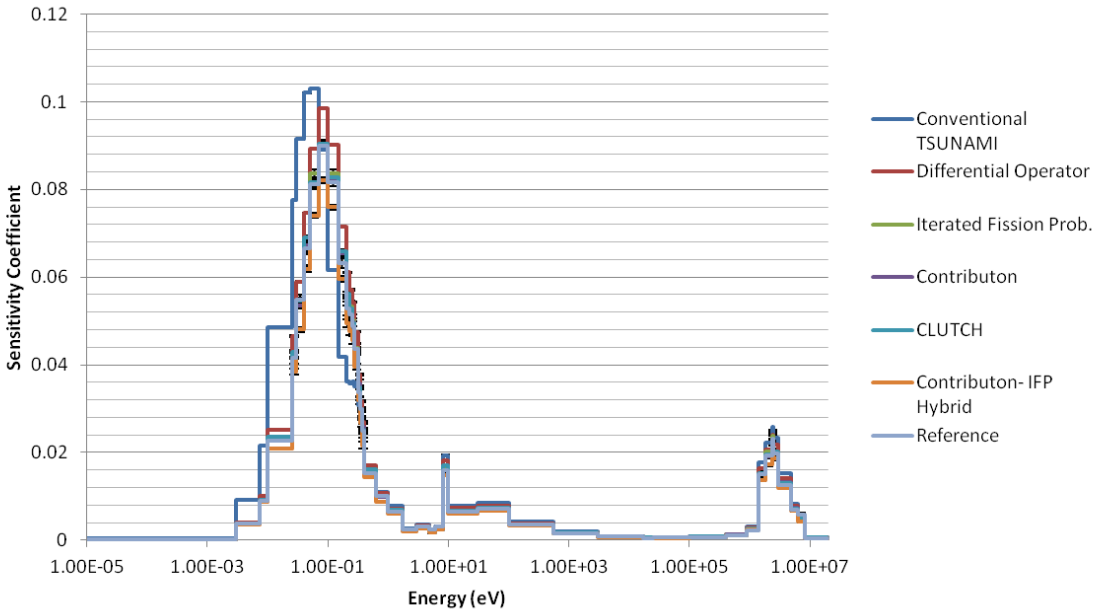

Figure 3.67: PWR 3.2%-enriched fuel $\bar{\nu}$ sensitivity coefficients.

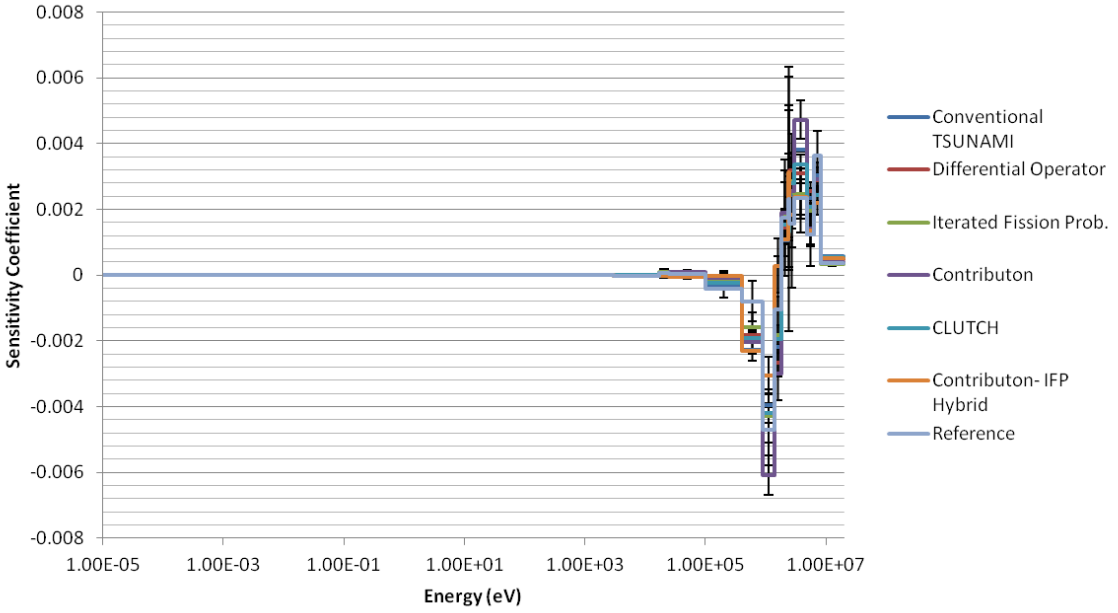

Figure 3.68: PWR 3.2%-enriched fuel constrained chi sensitivity coefficients.

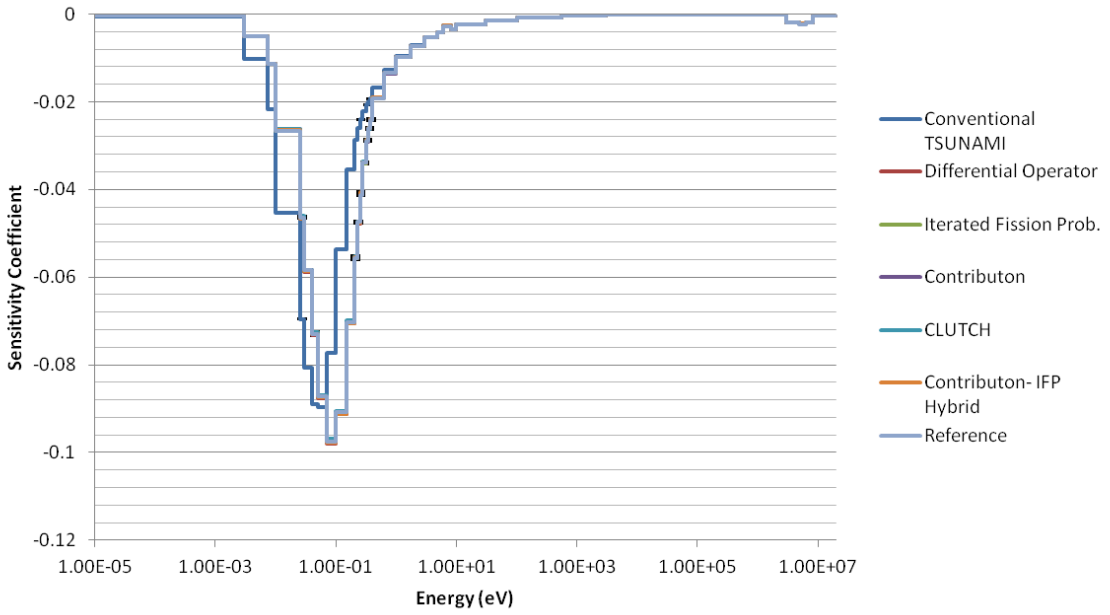

Figure 3.69: PWR moderator absorption sensitivity coefficients.

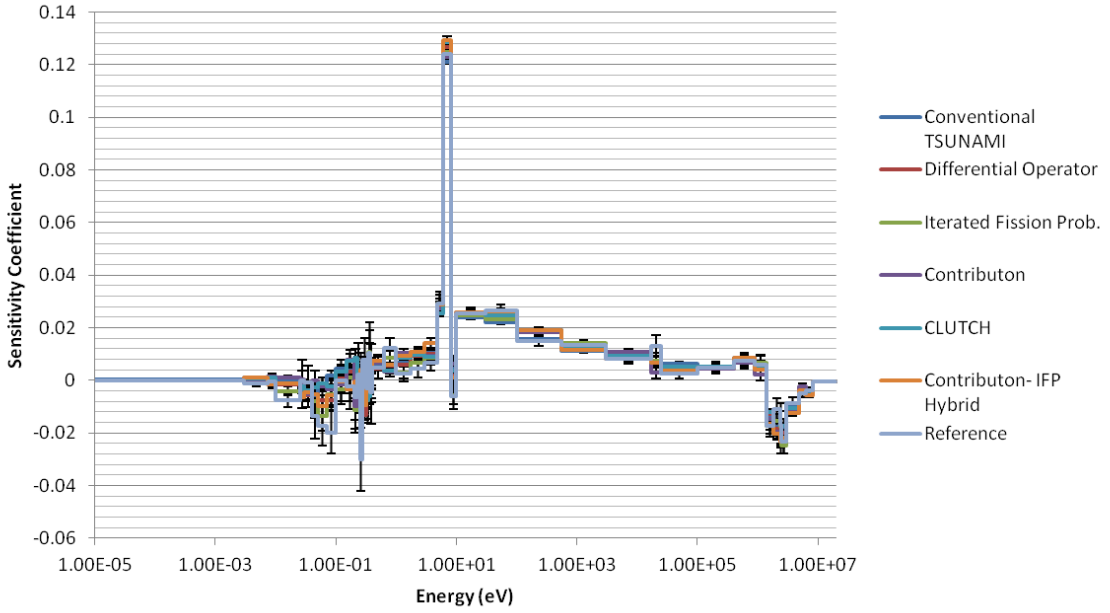

Figure 3.70: PWR moderator scatter sensitivity coefficients.

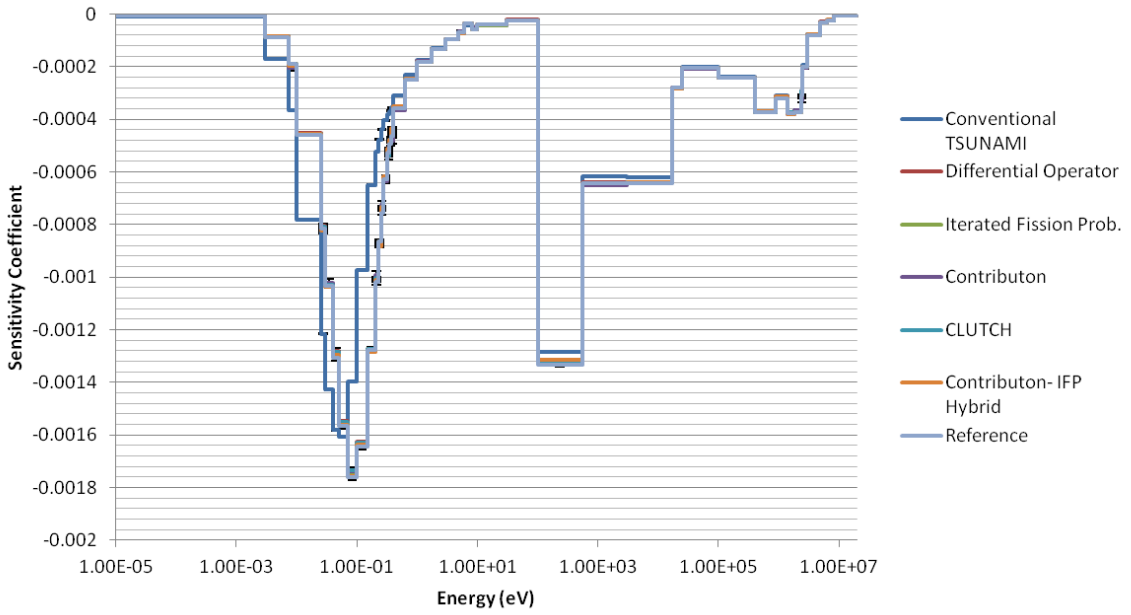

Figure 3.71: PWR clad absorption sensitivity coefficients.

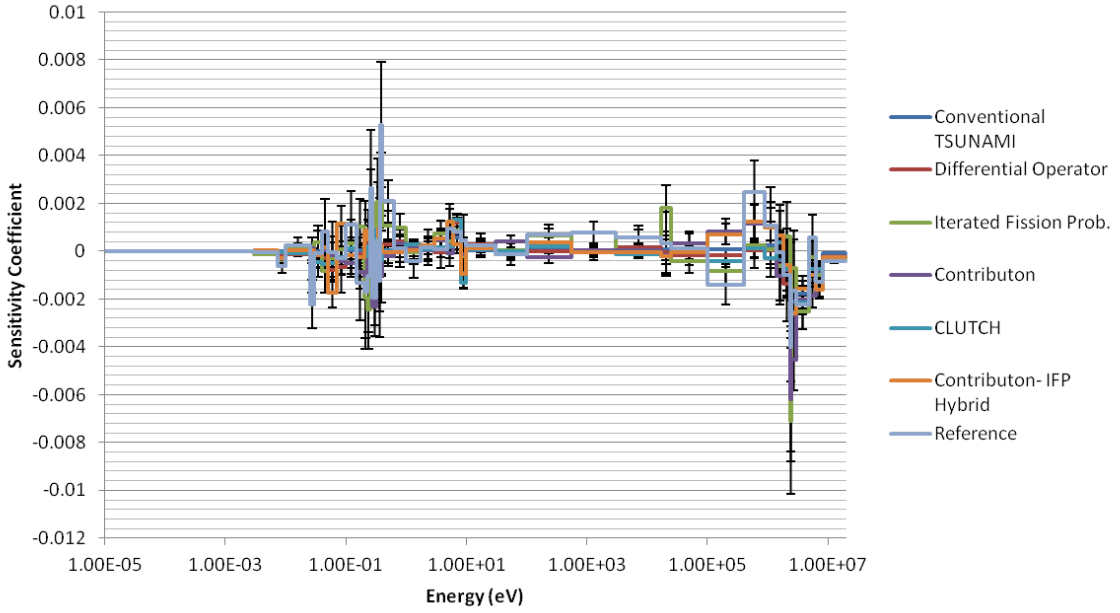

Figure 3.72: PWR clad scatter sensitivity coefficients.

Many of the sensitivity coefficient trends that were seen for the Fuel Pin, MCT, and LCT problems were again seen for the PWR problem. The moderator scatter sensitivity coefficients were largest in the slowing-down energy range because scattering reactions at these energies allow neutrons to escape the U-238 resonance range. Although the clad absorption sensitivity coefficients are all small, the effect of the zirconium absorption resonances between 100 eV and 10 keV can be seen in Figure 3.71. As expected, the fission and $\bar{\nu}$ sensitivities are the largest for the 3.2%-enriched fuel, and the smallest for the 2.2%-enriched fuel. As observed for the Fuel Pin problem, the constrained-chi sensitivity coefficients for the different fuel regions were negative for lower energies and positive for higher energies because of the increase in the fast fission factor seen for neutrons born at faster energies. The maximum and minimum values for the chi sensitivity coefficients is greater for the 2.2% and 2.7% fuel materials because these materials are placed in the center of the core, and fast neutrons born in these materials have a greater chance of causing fast fissions than neutrons born near the edge of the core. The fuel thermal absorption sensitivity coefficients are the largest for the 2.7% fuel, followed by the 2.2% and 3.2% sensitivities; this indicates that removing thermal neutrons from the neutron-starved center of the core has a greater impact on the

eigenvalue than removing neutrons from regions near the reflector or regions with the lowest fuel enrichment.

Although the different sensitivity methods gave sensitivity coefficients that generally agreed well for the PWR problem, significant differences were observed for the conventional TSUNAMI sensitivity coefficients, especially in the thermal energy range. This disagreement may indicate an inadequately-refined flux mesh for the TSUNAMI calculations. The Differential Operator and Contributon-IFP Hybrid methods, which produced noticeable disagreement for the sensitivity coefficients in other problems, generally agreed well with the reference sensitivity coefficients in Figures 3.54 through 3.72. The IFP-10, Contributon, and CLUTCH sensitivity coefficients were again mostly indistinguishable from the reference sensitivity coefficients in the figures. Table 3.17 shows the results of the chi-squared comparison between the calculated and reference sensitivity coefficients for the PWR problem; direct perturbation calculations were not performed for the PWR problem.

Table 3.17: Comparison with the IFP-20 reference case for the PWR problem

	Conven. TSUNAMI	**Diff. Operator**	**IFP-10**	**Contrib.**	**CLUTCH**	**Contrib. -IFP Hybrid**
Norm. $\chi 2$	309.3792	6.8602	0.4800	1.1993	1.4768	3.9515
p-value	0.0000	0.0000	0.9999	0.0001	0.0000	0.0000

As shown in the table, the conventional TSUNAMI, Differential Operator, and Contributon-IFP Hybrid methods once again differed significantly from the reference sensitivity coefficients. While the Contributon and CLUTCH methods produced χ^2 statistics that were close to acceptable χ^2 values, only the IFP-10 sensitivity coefficients showed no statistically-significant difference from the reference sensitivities; the very high p-value produced by the IFP-10 calculation also indicated that the calculation might have been able to use a smaller number of latent generations and still obtain accurate results. The disagreement seen for the Contributon and CLUTCH sensitivity coefficients may have been caused by an inadequate $F^*(r)$ mesh refinement or convergence, but may also be due to difficulties inherent to performing Monte Carlo calculations for very large

systems. Monte Carlo calculations assume that each neutron history is truly independent of all other histories when tallying the mean and variance of parameters in a system, but in truth intergenerational effects exist between neutron histories because the fission sites produced in one generation are used as the source points for the next generation. This introduces an inter-generational bias in the Monte Carlo simulation that can result in the underestimation of the variance for tally parameters; this variance underestimation has been shown by Brown to be as large as a factor of 2 for the PWR problem used in this study, and it is possible that the discrepancies seen for the Contributon and CLUTCH sensitivity coefficients is due to this variance underestimation [21]. This phenomenon may not have affected the IFP-10 sensitivity coefficient calculation because it used the same random number sequence as the reference calculation, whereas the CLUTCH and Contributon calculations did not due to their need to simulate more inactive generations to calculate $F^*(r)$. It should be noted that collapsing the three sets of fuel sensitivity coefficients into one set of sensitivity coefficients for all fuel materials results in acceptable p-values for the Contributon and CLUTCH sensitivity methods. A chi-squared test was used to evaluate the sensitivity coefficients generated for each individual fuel material in the PWR problem, and, as shown in Table 3.18, the 2.7% and 3.2% fuels produced sensitivity coefficients for the CLUTCH calculation that disagreed significantly with the reference sensitivities, whereas the 2.2% fuel sensitivity coefficients agreed well. Brown has shown that the underestimation of tally variances for the PWR problem is greatest near the center and the edge of the PWR core, and the 2.7% and 3.2% fuels contribute greatly to the eigenvalue sensitivity coefficients that are generated in these regions. Thus, it is possible that the disagreement seen for the CLUTCH and Contributon methods is due solely to the underestimation of Monte Carlo tally variances, and that the methods are producing reliable estimates of the sensitivity coefficients for this problem.

Table 3.18: Comparison between CLUTCH and reference fuel sensitivity coefficients for the PWR problem

	2.2%-enriched fuel	**2.7%-enriched fuel**	**3.2%-enriched fuel**
Norm. $\chi 2$	0.9735	1.9229	1.6733
p-value	0.5898	0.0000	0.0000

Figure 3.73 shows the results of the FoM comparison for the 2.2%-enriched and 2.7%-enriched regions, and Figure 3.74 shows the results of the FoM comparison for the 3.2%-enriched fuel, moderator, and clad regions. As shown in the figures, the conventional TSUNAMI and Differential Operator methods gave the largest FoM, followed by the CLUTCH method. The Contributon and Contributon-IFP Hybrid methods performed surprisingly well for the PWR problem, producing FoM that were comparable to or greater than those from the IFP-10 calculation. The difference between the FoM for the CLUTCH and IFP-10 methods was smaller for the PWR problem because the large number of inactive generation required to compute $F^*(r)$ significantly increased the runtime of the CLUTCH calculation, as shown in Table 3.19. The efficiency of the Differential Operator, IFP-10, and CLUTCH methods is expected to improve for continuous-energy simulations because the time used by these methods for data processing should become less significant in light of the runtime increases caused by continuous-energy cross-section lookups, and the IFP-10 method may produce larger FoM for continuous-energy calculations than the CLUTCH method because of the large number of inactive generations used for calculating $F^*(r)$.

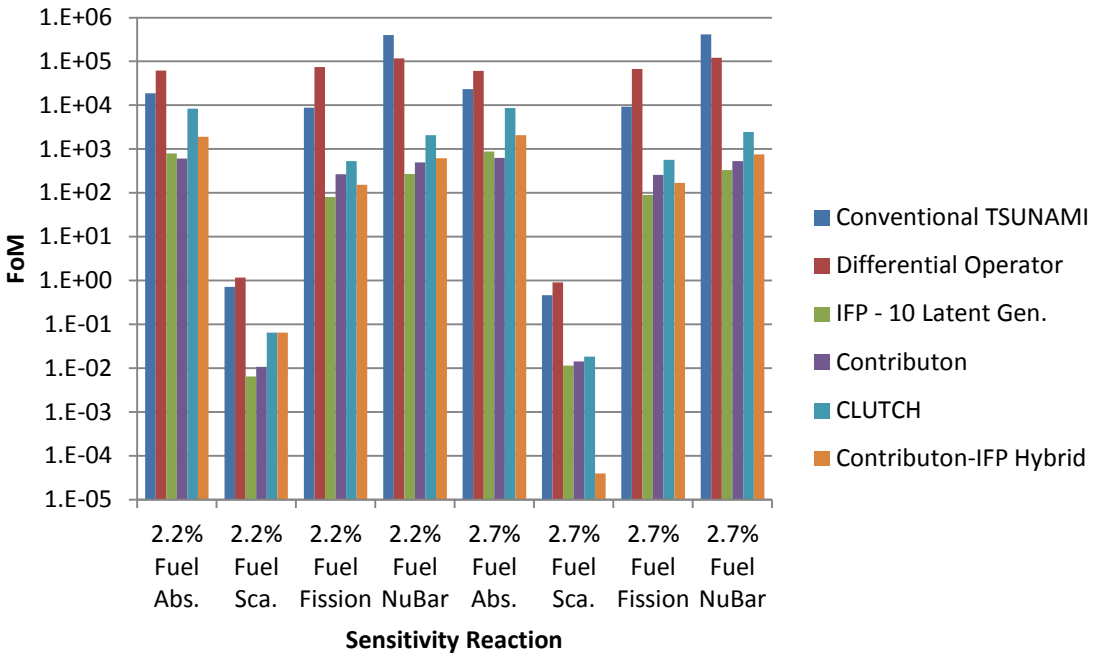

Figure 3.73: Figure of merit comparison for the 2.2%-enriched and 2.7%-enriched fuel in the PWR problem.

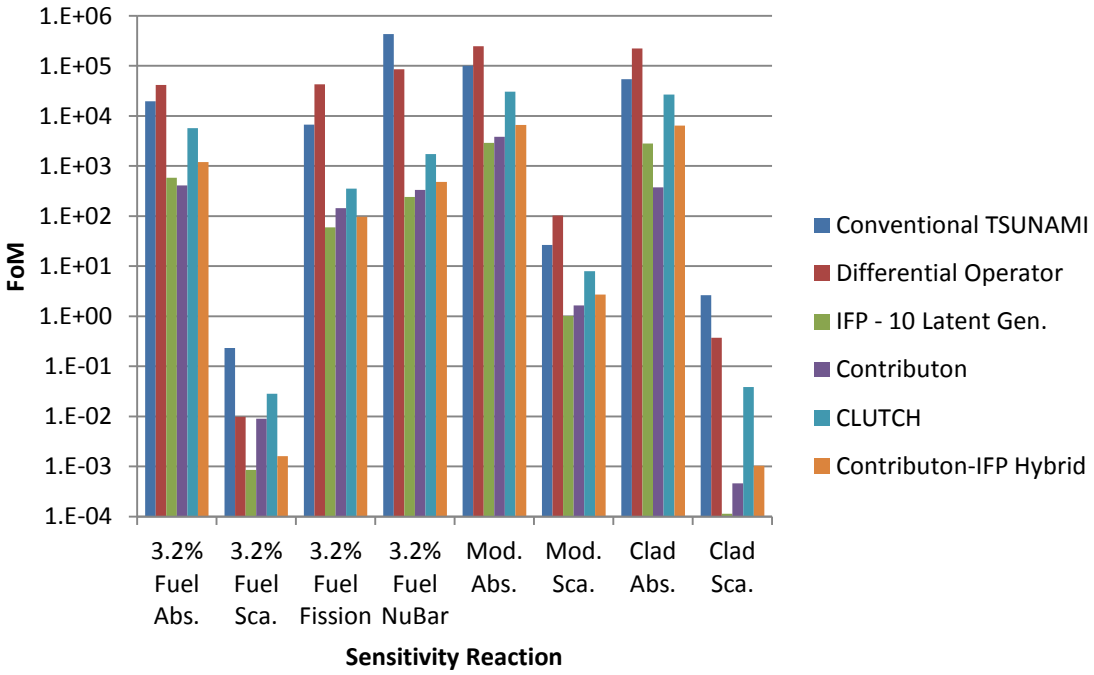

Figure 3.74: Figure of merit comparison for the 3.2%-enriched fuel, moderator, and clad in the PWR problem.

Table 3.19: PWR runtime comparison

	Conven. TSUNAMI	**Diff. Operator**	**IFP-10**	**Contrib.**	**CLUTCH**	**Contrib. -IFP Hybrid**
Runtime (minutes)	146.50	38.32	364.05	522.38	383.63	305.91
Runtime Increase	396.9%	30.0%	1134.8%	---	1201.2%	937.6%

As shown in Table 3.19, the CLUTCH calculation saw a large increase in problem runtime both because of the 10,000 inactive generations required to tally the $F^*(r)$ function, and because the calculations only used 700 active cycles for tallying sensitivity coefficients. This highlights a disadvantage to the Contributon and CLUTCH method: because the methods must generate an accurate $F^*(r)$ mesh before any sensitivity calculations can occur, sensitivity coefficient calculations that use a relatively small number of active generations produce sensitivity coefficients with low FoM. The ability to save a previously-converged $F^*(r)$ mesh from a problem and use it for future calculations could dramatically raise the FoM for these methods when performing repeated sensitivity coefficient calculations on models of the same system.

3.7 Sensitivity Method Memory Comparison

The memory usage for each Shift sensitivity coefficient calculation was estimated using the "top" command while the calculation was running, and the set of these memory requirements for each problem given in Table 3.20.

Table 3.20: Shift sensitivity calculation memory requirements

Model	Diff. Operator	IFP	Contrib.	CLUTCH	Contrib.-IFP Hybrid
Fuel Pin	49 MB	216 MB	15 MB	49 MB	15 MB
Godiva	48 MB	170 MB	16 MB	49 MB	16 MB
MCT	58 MB	613 MB	17 MB	58 MB	16 MB
PST	50 MB	305 MB	17 MB	52 MB	16 MB
LCT	58 MB	721 MB	18 MB	58 MB	17 MB
PWR	67 MB	1600 MB	20 MB	69 MB	17 MB

As shown in Table 3.20, the IFP calculations always required the largest amount of memory because these calculations stored reaction rates for every particle history for several generations before obtaining a sensitivity tally for that initial particle. As mentioned previously, the Contributon and Contributon-IFP Hybrid calculations showed the smallest memory requirements because they require almost no data storage to calculate the importance of an event, and instead simulate secondary particles at the site of the event. The Differential Operator and CLUTCH calculations required more memory than the Contributon and Contributon-IFP Hybrid calculations because they stored reaction rate information for each collision seen by a particle, but required significantly less memory than the IFP calculations because this memory was freed after each particle history ended. The memory requirements of the Contributon and CLUTCH methods are very similar to those of the Differential Operator and Contributon-IFP Hybrid methods, respectively, and the small (~1 MB) increase in the memory requirements for the Contributon and CLUTCH methods is due to the $F^*(r)$ spatial mesh used by these methods for tallying the importance of events. The fact that the memory increase caused by this $F^*(r)$ mesh is small is promising for these methods because it confirms that the $F^*(r)$ mesh does not require a large amount of memory.

Real-world sensitivity coefficient calculations will require substantially more memory than the calculations shown in Table 3.20. TSUNAMI-3D currently tracks sensitivity coefficients for 12 different neutron reactions instead of the 5 accounted for in

this study; furthermore, all of these sensitivity coefficient calculations calculated macroscopic region sensitivity coefficients, and calculating isotopic-dependent sensitivity coefficients will increase the memory requirements for each region sensitivity by a factor equal to the number of isotopes in that region. A more detailed sensitivity coefficient calculation could require isotopic-dependent sensitivity coefficients for 12 different reactions in a problem, and could easily contain 10 isotopes per region. These sorts of problems could easily push the IFP memory requirements, which were on the order of 0.1 to 1.0 GB per calculation, into the range of 10's to 100's of GB. The CLUTCH method's memory requirements should be sufficient for most problems, and the Contributon and Contributon-IFP Hybrid methods may be necessary to address the memory requirements of the most detailed problems.

3.8 Comparison of Constrained-Chi Sensitivity Methods

The approaches taken by Nagaya and Perfetti for calculating constrained-chi sensitivity coefficients presented in chapter 2.1.2 were both used to calculate constrained-chi sensitivity coefficients for the test problems, which were compared with sensitivity coefficients produced from direct perturbation calculations. This comparison was only performed for the Fuel Pin, Godiva, MCT, and PST problems because direct perturbations were not performed for the LCT or PWR problems. A chi-squared test was used to compare the sensitivities produced using each of the constrained-chi approaches using the IFP-20 calculations and direct perturbation calculations, and the results of this comparison are given in Table 3.21. The comparison in Table 3.21 grouped all of the chi sensitivities together for the different approaches and did not distinguish between chi sensitivities generated from different problems; the term "Count" in Table 3.21 refers to the number of sensitivity coefficients that met the criteria for comparison described earlier in this chapter.

Table 3.20: Constrained chi approach evaluation

	Perfetti's Constrained-Chi	**Nagaya's Constrained-Chi**
Count	2	5
χ^2	15.41809	685.0453
p-value	0.0000	0.0000

As shown in the Table, this comparison did not produce conclusive results because of the small number of reliable sensitivity coefficients generated using the direct perturbation method. Unfortunately, the majority of the chi sensitivity coefficients were very small and it was difficult for the direct perturbation methods to generate reliable sensitivity coefficients to compare with the IFP-20 constrained-chi sensitivity coefficients. In fact, only the Godiva and PST problems generated direct perturbation constrained-chi sensitivity coefficients with R^2 values greater than 0.90. Although both approaches for calculating the constrained-chi sensitivity coefficients gave p-values that were close to zero and the number of comparable sensitivity coefficients was very low, Perfetti's constrained-chi approach produced a much smaller χ^2 statistic than Nagaya's approach. The results presented here are not sufficient to comment on the accuracy of Perfetti's or Nagaya's approaches, and further studies should be performed to more thoroughly evaluate the two approaches. Because the difference between the constrained-chi sensitivity coefficients produced by the two approaches is inversely proportional to $1-\chi(E_i)$, future studies may need to perform few-group calculations to observe differences that are verifiable using direct perturbation calculations.

3.9 Optimizing the Iterated Fission Probability Process

The accuracy and efficiency of IFP sensitivity coefficient calculations is strongly dependent on the number of latent generations used before tallying the asymptotic population of neutrons created by a progenitor neutron; using a larger number of latent generations gives a more accurate estimate of the true importance of the original neutron, but also lowers the efficiency of the calculation because fission chains need to survive for a longer number of generations before contributing to the sensitivity coefficient tallies.

The number of latent generations used in the IFP calculations was varied to determine the minimum number of latent generations required to produce accurate sensitivity coefficient estimates for the problems described earlier in this chapter. IFP calculations were performed using either 2, 5, 10, or 15 latent generations, and chi-squared tests were used to compare the accuracy of the sensitivity coefficients from these calculations with those from the reference IFP-20 calculation. Table 3.22 shows the result of this comparison, and the IFP cases that were determined to produce accurate sensitivity coefficients using a minimum number of latent generations are highlighted in bold in the table.

Table 3.21: Iterated Fission Probability latent generation comparison

		IFP-2	**IFP-5**	**IFP-10**	**IFP-15**
Fuel Pin	Norm. χ^2	**0.7062**	0.5967	0.3371	0.1532
	p-value	**0.9999**	0.9999	0.9999	0.9999
Godiva	Norm. χ^2	**0.8372**	0.7173	0.3808	0.1768
	p-value	**0.8437**	0.9693	0.9999	0.9999
MCT	Norm. χ^2	1.0968	**0.6885**	0.4234	0.2024
	p-value	0.1074	**0.9999**	0.9999	0.9999
PST	Norm. χ^2	1.0884	**1.0748**	0.9757	1.0231
	p-value	0.1484	**0.1847**	0.6029	0.3813
LCT	Norm. χ^2	**0.7448**	0.5077	0.2964	0.1823
	p-value	**0.9999**	0.9999	0.9999	0.9999

As shown in Table 3.22, IFP calculations needed no more than 5 latent generations for the test problems examined in this chapter; in fact, the MCT and PST calculations could have used 2 latent generations and obtained accurate sensitivity coefficients, but instead used 5 latent generations to be conservative. Although the dominance ratio was not calculated for the problems examined in Table 3.22, most of the problems contained about one assembly of fuel, and were not the same scale as a full-core PWR or HTGR model. It is possible that calculations for more-complex systems

will require more latent generations, but the PWR challenge problem presented in chapter 3.6 produced very accurate sensitivity coefficients using 10 latent generations.

Chapter IV

Determining the $F^*(r)$ Importance Weighting Function for Contributon-Based Methods

This chapter discusses the calculation of the $F^*(r)$ weighting function that is used by the Contributon and CLUTCH methods for calculating eigenvalue sensitivity coefficients, as well as the necessary level of accuracy in the $F^*(r)$ function for accurately calculating sensitivity coefficients. The $F^*(r)$ function, originally given in Equation 2.69, is defined as

$$F^*(r) = \int_E \int_\Omega \frac{\chi(r,E)}{4\pi}\, \phi^*(r,E,\Omega) d\Omega dE \,, \tag{4.1}$$

and describes the average importance generated by a fission neutron born at location r. The function is used to weight the fission neutron production tally for a particle to give an estimate of the importance of the particle, as described in Equation 2.67 for the Contributon and CLUTCH methods. Currently TSUNAMI-3D has the capability to calculate eigenvalues sensitivity coefficients using the Contributon method with the assumption that $F^*(r) = 1$ everywhere, which implies that the importance of a neutron can be determined by tallying the number of fission neutrons that are created after an interaction of interest and that the future multiplication of these fission neutrons does not affect the importance of the original neutron [1]. This assumption will be shown to

produce poor estimates for sensitivity coefficients in systems with large adjoint flux gradients or multigenerational effects, and it is desirable to develop a more rigorous methodology for calculating $F^*(r)$ as the next generation of sensitivity coefficient calculation methods is developed.

Using the $F^*(r)$ function to calculate the importance of particles may seem like an iterative process, or even like pulling oneself up by one's bootstraps, because the adjoint flux is needed to calculate $F^*(r)$, which is then used to calculate the importance of a neutron. The approaches for calculating $F^*(r)$ that are presented in this chapter use one of two alternative methods for calculating the importance of neutrons, the Differential Operator method or the Iterated Fission Probability method, to tally $F^*(r)$ during inactive neutron generations and then pass the function to Contributon-based methods to calculate sensitivity coefficients during active generations. Future approaches for calculating $F^*(r)$ will likely include calculating $F^*(r)$ using a deterministic Denovo calculation and passing the results to Shift before the sensitivity coefficient calculation begins.

The Differential Operator- and IFP-based approaches for calculating $F^*(r)$ that were developed during the course of this research rely on the definition of the unconstrained chi sensitivity coefficient, which is given by

$$S_{k,\chi}(r) = \frac{1}{D}\frac{1}{k}\int_0^\infty \int_{4\pi} \bar{\upsilon}\Sigma_f(r,E)\phi(r,E,\Omega)d\Omega dE \int_0^\infty \int_{4\pi} \frac{\chi(r,E')}{4\pi}\, \phi^*(r,E',\Omega')d\Omega' dE', \tag{4.2}$$

where D is the adjoint-weighted fission source of a system, as described in Equation 2.14. The right-most integral term in Equation 4.2 is by definition $F^*(r)$, and Equation 4.2 can be rewritten as

$$F^*(r) = \frac{D \cdot S_{k,\chi}(r)}{\int_0^\infty \int_{4\pi} \frac{\bar{\upsilon}\Sigma_f(r,E)\phi(r,E,\Omega)}{k} d\Omega dE}. \tag{4.3}$$

Note that the numerator in Equation 4.3 reduces to the numerator of Equation 2.10 for chi sensitivity coefficients and that calculating D is not required for calculating $F^*(r)$. The denominator in Equation 4.3 represents the total number, or total weight, of neutrons born within r. The Differential Operator and IFP approaches for calculating $F^*(r)$ use the Differential Operator and IFP methods, respectively, to calculate the unconstrained chi sensitivity coefficient in the numerator in Equation 4.3 and divide that term by the total weight of neutrons born within r to obtain estimates for $F^*(r)$. The Differential Operator approach calculates the unconstrained chi sensitivity in Equation 2.10 for a particle born at a location by tallying the total number of fission neutrons created by that neutron from birth until death. The Iterated Fission Probability approach tallies the unconstrained chi sensitivity for the neutron in a similar manner, except that it waits for a number of latent generations to tally the asymptotic population created by the initial neutron.

Because $F^*(r)$ is defined as the importance created *per* neutron born within r, tallying $F^*(r)$ does not require the Monte Carlo fission source to be converged for accurate results, which allows $F^*(r)$ tallies to begin during inactive neutron histories. Although the Contributon and CLUTCH methods do not themselves require a spatial mesh for tallying sensitivity coefficients, a spatial mesh is currently used for storing and tallying the $F^*(r)$ function. The lack of energy, angular, and isotopic dependence in the $F^*(r)$ term results in small memory requirements for storing the function compared to the memory requirements of a conventional TSUNAMI flux mesh; an $F^*(r)$ mesh that is as refined as the conventional TSUNAMI mesh in Equation 2.44 requires 32 megabytes of memory as opposed to 182.8 gigabytes of memory. However, because the chi sensitivity coefficients, and thus $F^*(r)$, are by definition equal to zero for non-fissionable cells, the $F^*(r)$ mesh needs to cover only the fissionable regions in a problem, which further reduces the memory requirements of the $F^*(r)$ mesh. The IFP approach for calculating $F^*(r)$ requires far less memory than is required for conventional IFP sensitivity coefficient calculations because it only stores an integer "tag" signifying the mesh cell location where each progenitor neutron was born and does not store reaction rate tallies for the entire system for each progenitor. An IFP calculation for $F^*(r)$ that has the same number of neutron histories per generation and latent generations as the IFP sensitivity coefficient calculation in Equation 2.64 and is as refined as the conventional TSUNAMI

mesh in Equation 2.44 requires 0.84 megabytes of memory instead of the 33,707.5 gigabytes of memory needed by the conventional IFP method. Future approaches for calculating $F^*(r)$ may completely eliminate the need for a mesh-based spatial discretization of $F^*(r)$ by using Kernel Density Estimators (KDE) to represent $F^*(r)$ using functions that are not stored on a mesh but are instead continuous in space [24].

4.1 Procedure for Calculating $F^*(r)$

This subchapter describes the procedure used for determining the necessary refinement and convergence for a $F^*(r)$ mesh in Contributon-based calculations. The reference sensitivity coefficients used to evaluate the accuracy of a given mesh were generated by an Iterated Fission Probability sensitivity coefficient calculation. The Iterated Fission Probability method was chosen because it is an adjoint-weighted method for obtaining sensitivity coefficients and because it contains the fewest assumptions of the sensitivity coefficient methods in this study. The only fundamental assumption of the Iterated Fission Probability method is that the asymptotic population of neutrons produced by a progenitor neutron is reached after some number of latent generations; 20 latent generations has been shown to be a very conservative number of latent generations for obtaining accurate Iterated Fission Probability sensitivities, and thus 20 latent generations were used for the reference calculations in this study [5]. Furthermore, the statistical uncertainties for the sensitivity coefficients that were obtained using the Iterated Fission Probability method were generally several orders of magnitude smaller than the uncertainties that would be obtained from a similar direct perturbation calculation, which resulted in an even more rigorous evaluation of the experimental calculations.

Each realization of the $F^*(r)$ mesh was evaluated by calculating the difference, in terms of the number of effective standard deviations, between each experimental and reference sensitivity coefficient, calculating a sum of squares for these differences, and applying a chi-squared test to give a p-value for the equivalence of the two simulations. Because Shift gave sensitivity coefficients to six significant figures after the decimal point, an uncertainty of 5.0e-7 was added to the uncertainty for the sensitivity coefficients

when calculating their effective standard deviation. Only sensitivity coefficients that were greater than 1.0e-5 were used to calculate the chi-squared statistic; this was done to both further reduce the impact of the Shift round-off error and also because the very small sensitivities tended to have large uncertainties. Monte Carlo uncertainty estimates are only accurate for tallies with sufficiently converged mean and variance estimates, and sensitivity coefficients with large uncertainties may not have accurate statistical uncertainty estimates.

The procedure used for calculating an adequate $F^*(r)$ mesh for any problem is given below:

1. The problem of interest is first simulated using an $F^*(r)$ function that is equal to 1 everywhere. The results from this simulation are compared to the reference sensitivity coefficients, which are generated using an IFP sensitivity coefficient calculation with 20 latent generations, to determine if an $F^*(r)$ mesh is needed for Contributon-based calculations.
2. The problem is next simulated using different $F^*(r)$ spatial refinements to determine the necessary level of spatial refinement for the mesh. This step is performed for both the Differential Operator and Iterated Fission Probability approaches for calculating the $F^*(r)$ mesh to determine which approach is appropriate for the problem. The Differential Operator approach is generally adequate for simple problems, while the Iterated Fission Probability approach is needed for more-complex problems. The Iterated Fission Probability $F^*(r)$ calculations in this comparison used 20 latent generations to ensure that the comparisons were free from the effects of using an insufficient number of latent generations. These simulations tally the $F^*(r)$ mesh over a large number, typically 10,000, inactive neutron generations to ensure that mesh convergence was not a factor in the comparison; unfortunately, simulating 10,000 inactive generations was often not enough to remove all effects of mesh convergence from the spatial refinement comparison, and moving to a finer mesh sometimes resulted in worse sensitivity coefficient agreement.

3. If the Iterated Fission Probability approach is chosen in Step 2 then the number of latent generations used by this approach is varied to determine the necessary number of latent generations to obtain a sufficiently-accurate $F^*(r)$ mesh.
4. The necessary level of $F^*(r)$ mesh convergence is determined by varying the number of inactive generations over which the $F^*(r)$ mesh is tallied.

4.2 The Necessity of an $F^*(r)$ Mesh

Each of the sample problems from Chapter 3 was simulated using the CLUTCH sensitivity method with an $F^*(r)$ mesh that was equal to one everywhere and was compared with a reference Iterated Fission Probability calculation with 20 latent generations. Chi-squared test statistics were calculated for each of the problems and used to give a p-value comparing each calculation with the reference calculation; these values are given in Table 4.1. Table 4.1 also gives the number of sensitivity coefficients that met the criteria given in subchapter 4.1 to be used in this comparison. As shown in Table 4.1, calculating an $F^*(r)$ mesh is necessary for all problems except for the Fuel Pin model. Indeed, the infinitely-reflected nature of the Fuel Pin model causes the adjoint flux to vary by a very small amount through model, whereas spatial effects force the other cases to calculate a spatially-dependent $F^*(r)$ mesh.

Table 4.1: CLUTCH sensitivity coefficient accuracy for problems with $F^*(r) = 1$

Model	Normalized χ^2 Statistic	p-value
Fuel Pin	0.7831	0.9964
Godiva	14.1381	0.0000
MCT	30.6821	0.0000
PST	12.7323	0.0000
PWR	22.0657	0.0000
LCT	19.2849	0.0000

4.3 $F^*(r)$ Mesh Refinement

A mesh refinement study was not performed for the Fuel Pin model because it produced accurate sensitivity coefficient estimates with an $F^*(r)$ mesh equal to one everywhere. In order to determine the necessary spatial refinement for the Godiva $F^*(r)$ mesh, CLUTCH simulations were formed using 10,000 latent generations and various mesh refinements. All calculations for the Godiva model used 10,000 active neutron generations containing 5,000 active histories each. These calculations were performed using both the Differential Operator and Iterated Fission Probability approaches for determining $F^*(r)$, and Table 4.2 gives the normalized χ^2 value and p-value for each mesh realization of the $F^*(r)$ mesh. Four different mesh refinements were examined for the Godiva problem: a 3×3×3 mesh, a 10×10×10 mesh, a 25×25×25 mesh, and a 50×50×50 mesh. These refinements correspond to mesh widths of about 2.91cm, 0.87 cm, 0.35 cm, and 0.17 cm, respectively.

Table 4.2: Godiva $F^*(r)$ mesh refinement results

		3×3×3 Mesh	**10×10×10 Mesh**	**25×25×25 Mesh**	**50×50×50 Mesh**
Differential Operator Approach	Norm. $\chi2$	1.4787	**0.9902**	0.9999	1.0047
	p-value	0.0044	**0.5021**	0.4784	0.4668
Iterated Fission Probability Approach	Norm. $\chi2$	1.3089	1.0089	1.0545	1.0709
	p-value	0.0376	0.4566	0.3512	0.3161

As shown in bold in Table 4.2, a 10×10×10, or 0.87 cm, mesh gave a sufficiently-refined $F^*(r)$ mesh for the Godiva problem, and moving to a more highly refined mesh resulted in no improvement in sensitivity coefficient accuracy. In fact, the simulations with finer $F^*(r)$ meshes produced slightly smaller p-values than the 10×10×10 mesh, likely because the finer meshes contain more mesh intervals, which resulted in each interval receiving fewer $F^*(r)$ tallies per mesh interval and thus produced larger $F^*(r)$ uncertainties. The Differential Operator and Iterated Fission Probability approaches for calculating $F^*(r)$ both produced accurate sensitivity coefficients for the Godiva model, and the Differential

Operator approach was selected for all other CLUTCH calculations using the Godiva model.

Next, the necessary spatial refinement for the $F^*(r)$ mesh in the MCT model was determined. All calculations for the MCT model used 10,000 inactive and 1,400 active generations with 5,000 neutron histories each. The X-Y mesh refinements examined in this study placed either four, one, or one-quarter MCT fuel pins within each $F^*(r)$ mesh interval, which correspond to mesh intervals of about 3.81 cm, 1.90 cm, and 0.95 cm, respectively. The Z mesh refinements used 20, 40, or 80 mesh axial intervals across the fuel region, which correspond to mesh widths of about 4.78 cm, 2.39 cm, and 1.19 cm, respectively. Chi-squared calculations were performed on the sensitivity coefficients produced by each of the mesh refinements, and are given in Tables 4.3 for both the Differential Operator and Iterated Fission Probability approaches for calculating $F^*(r)$.

Table 4.3: MCT $F^*(r)$ mesh refinement results

		Differential Operator Approach			**Iterated Fission Probability Approach**		
		4 pins per mesh	1 pin per mesh	0.25 pins per mesh	4 pins per mesh	1 pin per mesh	0.25 pins per mesh
20 Z Intervals	Norm. $\chi 2$	9.5130	6.5531	6.4706	1.8871	1.0698	1.0779
	p-value	0.0000	0.0000	0.0000	0.0000	0.1767	0.1510
40 Z Intervals	Norm. $\chi 2$	9.4534	6.4377	6.3466	1.8555	**1.0507**	1.0508
	p-value	0.0000	0.0000	0.0000	0.0000	**0.2463**	0.2461
80 Z Intervals	Norm. $\chi 2$	30.6821	6.3842	6.3005	1.8513	1.0472	1.0641
	p-value	0.0000	0.0000	0.0000	0.0000	0.2607	0.1956

As shown in Table 4.3, the Differential Operator approach for calculating $F^*(r)$ did not perform well for the MCT problem, producing p-values that were all close to zero. Although the Differential Operator approach performed well for the Godiva model, the increasingly complex nature of the MCT system requires $F^*(r)$ calculations using the more rigorous Iterated Fission Probability approach. The results in Table 4.3 indicate that CLUTCH sensitivity coefficient calculations for the MCT problem require at least

one $F^*(r)$ mesh interval per fuel pin cell and at least 20 axial meshes; a mesh with this level of refinement has mesh interval widths of 1.90 cm, 1.90 cm, and 4.78 cm in the X-, Y-, and Z-dimensions, respectively. As was observed for the Godiva model, moving to a more refined mesh does not always result in more accurate sensitivity coefficients because a finer mesh receives fewer tallies for $F^*(r)$ in each mesh interval, and thus produces $F^*(r)$ estimates with greater uncertainty. A mesh refinement with 1 pin per X-Y mesh interval and 40 Z intervals, shown in bold in Table 4.3, was selected for all other MCT model CLUTCH calculations because the large increase in χ^2 seen when moving from 20 to 40 Z intervals allows for more flexibility when varying the number of IFP latent generations and the number of inactive generations in simulations, as performed in Chapters 4.4 and 4.5.

The necessary spatial refinement for the $F^*(r)$ mesh in the PST model was determined by performing simulations with 10,000 inactive and 1,600 active generations, each containing 5,000 neutron histories. The mesh refinements examined for the PST model placed 8, 16, or 32 mesh intervals in the X and Y dimensions for each fuel cylinder, and 4, 8, or 16 mesh intervals in the Z dimension; these refinements correspond to mesh widths of about 3.67 cm, 1.84 cm, and 0.92 cm, respectively, and 6.73 cm, 3.36 cm, and 1.68 cm, respectively. Table 4.4 gives the results of the sensitivity coefficient calculations for each mesh refinement for both the Differential Operator and Iterated Fission Probability approaches.

Table 4.4: PST $F^*(r)$ mesh refinement results

		Differential Operator Approach			**Iterated Fission Probability Approach**		
		3.67 cm XY Mesh	1.84 cm XY Mesh	0.92 cm XY Mesh	3.67 cm XY Mesh	1.84 cm XY Mesh	0.92 cm XY Mesh
4 Z Intervals	Norm. χ^2	2.9511	3.3475	3.1008	2.2097	1.7664	1.6225
	p-value	0.0000	0.0000	0.0000	0.0000	0.0000	0.0000
8 Z Intervals	Norm. χ^2	2.4677	2.4106	1.8859	1.5173	1.1968	3.0761
	p-value	0.0000	0.0000	0.0000	0.0000	0.0131	0.0000
16 Z Intervals	Norm. χ^2	6.9754	1.7037	1.5795	1.2546	**1.0638**	2.1932
	p-value	0.0000	0.0000	0.0000	0.0023	**0.2212**	0.0000

As shown in Table 4.4, obtaining a sufficiently refined $F^*(r)$ mesh was difficult for the PST problem. The Differential Operator approach again produced poor estimations of the sensitivity coefficients, and only one of the Iterated Fission Probability approach mesh refinements produced a reasonable p-value. This mesh refinement, which used 16 mesh intervals in the X-, Y-, and Z-dimensions and resulted in mesh interval widths of 1.84 cm, 1.84 cm, and 1.68 cm, is shown in bold in Table 4.4 and was used for all other PST model CLUTCH calculations. The difficulty seen here in obtaining a sufficiently refined $F^*(r)$ mesh makes the PST problem an ideal case for using Kernel Density Estimators for tallying $F^*(r)$. Unlike most of the other problems, the PST problem does not contain a large number of fuel pins, but instead 4 large cylinders containing a Plutonium solution. A KDE approach could generate a continuous function describing $F^*(r)$ over each cylinder, and would reduce the difficulty in calculating a spatially-dependent $F^*(r)$ for this problem.

Next, the necessary $F^*(r)$ refinement for the LCT problem was determined. The mesh realizations examined for this case used either 4 or 1 pins per mesh in the X- and Y-dimensions, and 15, 30, or 60 meshes in the Z-dimension. These mesh refinements corresponded to X and Y mesh widths of 2.60 cm and 1.30 cm, respectively, and to Z mesh widths of 6.00 cm, 3.00 cm, and 1.50 cm, respectively. Sensitivity coefficients were calculated using each of these mesh refinements for both the Differential Operator

and Iterated Fission Probability approaches, and the results of these calculations are given in Table 4.5. Each simulation in Table 4.5 was performed using 10,000 inactive and 1,000 active generations, each containing 5,000 neutron histories.

Table 4.5: LCT $F^*(r)$ mesh refinement results

		Differential Operator Approach		**Iterated Fission Probability Approach**	
		4 pins per mesh	1 pin per mesh	4 pins per mesh	1 pin per mesh
15 Z Intervals	Norm. χ^2	6.7704	6.2087	**0.9041**	0.9315
	p-value	0.0000	0.0000	**0.9286**	0.8486
30 Z Intervals	Norm. χ^2	6.4323	5.8722	0.8672	0.8964
	p-value	0.0000	0.0000	0.9802	0.9439
60 Z Intervals	Norm. χ^2	6.3471	5.7668	0.8564	0.8954
	p-value	0.0000	0.0000	0.9873	0.9461

As shown in Table 4.5, the Differential Operator approach was again not sufficient for producing an accurate $F^*(r)$ mesh, whereas the Iterated Fission Probability approach performed well. Each of the mesh refinements examined resulted in a good estimate of the sensitivity coefficients for this problem, and the case with the largest mesh interval, which contained 4 fuel pins in each X-Y mesh and used 15 axial meshes, was selected as the mesh for all other CLUTCH calculations and is shown in bold in Table 4.5. The dimensions for this mesh were 2.60 cm, 2.60 cm, and 6.00 cm in the X-, Y-, and Z-dimensions, respectively. In other problems the necessary $F^*(r)$ mesh refinement was typically about 1 cm^3, and the acceptable mesh refinement for the LCT problem was significantly larger than this trending size; in fact, the slight difference seen in Chapter 3 for the samarium solution sensitivity coefficients suggests that this problem might have required a smaller $F^*(r)$ mesh refinement near the samarium hole in the center of the assembly.

4.4 Determining the Necessary Number of Latent Generations when Calculating $F^*(r)$

After determining the necessary level of $F^*(r)$ refinement for obtaining accurate sensitivity coefficient estimates, the necessary number of latent generations for the Iterated Fission Probability approach for calculating $F^*(r)$ was investigated. This investigation surveyed only the cases that used the Iterated Fission Probability approach for calculating $F^*(r)$, and did not examine the Godiva and Fuel Pin models because they used the Differential Operator and $F^*(r)$ = 1 approaches, respectively. To perform this investigation, a CLUTCH simulation was performed for each problem using the Iterated Fission Probability approach for calculating $F^*(r)$ with 2, 5, 10, 15, or 20 latent generations. The sensitivity coefficients produced by these simulations were compared with sensitivity coefficients produced by a reference Iterated Fission Probability sensitivity coefficient calculation with 20 latent generations. Each simulation used 10,000 latent generations for tallying $F^*(r)$, 5,000 neutron histories per generation, and used the same number of active generations as was given in the previous subchapter.

Table 4.6: Number of latent generations for calculating $F^*(r)$ study results

		Number of Latent Generations				
		2	5	10	15	20
MCT	Norm. $\chi 2$	1.4833	1.0854	**1.0552**	1.0520	1.0509
	p-value	0.0000	0.1304	**0.2286**	0.2411	0.2456
PST	Norm. $\chi 2$	1.0667	**1.0410**	1.0555	1.0600	1.0638
	p-value	0.2125	**0.3066**	0.2509	0.2351	0.2221
LCT	Norm. $\chi 2$	1.8779	1.3576	**0.9591**	0.9124	0.9041
	p-value	0.0000	0.0000	**0.7269**	0.9087	0.9286

Table 4.6 gives the chi-square test results from the CLUTCH Iterated Fission Probability approach simulations with various numbers of latent generations. As shown in bold in Table 4.6, the MCT, PST, and LCT problems required IFP-based $F^*(r)$ calculations using 10, 5, and 10 latent generations, respectively. For comparison, the

normal Iterated Fission Probability sensitivity coefficient calculations for these problems required 5, 5, and 2 latent generations, respectively, as given in Table 3.22. This is not to say that the CLUTCH simulations with a smaller number of latent generations produced poor estimates for $F^*(r)$, or that more latent generations are somehow required for calculating $F^*(r)$ than when directly calculating sensitivity coefficients. These CLUTCH IFP-approach simulations required more latent generations than normal IFP calculations because the contribution to χ^2 from an imperfect $F^*(r)$ spatial mesh refinement, resulted in lower overall p-values before the effect of varying the number of latent generations was examined.

4.5 $F^*(r)$ Mesh Convergence

The last step in obtaining a sufficient $F^*(r)$ mesh for performing CLUTCH and Contributon calculations was determining the necessary mesh convergence and the necessary number of inactive generations needed for generating $F^*(r)$ to produce accurate sensitivity coefficients. Because the tallies that generate the $F^*(r)$ mesh occur during the inactive neutron generations, the total number of inactive generations was varied and its effect on the sensitivity coefficients was examined. The number of inactive generations examined in this study includes 50, 200, 500, 1,000, 2,000, 5,000, and 10,000 generations. Table 4.7 shows the chi-squared statistics produced for sensitivity calculations using these numbers of skipped generations, as well as the average mesh cell uncertainty and the average number of neutron histories born in each mesh cell containing fissionable material. Table 4.7 does not give data for the Fuel Pin problem because it did not require an $F^*(r)$ mesh to obtain accurate sensitivity coefficients. The number of inactive generations deemed necessary for each problem is shown in bold in Table 4.7.

Table 4.7: $F^*(r)$ mesh convergence study results

		Number of Inactive Generations						
		50	200	500	1,000	2,000	5,000	10,000
Godiva	Norm. χ^2	1.0004	**0.8959**	0.8071	0.8389	0.8188	0.8507	0.9903
	p-value	0.4772	**0.7279**	0.8872	0.8389	0.8705	0.8182	0.5021
	Histories per cell	428.8	**1644.7**	4065.0	8064.5	15923.6	39557.0	79113.9
	Average mesh unc.	32.98%	**20.22%**	14.30%	11.20%	9.78%	7.33%	5.34%
MCT	Norm. χ^2	1.4607	0.9748	**1.0717**	1.0483	1.0733	1.1619	1.0997
	p-value	0.0000	0.6226	**0.1699**	0.2551	0.1653	0.0191	0.0959
	Histories per cell	38.7	154.3	**385.8**	771.6	1543.2	3858.0	7716.0
	Average mesh unc.	58.60%	27.08%	**16.92%**	11.93%	8.42%	5.33%	3.77%
PST	Norm. χ^2	1.0303	**1.0867**	1.1101	1.0903	1.0564	1.0536	1.0410
	p-value	0.3508	**0.1542**	0.0999	0.1436	0.249	0.2583	0.2509
	Histories per mesh	29.0	**84.0**	193.7	374.7	733.6	1796.6	3557.5
	Average mesh unc.	75.05%	**48.22%**	35.47%	27.84%	21.67%	15.54%	12.03%
LCT	Norm. χ^2	1.1084	0.8698	**0.9740**	0.9559	0.9594	1.0046	0.9591
	p-value	0.0542	0.9785	**0.6455**	0.7431	0.7262	0.4635	0.7269
	Histories per cell	117.5	441.5	**1084.6**	2141.3	4224.8	10442.8	20859.4
	Average mesh unc.	36.28%	19.25%	**13.47%**	10.62%	8.69%	6.20%	4.43%

As shown in Table 4.7, none of the problems required more than 500 inactive generations for generating an $F^*(r)$ mesh, which corresponded to simulating approximately 1,000 inactive neutron histories per each $F^*(r)$ interval containing fissionable material. These results are promising because requiring simulations to use 500 inactive generations instead of the 200 typically required for fission source convergence typically will not

result in a large increase in problem runtime. Although 50 inactive generations would have sufficed for the Godiva problem, using 200 generations was done to guarantee fission source convergence. The p-values in Table 4.7 for several of the problems, including the MCT and LCT problems, increase dramatically when using 200 inactive generations instead of 500 inactive generations; the reason for this behavior is not clear because using a more poorly-converged $F^*(r)$ mesh should result in poorer estimates for the sensitivity coefficients in a problem. Although it is possible that these non-intuitive results occur because the error introduced by using a more coarse mesh cancel out, or that these fluctuations in the p-values are not statistically significant, or that the cases with 200 inactive generations experienced larger p-values because they saw the same random number sequence as the reference calculation, the cases that gave non-intuitive results for 200 inactive generations were not selected for calculating $F^*(r)$, and these cases instead used 500 inactive generations.

The results in Table 4.7 also indicate that an adequate $F^*(r)$ mesh does not have a strict mesh convergence criterion, and it was shown that sensitivity coefficient calculations require $F^*(r)$ mesh values to be converged to between 10% and 20% relative uncertainty, a convergence criterion which is loose relative to typical neutron flux convergence standards. It should be noted that the distribution of the mesh cell uncertainties is right-skewed, and the average mesh cell uncertainty calculations is strongly influenced by mesh cells that "clip" a region of fissionable material, thus containing a small amount of fissionable material, receiving a small number of $F^*(r)$ tallies, and resulting in mesh cell uncertainties close to 100%. Although it was not calculated in this study, the median mesh cell uncertainty can be as small as one-half the average mesh cell uncertainty [25]. Regardless, the ability to use $F^*(r)$ mesh cells with 5%-10% uncertainty for sensitivity coefficient calculations is promising. Not only does it suggest that the Differential Operator and Iterated Fission Probability $F^*(r)$ calculation approaches can be used with the CLUTCH and Contributon methods to calculate sensitivity coefficients without an exorbitant increase in runtime, but that future $F^*(r)$ calculations may be able to circumvent calculating $F^*(r)$ during inactive generations by coupling SHIFT with a deterministic code. Similar to the CADIS methodology, this approach would use a deterministic calculation to obtain an estimate for $F^*(r)$ before

beginning a SHIFT calculation [26]. If $F^*(r)$ values with 10% uncertainty are sufficient for calculating sensitivity coefficients, then the approximations introduced by a deterministic simulation may still allow for a deterministic calculation of $F^*(r)$ that produces accurate sensitivity coefficients. This hybrid approach might not pan out because the large statistical uncertainties in the $F^*(r)$ values could have allowed for accurate sensitivity coefficient calculations if these uncertainties canceled out when particles streamed through many mesh cells; this cancellation would not have occurred for deterministically-determined $F^*(r)$ values because they would not have been randomly different from the true $F^*(r)$ values.

Chapter V

Conclusions and Future Work

This thesis includes a survey of existing methods for performing continuous-energy eigenvalue sensitivity coefficient calculations and introduced two new sensitivity coefficient calculation methods, the CLUTCH and Contributon-IFP Hybrid methods. The CLUTCH method has shown potential for use in continuous-energy sensitivity coefficient calculations, and has demonstrated the ability to accurately calculate sensitivity coefficients with high FoM for the multigroup test problems presented in this thesis.

In addition to the CLUTCH and Contributon-IFP Hybrid methods, this study has evaluated the performance of the Differential Operator, Iterated Fission Probability, and Contributon methods for performing sensitivity coefficients. The Differential Operator method can calculate sensitivity coefficients very efficiently and without using a prohibitive amount of memory, but had difficulty calculating accurate sensitivity coefficients for many of the test problems. Although the sensitivity coefficients that were produced by the Differential Operator method often showed a statistically significant difference when compared to reference sensitivities, the actual error in the Differential Operator sensitivity coefficients was often quite small, indicating that the Differential Operator method may be a viable method for preliminary sensitivity coefficient calculations. Methods exist for improving the accuracy of the Differential Operator method by accounting for the change induced in the fission source term by perturbations or by incorporating second-order differential terms, but these approaches were not

pursued in this study [19]. The fission source correction methods are essentially identical to the approach taken by the Iterated Fission Probability method for calculating sensitivity coefficients, and second-order differentials cannot be used for calculating the uncertainty in the eigenvalue for a system because cross-section covariance matrices typically contain only first-order cross-section uncertainties.

The Iterated Fission Probability method has been shown to produce accurate estimates for eigenvalue sensitivity coefficients, but can require a prohibitive amount of memory. The memory requirements for the IFP method scale directly with the number of latent generations used by the method, the number of particles simulated per generation, and the number of isotopes present in a system, and complex problems with hundreds of unique materials and high dominance ratios may require many gigabytes of memory for performing IFP calculations. It is possible to reduce the potentially large memory requirements of the IFP method by recording progenitor tallies only once for every number of latent generations instead of allowing particles from every generation to act as progenitors. This approach reduces the memory requirements of the IFP method by a factor equal to the number of latent generations used for a problem, but sacrifices calculation efficiency for these improvements in memory requirements. The Iterated Fission Probability method already suffers in terms of efficiency when compared to the Differential Operator and CLUCTH methods because the method requires progenitor fission chains to survive for a number of latent generations before recording sensitivity tallies, whereas the Differential Operator and CLUTCH methods produce non-zero sensitivity coefficient tallies for almost every collision a particle sees during its lifetime. The IFP method was shown to produce FoM that were about an order of magnitude lower than those from the CLUTCH method, but the difference in efficiency between the two methods should decrease when applied to continuous-energy calculations. The IFP method has been shown to increase the runtime of continuous-energy problems by about 2% when recording sensitivity coefficient tallies once for every number of latent generations; thus the IFP method can be expected to increase the runtime of a continuous-energy problem by about 40% for problems requiring 20 latent generations that record progenitor sensitivity tallies during every generation [5]. A 40% increase in problem runtime is quite significant, but is not prohibitive to performing continuous-energy

eigenvalue sensitivity coefficient calculations. A large portion of the runtime for multigroup IFP calculations is likely used for data processing, and this portion should become much less significant for continuous-energy problems because of the large amount of time used for continuous-energy cross-section lookups. Thus, because the runtimes for the IFP and CLUTCH methods will likely be similar for continuous-energy calculations, a more fair comparison between the efficiency of the IFP and CLUTCH methods might not examine the FoM for methods, but instead the ratio of the relative variances produced for calculations using the same number of active neutron histories. Table 5.1 shows the *variance gain*, or average ratio of the IFP and CLUTCH energy- and material-integrated sensitivity coefficient relative variances, that was produced by each of the test problems. It should be noted that the variance gain is equivalent to the ratio of the CLUTCH and IFP FoMs if the two calculations are assumed to have equal runtimes.

Table 5.1: Average IFP-CLUTCH variance gain

Model	**Number of IFP Latent Generations**	**Average Variance Gain**
Fuel Pin	2	6.57
Godiva	2	2.81
MCT	5	2.74
PST	5	8.77
LCT	2	2.72
PWR	10	31.75

Table 5.1 shows that even when runtime is ignored, the CLUTCH method produces a significant amount of speedup compared to the IFP method, and this gain is expected to increase for IFP calculations that use a larger number of latent generations for IFP calculations. Although the IFP-CLUTCH variance gain was largest for the PWR problem, the actual speedup seen for a continuous-energy PWR calculation is not expected to be this extreme because of the large number of inactive generations needed to tally $F^*(r)$.

Although some inaccuracy was observed for the Contributon-IFP Hybrid method, the Contributon and Contributon-IFP Hybrid methods were seen to generally produce

accurate but inefficient sensitivity coefficient estimates due to their approach of using secondary particles to calculate the importance of events. The low efficiency produced by these methods is expected to persist when the methods are extended to continuous-energy applications. The Contributon-IFP Hybrid approach was developed to use the Iterated Fission Probability methodology to calculate sensitivity coefficients while avoiding the method's potentially large memory requirements. The Contributon-IFP Hybrid method may be useful for calculating reference sensitivity coefficients for the largest and most complex problems because of its small memory requirements, and the Contributon method may be useful for large, massively-parallel sensitivity coefficient calculations. Other than the conventional TSUNAMI method, the Contributon method is the only method that requires almost no previous information on the lifetime of a particle to calculate importance of that particle. The CLUTCH, IFP, Differential Operator, and Contributon-IFP Hybrid approaches all store the reaction rates generated by a particle for an amount of time before calculating the importance associated with these reaction rates, and would need to pass these reaction rates between domains during domain-decomposed parallel simulation; thus, only the Contributon method can be used for massively-parallel, domain-decomposed sensitivity coefficient calculations.

Chapter 4 described several approaches for calculating the $F^*(r)$ importance weighting function used by the Contributon and CLUTCH methods. It was found that an $F^*(r)$ function is typically necessary for obtaining accurate sensitivity coefficients with these methods, and that an Iterated Fission Probability-based approach can successfully calculate $F^*(r)$ during the inactive generations of a Monte Carlo simulation. An approximately 1 cm^3 $F^*(r)$ mesh that simulated about 1,000 inactive neutron histories per mesh interval containing fissionable fuel was determined to be a sufficiently-refined and sufficiently-converged mesh for sensitivity coefficient calculations. The acceptable amount of uncertainty in the $F^*(r)$ mesh values was quite large, which suggests that the $F^*(r)$ mesh might be able to be calculated before a sensitivity coefficient calculation with a deterministic code. Future studies will investigate this hybrid approach, and will also investigate a mesh-free approach that uses Kernel Density Estimators to represent $F^*(r)$ as a continuous function.

The calculations examined in this study evaluated the accuracy of the sensitivity coefficient methods by calculating the sum of the χ^2 statistics across all energies and all materials in each problem, and it is possible that some methods produced poor estimates for select sensitivity coefficients but that these discrepancies were washed out when the χ^2 statistics were summed over all energies and materials. This possibility reflects the unfortunate lack of a complete approach for comparing the results from sensitivity coefficient calculations. The χ^2 approach used extensively throughout this study allows for a very rigorous comparison of the average disagreement between reference and calculated sensitivity coefficients, but it also allows poor agreement for some sensitivity coefficients to be masked by good agreement from other sensitivity coefficients. Furthermore, χ^2 comparisons do not look at the absolute difference between the sensitivity coefficients, and sensitivity coefficients that produce large χ^2 values may actually differ by a very small, or insignificant, amount. Comparing the percent difference between sensitivity coefficients works well for the largest and most significant sensitivity coefficients, but very small sensitivity coefficients can produce artificially large percent differences even when they are actually quite accurate. Graphical analysis of the sensitivity coefficients allows for a good heuristic assessment of the accuracy of a sensitivity coefficient method, but is not a statistically rigorous comparison. The only true way to compare the accuracy of a sensitivity coefficient calculation is to use the sensitivity coefficients from the calculation to calculate the total amount of uncertainty in the eigenvalue for the system, and to then determine whether this uncertainty is within some tolerance of the eigenvalue uncertainty generated by a reference calculation.

Future studies will include based on the work presented in this thesis will include:

- Calculating the $F^*(r)$ mesh using a deterministic transport code before performing Monte Carlo sensitivity coefficient calculations.
- Using Kernel Density Estimators to represent $F^*(r)$ as a function that is continuous in space.
- Conducting a thorough comparison of Nagaya's and Perfetti's approaches for calculating chi sensitivity coefficients.

- Extending the lessons learned and methods developed in this study to perform generalized sensitivity coefficient calculations using Monte Carlo methods.

Bibliography

[1] "SCALE: A Comprehensive Modeling and Simulation Suite for Nuclear Safety Analysis and Design," ORNL/TM-2005/39, Version 6.1, Oak Ridge National Laboratory, Oak Ridge, Tennessee (2011). Available from Radiation Safety Information Computational Center at Oak Ridge National Laboratory as CCC-785.

[2] United States Nuclear Regulatory Commission (2006). *Justification for Minimum Margin of Subcriticality for Safety* (FCSS-ISG-10). Retrieved from http://pbadupws.nrc.gov/docs/ML0616/ML061650370.pdf.

[3] J. E. Olhoeft, "The Doppler Effect for a Non–Uniform Temperature Distribution in Reactor Fuel Elements," WCAP–2048, Westinghouse Electric Corporation, Atomic Power Division, Pittsburgh (1962).

[4] X-5 Monte Carlo Team, "MCNP - A General N-Particle Transport Code, Version 5, Volume I: Overview and Theory," Tech. Rep. LA-UR-03-1987, Los Alamos National Laboratory, 2003.

[5] B. C. Kiedrowski, *Adjoint Weighting for Continuous-Energy Monte Carlo Radiation Transport*, doctoral dissertation, University of Wisconsin (2009).

[6] H. J. Shim, C. H. Kim, "Adjoint Sensitivity and Uncertainty Analyses in Monte Carlo Forward Calculations," *Journal of Nuclear Science and Technology*, **48**(12), pp.1453–1461 (2011).

[7] H. Hurwitz, Jr., "A note on the theory of danger coefficients," Tech. Rep. KAPL-98, Knolls Atomic Power Laboratory, 1948.

[8] M.L. Williams, "The Relations Between Various Contributon Variables Used in Spatial Channel Theory Applied to Reactor Shielding Analysis," *Nuclear Science and Engineering*, **63**, pp.220 (1977).

[9] Private Communication with Dr. Forrest B. Brown, Hollywood, Florida, June 2011.

[10] M. L. Williams, *Equations for Contributon Eigenvalue Solution*. Unpublished document (2007).

[11] Y. Nagaya, I. Kodeli, G. Chiba, M. Ishikawa, "Evaluation of sensitivity coefficients of effective multiplication factor with respect to prompt fission neutron spectrum," *Nuclear Instruments and Methods in Physics Research A*, **603**, pp.485–490 (2009).

[12] E. Lewis, W. Miller, Jr., *Computational Methods of Neutron Transport*, pp. 329, American Nuclear Society, La Grange Park, Illinois, USA (1993).

[13] G. F. Knoll, *Radiation Detection and Measurement*. John Wiley & Sons, Inc., 2010.

[14] S. Goluoglu, L. M. Petrie, Jr., M. E. Dunn, D. F. Hollenbach, and B. T. Rearden, "Monte Carlo Criticality Methods and Analysis Capabilities in SCALE," *Nuclear Technology*, **174**(2), pp.214–235 (2011).

[15] Private Communication with Dr. Michael Dunn, Oak Ridge, Tennessee, 2011.

[16] B. T. Rearden**,** M. L. Williams, M. A. Jessee, D. E. Mueller, and D. A. Wiarda, "Sensitivity and Uncertainty Analysis Capabilities and Data in SCALE," ***Nuclear Technology*** **174**(2), pp.236–288 (2011).

[17] B. T. Rearden, C. M. Perfetti, M. L. Williams, "SCALE Sensitivity Calculations using Contributon Theory," Proceedings of the *Joint International Conference on Supercomputing in Nuclear Applications and Monte Carlo 2010 (SNA + MC2010)*, Tokyo, Japan, October 17-21, 2010.

[18] G. Radulescu, D. E. Mueller, and J. C. Wagner, "Sensitivity and Uncertainty Analysis of Commercial Reactor Criticals for Burnup Credit," *Nuclear Technology* **167**(2), pp.268-287 (2009).

[19] K. F. Raskach, "An Improvement of the Monte Carlo Generalized Differential Operator Method by Taking into Account First- and Second-Order Perturbations of Fission Source," *Nuclear Science and Engineering*, **162**(2), pp.158–166 (2009).

[20] B. C. Kiedrowski, F. B. Brown, P. P. H. Wilson, "Adjoint-Weighted Tallies for *k*-Eigenvalue Calculations with Continuous-Energy Monte Carlo," *Nuclear Science and Engineering*, **168**(3), pp.226–241 (2011).

[21] F. B. Brown, "'K-effective of the World' and Other Concerns for Monte Carlo Eigenvalue Calculations," *Progress in NUCLEAR SCIENCE and TECHNOLOGY*, **2**, pp.738-742 (2011).

[22] M. Nakagawa, T. Mori, "Whole core calculations of power reactors by use of Monte Carlo method," *Journal of Nuclear Science and Technology*, **30** [7], pp. 692-701 (1993).

[23] *International Handbook of Evaluated Criticality Safety Benchmark Experiments*, Nuclear Energy Agency Nuclear Science Committee of the Organization for Economic Co-operation and Development, NEA/NSC/DOC(95)03 (2010).

[24] K. Banerjee, W. M. Martin, "Kernel Density Estimate Monte Carlo Global Flux Tallies," Proceedings of the *International Conference on Mathematics, Computational Methods & Reactor Physics (M&C 2009)*, Saratoga Springs, New York, May 3–7, 2009.

[25] C. M. Perfetti, W. R. Martin, B. T. Rearden, and M. L. Williams, "Determining Importance Weighting Functions for Contributon Theory Eigenvalue Sensitivity Coefficient Methodologies," *Proceedings of PHYSOR 2012*, Knoxville, Tennessee, April 15–20, 2012.

[26] J. C. Wagner, A. Haghighat, "Automated Variance Reduction of Monte Carlo Shielding Calculations Using the Discrete Ordinates Adjoint Function," N*uclear Science and Engineering*, **128**, pp. 186 (1998).